ACS NANO

www.acsnano.org

Two-Dimensional Carbon Graphdiyne: Advances in Fundamental and Application Research

Xuchen Zheng, Siao Chen, Jinze Li, Han Wu, Chao Zhang, Danyan Zhang, Xi Chen, Yang Gao, Feng He, Lan Hui, Huibiao Liu, Tonggang Jiu, Ning Wang, Guoxing Li, Jialiang Xu, Yurui Xue,* Changshui Huang,* Chunying Chen,* Yanbing Guo,* Tong-Bu Lu,* Dan Wang,* Lanqun Mao,* Jin Zhang,* Yue Zhang,* Lifeng Chi,* Wanlin Guo,* Xian-He Bu,* Hongjie Zhang,* Liming Dai,* Yuliang Zhao,* and Yuliang Li*

Cite This: *ACS Nano* 2023, 17, 14309−14346

Read Online

ACCESS | Metrics & More | Article Recommendations

ABSTRACT: Graphdiyne (GDY), a rising star of carbon allotropes, features a two-dimensional all-carbon network with the cohybridization of sp and sp^2 carbon atoms and represents a trend and research direction in the development of carbon materials. The sp/sp^2-hybridized structure of GDY endows it with numerous advantages and advancements in controlled growth, assembly, and performance tuning, and many studies have shown that GDY has been a key material for innovation and development in the fields of catalysis, energy, photoelectric conversion, mode conversion and transformation of electronic devices, detectors, life sciences, etc. In the past ten years, the fundamental scientific issues related to GDY have been understood, showing differences from traditional carbon materials in controlled growth, chemical and physical properties and mechanisms, and attracting extensive attention from many scientists. GDY has gradually developed into one of the frontiers of chemistry and materials science, and has entered the rapid development period, producing large numbers of fundamental and applied research achievements in the fundamental and applied research of carbon materials. For the exploration of frontier scientific concepts and phenomena in carbon science research, there is great potential to promote progress in the fields of energy, catalysis, intelligent information, optoelectronics, and life sciences. In this review, the growth, self-assembly method, aggregation structure, chemical modification, and doping of GDY are shown, and the theoretical calculation and simulation and fundamental properties of GDY are also fully introduced. In particular, the applications of GDY and its formed aggregates in catalysis, energy storage, photoelectronic, biomedicine, environmental science, life science, detectors, and material separation are introduced.

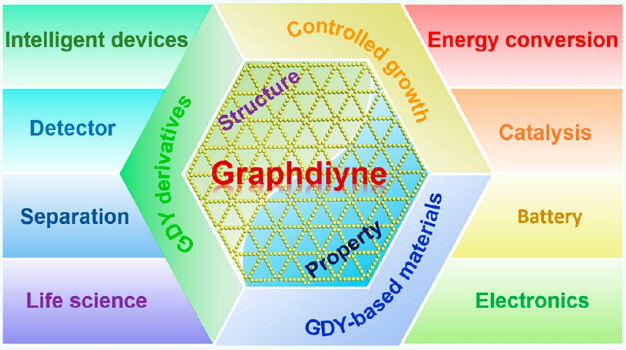

KEYWORDS: *graphdiyne, two-dimensional carbon materials, controlled growth, atomic catalysis, energy conversion, life science, intelligent device, material separation*

1. INTRODUCTION

Emerging carbon materials have become one of the frontier research fields in many disciplines due to their special physical and chemical properties and wide application prospects. However, traditional carbon materials (such as graphite, graphene, carbon nanotubes, fullerenes, etc.) that have been synthesized are only composed of sp^2 carbon atoms, and have been lacking sp and sp^2 cohybrid carbon allotropes, which is a serious lack of a comprehensive understanding of the connotation of carbon materials.[1] Therefore, it is very necessary and urgent to develop carbon materials with mixed hybrid states.

Scientists have long been concerned about the hybrid state of

Received: April 29, 2023
Accepted: July 10, 2023
Published: July 20, 2023

https://doi.org/10.1021/acsnano.3c03849

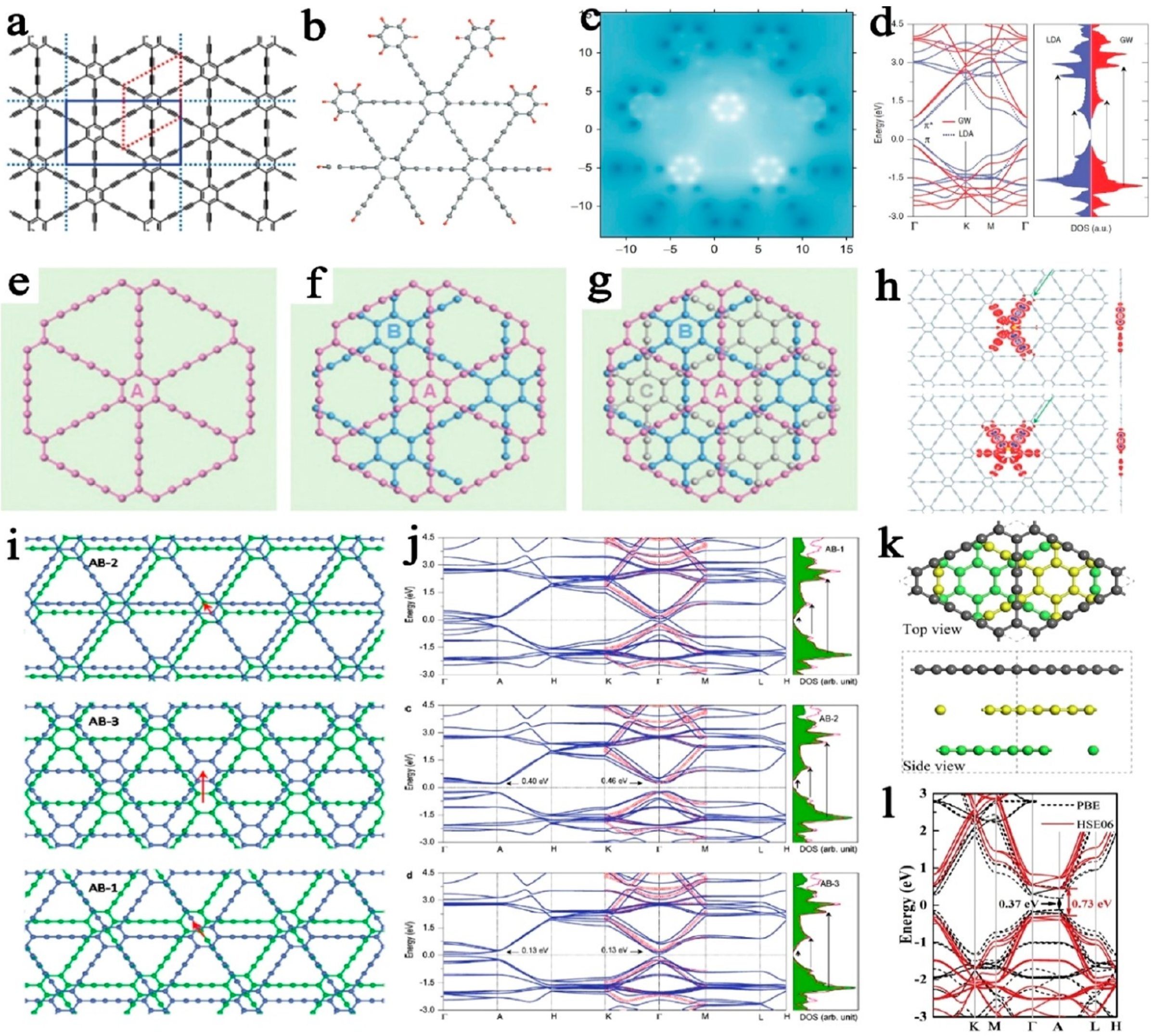

Figure 1. GDY structure. (a) Molecular structure of GDY. (b−c) ACS maps of GDY. Reproduced with permission from ref 8. Copyright 2015, Elsevier. (d) Top and side views of electron densities. (e−g) Various stacking structures of GDY. Reproduced with permission from ref 33. Copyright 2017, American Chemical Society. (h) Simulated band structures and density of states (DOS) of GDY. Reproduced with permission from ref 41. Copyright 2011, American Physical Society. (i) Geometrical structures of the AB-2, AB-3, and AB-1 stacked bulk GDY. (j) Corresponding band structure and the DOS simulation. Reproduced with permission from ref 39. Copyright 2013, American Chemical Society. (k) Top and side views of ABC stacking GDY. (l) Band structures using the PBE and HSE06 functionals. Reproduced with permission from ref 42. Copyright 2019, Elsevier.

carbon materials. It was not until 2010 that the sp and sp^2 cohybrid carbon allotrope GDY was synthesized by Li and coworkers.[1] GDY is a two-dimensional planar network formed by the connection of an alkyne bond (sp-C) and benzene ring (sp^2-C). It is considered as a carbon material with an almost perfect structure.[2−9] GDY's discovery has realized people's long-term expectation of the members of the carbon family, expanded the understanding of carbon material, and explored a direction of carbon materials research.[10−14] Importantly, scientists expect GDY-based materials to become key materials for catalysis,[15−17] energy storage,[18,19] energy conversion materials,[5,20−22] electronics, life sciences,[23] and multidomain next-generation high-performance devices.

The successful synthesis of GDY enriched the carbon material family and set a precedent for the preparation of all-carbon materials in solution by synthetic chemistry. The special arrangement of the sp/sp^2-hybridized carbon atoms in GDY gives it distinctive chemical and electronic structures as well as fascinating properties including an inherent band gap, excellent chemical and mechanical stability, highly conjugated and superlarge π structures, abundant carbon chemical bonds, infinite distribution of natural pores, intrinsic band gap, excellent chemical and mechanical stabilities, and so on.[10,24] In particular, the important property of the controllable growth of GDY on any substrate provides high convenience for the rapid preparation of films, heterojunctions, and composite material systems of different dimensions and sizes.[25,26] It changes the way of preparing and processing traditional carbon materials with high temperature and high pressure and shows the advantages and advanced characteristics of GDY in growth, assembly, controlled performance, and other aspects. These advanced materials and the characteristics of controllable growth and assembly of aggregation structures lead to the convenience of GDY-based materials in applications and processing. The results show that GDY has been widely used in the fields of energy, catalysis, environmental science, electronic devices, detectors,

https://doi.org/10.1021/acsnano.3c03849

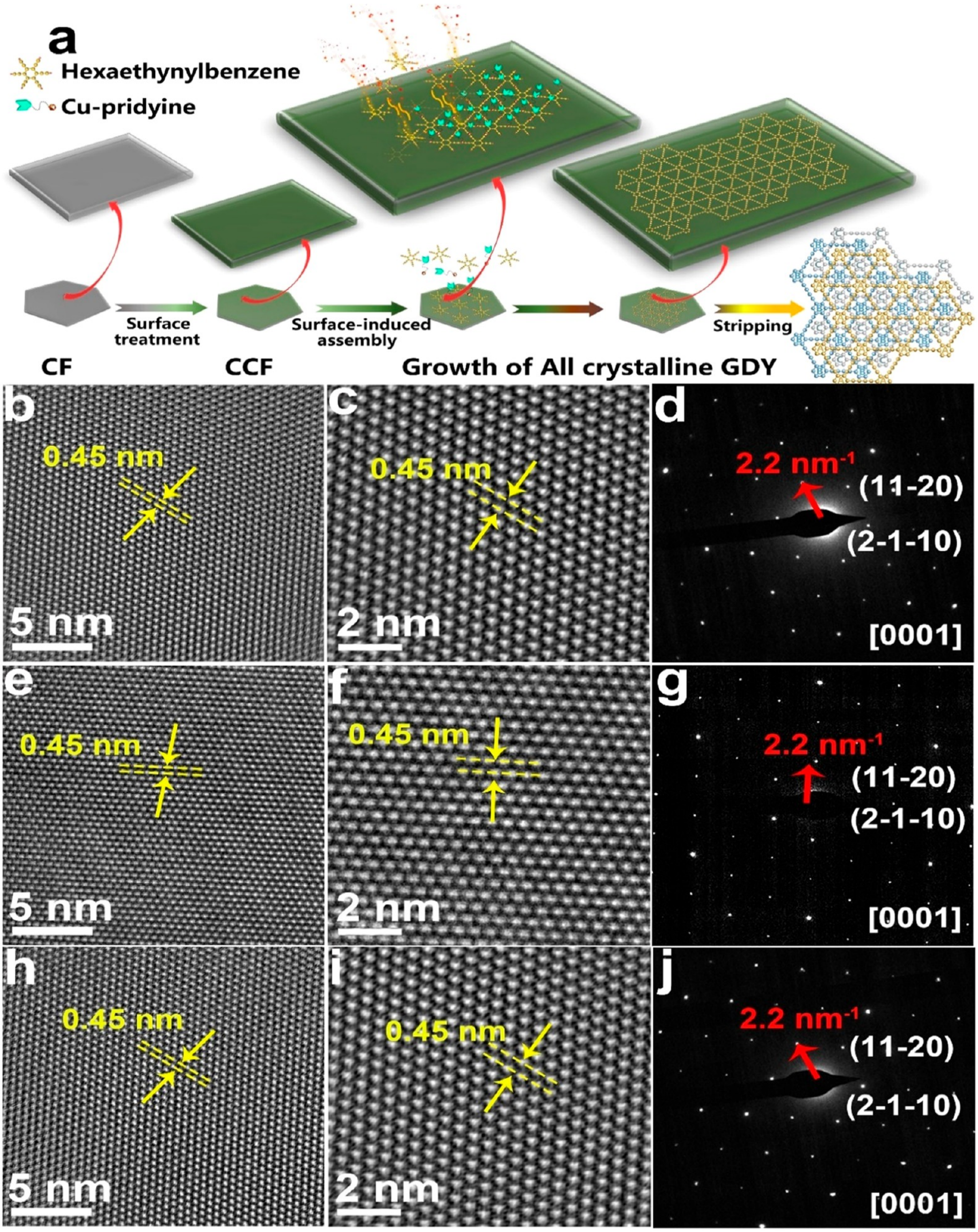

Figure 2. Crystalline GDY. (a) Schematic diagram of the synthesis of GDY. (b, c, e, f, h, i) HRTEM and (d, g, j) selected area electron diffraction (SAED) images. Reproduced with permission from ref 44. Copyright 2023, Elsevier.

biomedicine, and therapy.[27−35] We are also pleased to see that, as an emerging science, graphdiyne has given birth to some innovative scientific concepts, phenomena, properties, and applications. As one of the frontiers of chemistry and materials science, graphdiyne was listed in the Top 10 research areas in the 2020 Research Frontiers report, jointly released to the Top 10 world by the Institutes of Science and Development of the Chinese Academy of Sciences (CASISD), the National Science Library of Chinese Academy of Sciences, and Clarivate Analytics.

In this review, the growth, self-assembly method, aggregation structure, chemical modification, and doping of GDY are systemically discussed, and the theoretical calculation and simulation and fundamental properties of GDY are also fully

https://doi.org/10.1021/acsnano.3c03849
ACS Nano 2023, 17, 14309−14346

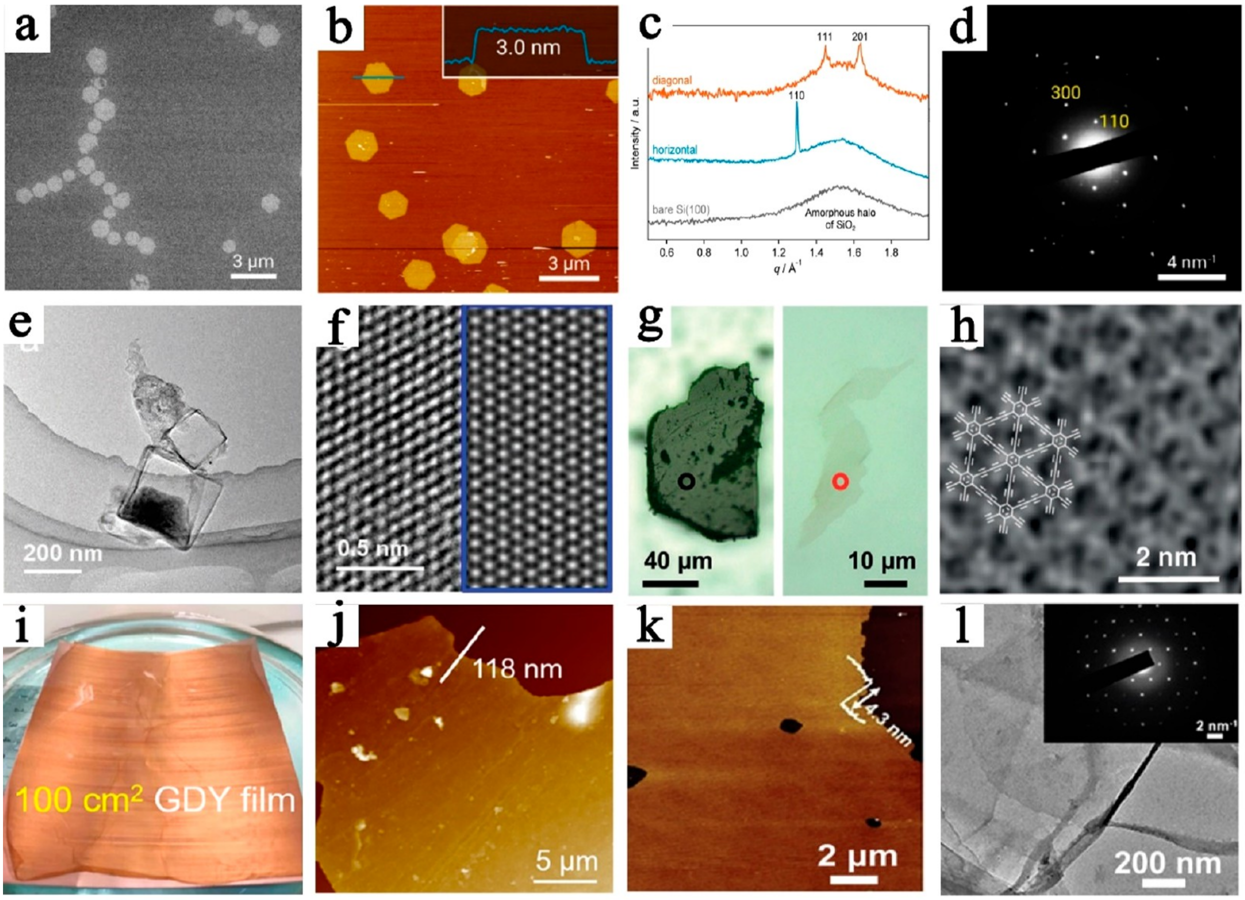

Figure 3. Few-layer and large area GDY. (a) TEM image of GDY films. (b) AFM image of the few-layer GDY films with the thickness of 3 nm. (c) 2D grazing incidence wide-angle X-ray scattering of GDY films. (d) SAED pattern of the GDY film. Reproduced with permission from ref 33. Copyright 2017, American Chemical Society. (h) TEM images of cuboidal GDY boxes and GDY sheets. (i) HRTEM image of GDY film. Reproduced with permission from ref 46. Copyright 2020, Wiley-VCH. (g) Optical images of the GDY powder and eGDY. (h) Theoretical simulation of the ion adsorption structures. Reproduced with permission from ref 47. Copyright 2019, Wiley-VCH. Optical photographs (i) and AFM image (j) of GDY nanosheets. Reproduced with permission from ref 48. Copyright 2022, American Chemical Society. (k) AFM images of few−layer GDY. (l) TEM and SADE images of the ABC-stacking GDY film. Reproduced with permission from ref 49. Copyright 2020, Wiley-VCH.

introduced. In particular, the applications of GDY and its formed aggregates in catalysis, energy storage, photoelectronics, biomedicine, environmental science, life science, detectors, and material separation are introduced. Finally, the opportunities and challenges for fundamental research and applied research of GDY are comprehensively discussed.

2. THE STRUCTURES AND PROPERTIES OF GRAPHDIYNE

GDY has a two-dimensional (2D) planar network comprised of sp^2-C (benzenic rings) and sp-C (alkyne, Figure 1a−c) and exhibits a hexagonal symmetry structure (*P6m*). Superior to traditional carbon materials, GDY possesses four types of chemical bonds of C_{sp^2}−C_{sp^2} (benzene ring, 1.41 Å), single C_{sp^2}−C_{sp} (1.40 Å), triple C_{sp}−C_{sp} (1.24 Å), and single C_{sp}−C_{sp} (1.33 Å) bonds. The sp- and sp^2-cohybrids make the surface charge highly unevenly distributed on GDY surfaces (Figure 1d). The theoretical cell crystal parameters *a*, *b*, *c*, and θ for the GDY structure are 9.38 Å, 9.38 Å, 3.63 Å, and 120°, respectively. The interlayer distance of GDY was calculated to be approximately 3.7 Å. Shuai and co-workers calculated the structure of GDY nanosheets by molecular dynamics simulations and obtained an optimized lattice parameter of 9.48 Å.[36] Monolayer GDY belongs to the hexagonal system and the *P6/mmm* space group. The *d*-spacings of the (100) and (110) planes are 0.821 and 0.474 nm, respectively. As shown in Figure 1e−g, few-layer graphdiyne theoretically has three different stacking modes with high symmetry. The AA-, AB-, and ABC-stacked GDY structural modes are ascribed to the symmetries of *P6/mmm*, $P6_3/mmc$ and $R\bar{3}m$ respectively. Nishihara and co-workers simulated the SAED of GDY and showed that, among all the stacking modes of the GDY structures with high symmetry, the (100) reflection of ABC-stacked GDY is absent, which corresponds to the systematic elimination of rhombohedral (R)-centering.[33]

Another important characteristic of GDY is that it has natural band gap (∼0.44−1.47 eV), which indicates that GDY is a direct band gap semiconductor material (Figure 1h−l).[37−41] Lu et al. compared the density of states and the energy band distribution of GDY and showed that the band gaps of GDY at the LDA and GW levels were calculated to be 0.44 and 1.10 eV, respectively.[41] The experimental and theoretical quasiparticle band gaps of GDY were 1.17 and 1.29 eV, respectively, which are very close to that of Si. Besides, GDY has a high in-plane electron mobility of 2×10^5 cm^2 V^{-1} s^{-1} and a hole mobility of 2×10^4 cm^2 V^{-1} s^{-1} at room temperatures, respectively, indicating its excellent electron transport properties.[36,39,42] Previous results also revealed that

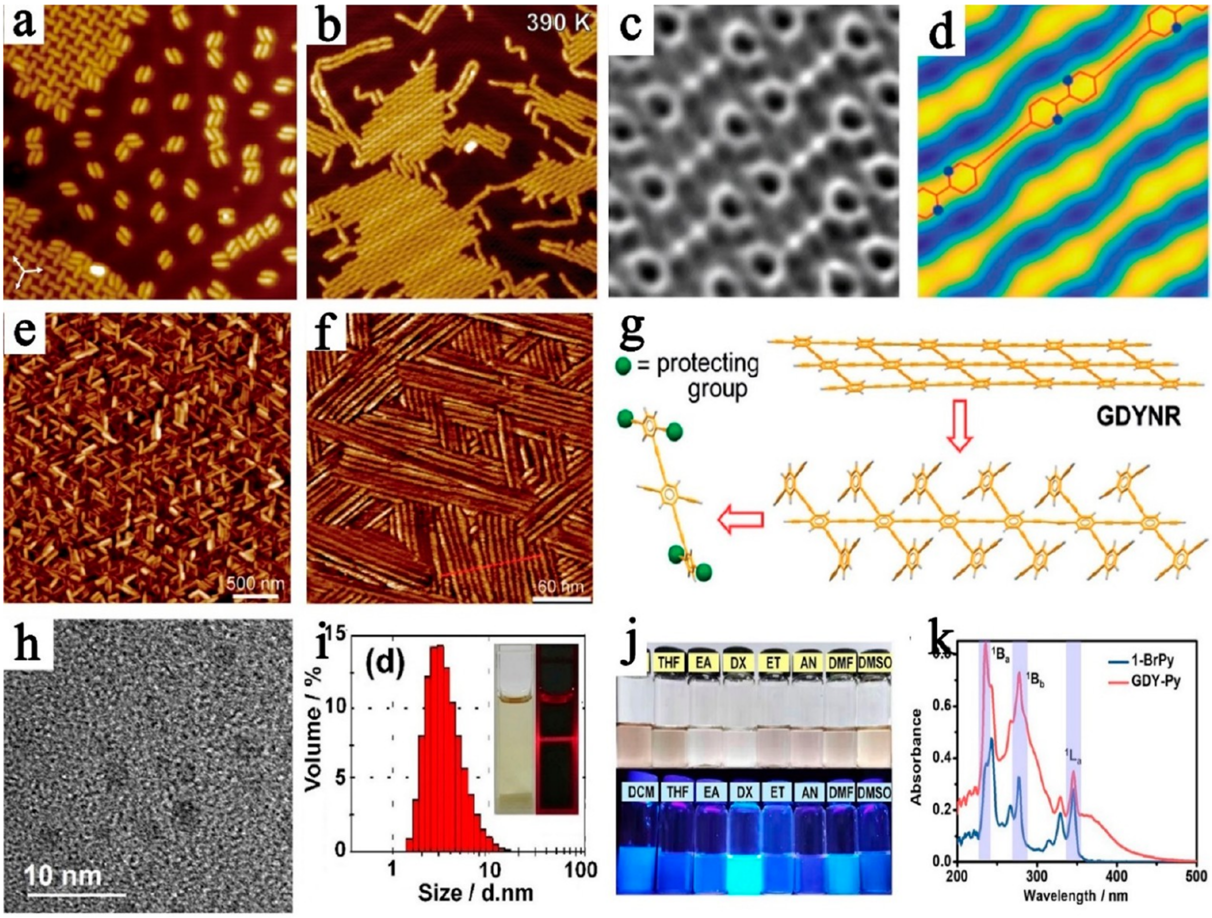

Figure 4. Low dimension of graphdiyne derivatives. (a) STM image of the self-assembly of pyridine-modified terminal alkynes on Au(111); (b) STM image of the self-assembly of N-doped GDYNY on the Au(111) surface; (c) bond-resolved AFM frequency shift image of N-doped GDYNY; (d) simulated STM image of N-doped GDYNY. Reproduced with permission from ref 73. Copyright 2023, American Chemical Society. (e−f) AFM height images of GDYNR. (g) Schematic structure of GDYNR.[74] Reproduced with permission from ref 74. Copyright 2020, Wiley-VCH. (h) TEM images of GDY-Py QDs. (i) Volume-weighted size distribution of GDY-Py QDs. (j) Photographs of GDY-Py QDs dispersions in different solvents. (k) UV−vis absorption of samples. Reproduced with permission from ref 75. Copyright 2020, Wiley-VCH.

the tuning of the GDY structures (e.g., quoted strain, boron/nitrogen doping, nanocarbon structures, and hydrogenation, etc.) could effectively tune the band gaps. For example, the optical energy gap of HGDY, MeGDY, and CNGDY were measured to be 1.73, 1.62, and 1.53 eV, respectively (CNGDY < MeGDY < HGDY), and the direct band gaps of HGDY, MeGDY, and CNGDY monolayers calculated by PBE functional were 0.79, 0.77, and 0.73 eV, respectively.[43]

3. SYNTHESIS OF GRAPHDIYNE AND ITS DERIVATIVES

3.1. Synthesis of Crystalline Graphdiyne. Crystalline structures have been desirable in engineering applications due to their obvious advantages compared to amorphous materials. More recently, our group established a stabilization method for green and selective synthesis of all-crystalline GDY through a simple surface-induced assembly coupling process (Figure 2a).[44] Typically, the carboxylated carbon fiber (CCF) was used as the substrate, and a piece of Cu foil was used to provide the Cu ions. The hexaethynylbenzene (HEB) was dropwise added into the above reactors, allowing for the adsorption and assembly of HEB on the surface of CCF, followed by the growth of all-crystalline GDY. This is the important work that realizes the controlled and facile growth of all crystalline GDY. The typical high-resolution TEM (HRTEM) images (Figure 2b,c,e,f,h,i) and corresponding selected-area electron diffraction (SAED) patterns (Figure 2d,g,j) demonstrated the successful synthesis of all-crystalline GDY. From the enlarged HRTEM images, a hexagonal lattice with a large *d* spacing of about 0.45 nm was observed, which can be indexed by the $(11\bar{2}0)$ reflections of GDY. The observed experimental patterns revealed that the all-crystalline GDY samples are stacked in the ABC stacking mode and not those of either AA or AB modes. This is in accordance with previous reports. Lu and co-workers observed the six-layered single crystalline of GDY with the ABC-stacked mode and a thickness of approximate 2.19 nm (corresponding to six layers).[45] In another work, Gao et al. reported a solution-phase van der Waals epitaxial growth method for the synthesis of crystal GDY on the surface of graphene.[34] Their results showed that the in-plane coupling was faster than out-of-plane growth toward the formation of an incommensurately stacked heterostructure composed of single-layer graphene and few-layer ABC-stacked GDY. Electron microscopy and Raman fingerprinting results demonstrated the perfectly ordered 2D GDY structures. Matsuoka et al. reported the liquid/liquid (liquid/gas) interface-assisted synthesis of crystalline GDY nanosheet (Figure 3a−d).[33] The obtained crystalline hexagonal GDY nanosheets showed an average

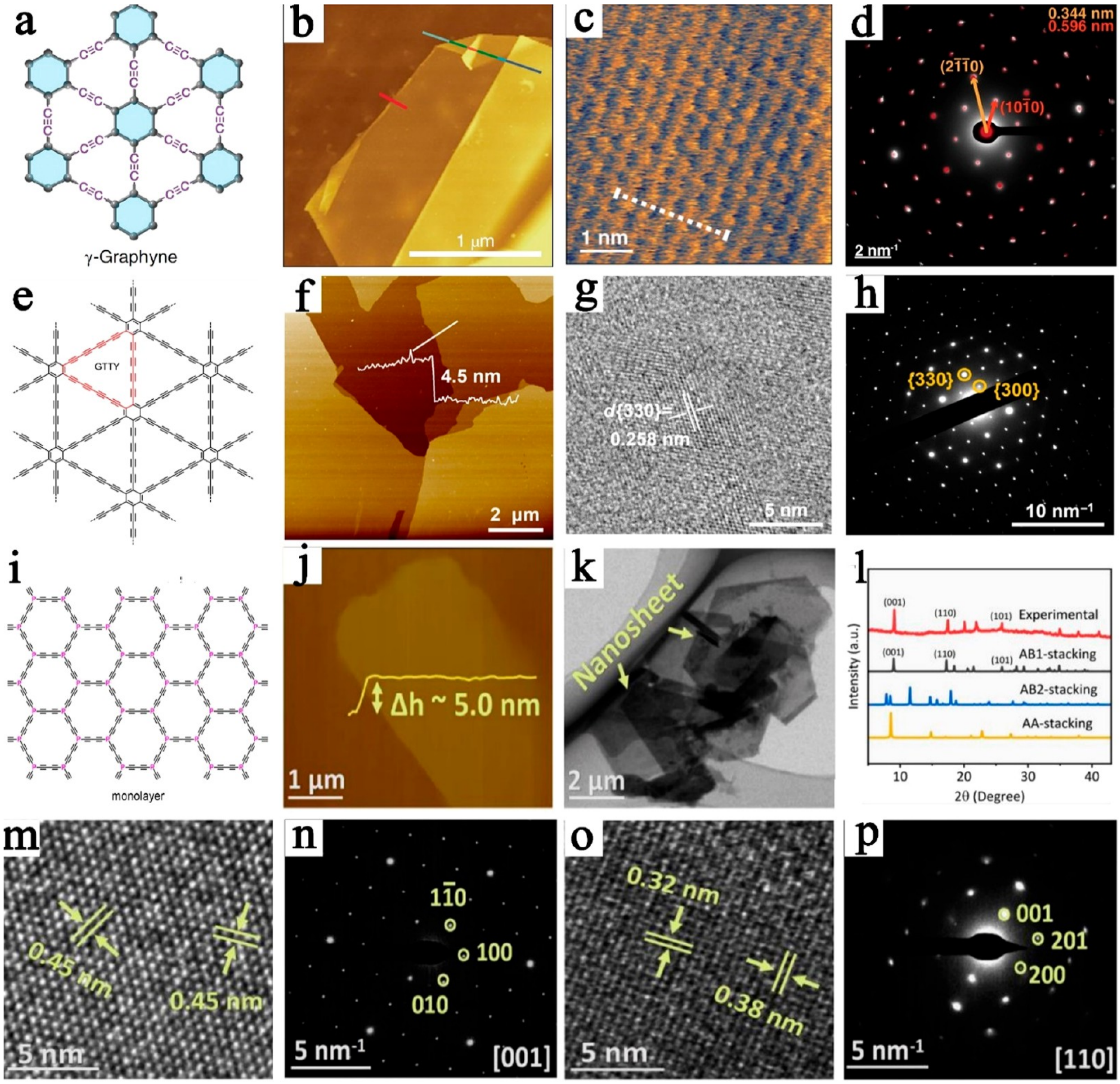

Figure 5. Other structures of graphdiyne derivatives. (a) Schematic diagram of the structure of graphyne. Reproduced with permission from ref 77. Copyright 2022, Springer Nature. AFM (b) and HR-AFM (c) images of graphyne. (d) SAED image of graphyne (inset: the one-dimensional strip structure of graphyne). Reproduced with permission from ref 78. Copyright 2022, American Chemical Society. (e) Scheme of the structure of GTTY. (f) AFM and (g) HR-TEM images of GTTY. (h) SAED image of GTTY. Reproduced with permission under a Creative Commons CC-BY License from ref 79. Copyright 2021, Chinese Chemical Society. (i) The structure of P-GDY. AFM (j), TEM (k), XRD (l), HRTEM (m, o), and SAED (n, p) images of P-GDY. Reproduced with permission from ref 80. Copyright 2023, American Chemical Society.

thickness of 3 nm (Figure 3a,b), average size of 1.5 mm, and an ABC stacking mode.

3.2. Synthesis of Few-Layer Graphdiyne. The reaction conditions of the reactions are essential for the synthesis of GDY with different layers or thickness.[46] Zhang and co-workers reported the catalyst-free synthesis of few-layer GDY at a solid/liquid interface by a microwave-induced temperature gradient (Figure 3e,f). Under microwave irradiation, inorganic crystals with large dielectric constants could be heated to certain temperatures, whereas the nonmicrowave-absorbing solvent remained at room temperatures, resulting in a temperature gradient, which leads to the facile synthesis of few-layer GDY. Experimental results showed that GDY nanosheets had a thickness of less than 2 nm and a field-effect mobility of 50.1 cm^2 V^{-1} s^{-1}. In addition to the chemical synthesis methods, Mao et al. reported a damage-free liquid-phase exfoliation method for the preparation of few-layered GDY (Figure 3g),[47] during which lithium hexafluorosilicate would be embedded into the bulk GDY followed by being exfoliated to the few-layer GDY. Optical and AFM images illustrated that GDY was exfoliated to several nanometers. HAADF-STEM images confirmed the crystalline structure of single-layer GDY (Figure 3h).[47] Hu et al. reported a simple and fast growth of large area GDY films on the surface of Cu foil by using a copper trichloro ($CuCl_3^-$) complex catalyst (Figure 3i–j).[48] The intensity of the conjugated diyne bonds for the as-synthesized GDY film in Raman spectra was significantly higher than that of previously reported ones. Based on the liquid–liquid interface synthesis, more few-layer graphdiyne synthesis methods have been developed (Figure 3k–l).[49] Zhou et al. also realized the synthesis of ultrathin GDY films using

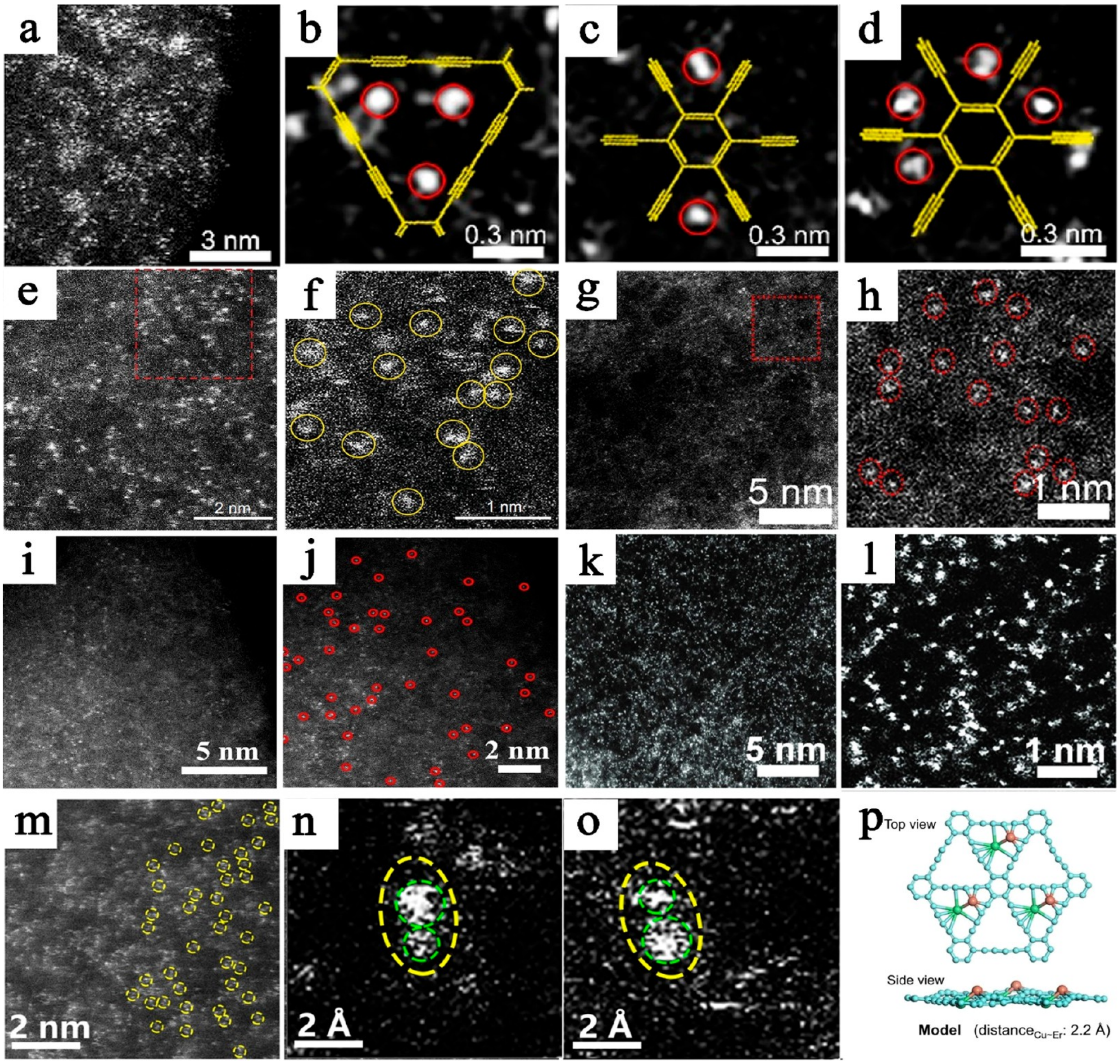

Figure 6. Graphdiyne-based atoms materials. HAADF-STEM images of (a–d) Mo^0/GDY/SACs, Reproduced with permission from ref 81. Copyright 2019, American Chemical Society. (e–f) Pd^0/GDY, Reproduced with permission under a Creative Commons CC-BY License from ref 82. Copyright 2021, Oxford University Press. (g–h) Co^0/GDY, Reproduced with permission under a Creative Commons CC-BY License from ref 83. Copyright 2021, American Chemical Society. (i–j) Cu^0/GDY Reproduced with permission from ref 84. Copyright 2022, Wiley-VCH. and (k–l) Pt^0/GDY. Reproduced with permission under a Creative Commons CC-BY License from ref 85. Copyright 2022, Wiley-VCH. (m–o) HAADF-STEM images of CuEr-GDY. (p) Top and side views of the optimized configurations of Cu and Er atoms anchoring on the GDY model. Reproduced with permission from ref 44. Copyright 2023, Elsevier.

graphene (or hexagonal boron nitride) as the surface template.[50] Kong et al. employed a more efficient Cu(II)-*N*,*N*,*N*′,*N*′-tetramethylethylenediamine (TMEDA) for faster growth of GDY at the superspreading liquid/liquid interface in water/toluene.[51] GDY samples with 4–50 nm thickness could be obtained in 2 h at room temperatures. By controlling the Cu^{2+} diffusion, Huang and co-workers achieved the control over the growth speed of GDY film.[52]

3.3. Synthesis of Graphdiyne Derivatives. One of the important properties of GDY is that it can do chemistry. This allows the controlled synthesis of a large amount of GDY derivatives with different chemical structures, including the heteroatoms (such as F, Cl, CN, B, and N) and functional group-substituted GDY.[53−67] Yuan and co-workers reported the synthesis of large-area porous hydrogen-substituted GDY (HsGDY) film under moderate reaction conditions via dehalogenative homocoupling.[68] S H-GDY, F-GDY, and Me-GDY were fabricated via monomer coupling at the interface by Song et al. via the liquid/liquid interface method.[69] Zhao and co-workers synthesized crystalline cyano-functionalized graphdiyne at a liquid/liquid interface, showing a 9-fold stacking mode.[70] Kan et al. explored the interfacial synthesis of 2D N-graphdiyne films.[71] Szczurek and co-workers developed a route toward the structure of N-graphyne via the Sonogashira cross-coupling reaction of 1,3,5-triethynylbenzene with cyanuric chloride.[72]

In addition to the 2D film morphology, Chi and co-workers reported the synthesis of well-aligned nitrogen-doped GDYNW on gold surfaces with selective on-surface acetylenic homocou-

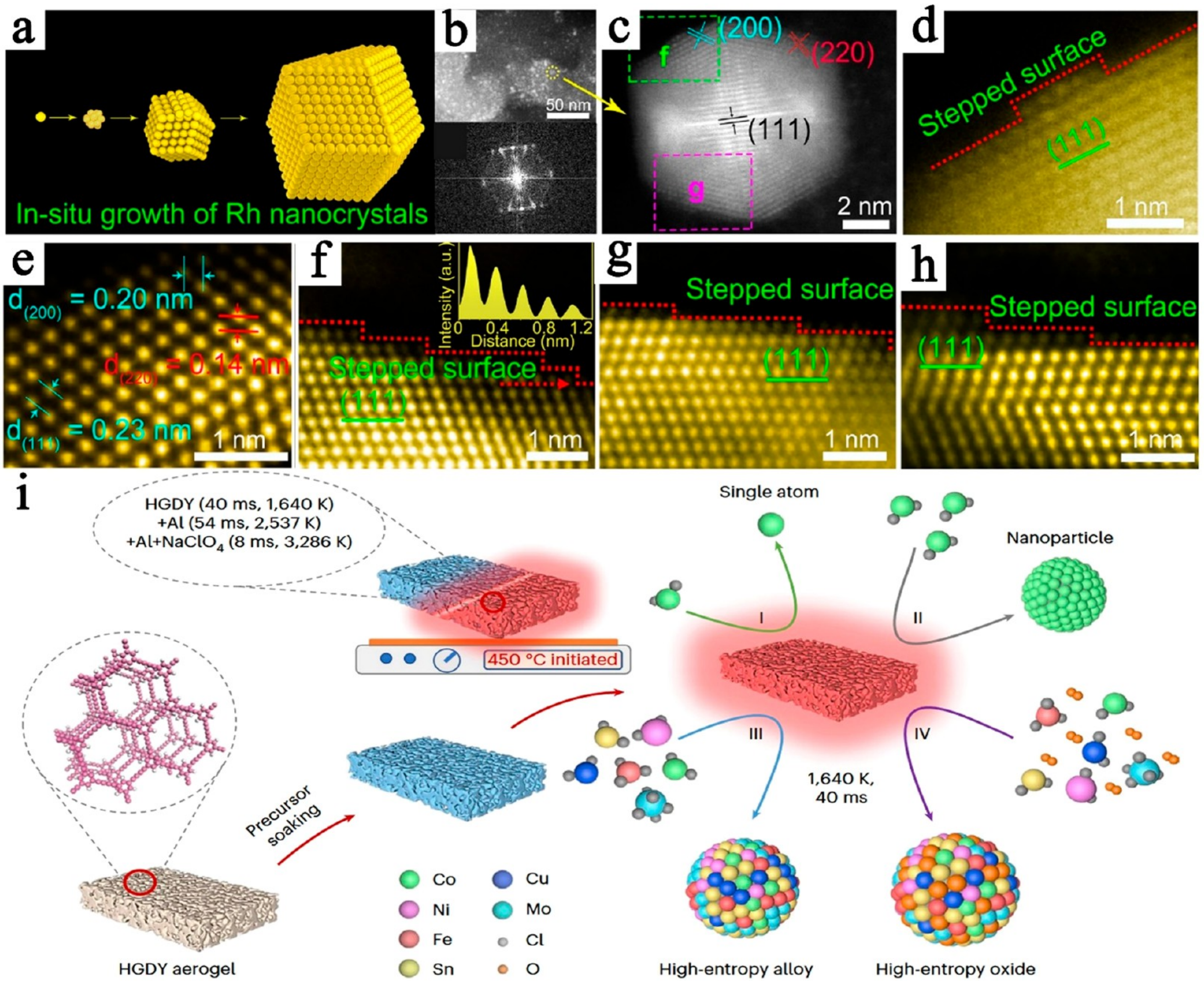

Figure 7. GDY-induced growth of nanostructures. (a) Simulated atomic arranging process and model of individual Rh nanocrystal. (b, c) HAADF-STEM image of Rh/GDY. (d−h) HAADF-STEM images of Rh/GDY. Reproduced with permission under a Creative Commons CC-BY License from ref 94. Copyright 2022, Springer Nature. (i) Schematic diagram of the hydrogen-substituted GAUSS process. Reproduced with permission from ref 96. Copyright 2023, Springer Nature.

pling reactions (Figure 4a−d).[73] Li and co-workers presented the synthesis of GDY nanoribbons with uniform width (4.16 nm in width; Figure 4e−g) through stepwise inter- and intramolecular Glaser−Hay coupling reaction of ethynyl groups.[74] Liu and co-workers proposed a facile strategy to the controllable synthesis of GDY quantum dots in which pyrene groups are covalently linked to GDY (GDY-Py QDs, 3 nm; Figure 4h−k).[75] Min et al. reported that the synthesis of GDY oxides QDs with superior photostability and hydrophilicity by solvothermal treatment of graphdiyne oxide nanosheets.[76] Recently, another important GDY derivative, graphyne, was synthesized by both the Zhang group (Figure 5a,b)[77] and Rodionov group (Figure 5c).[78] Rodionov et al. showed that the graphyne has a band gap of 0.48 eV, a hexagonal *a*-axis spacing of 6.88 Å, and an interlayer spacing of 3.48 Å (Figure 5d). Pan et al. reported the direct synthesis of crystalline graphtetrayne (GTTY) via the Glaser coupling (Figure 5e−h).[79] Wang et al. synthesized a crystalline 2D phosphine-graphdiyne (P-GDY) material (Figure 5i−l).[80] Experiment results revealed that the p−π conjugation of most trivalent was insignificant, owing to the pyramidal configuration. HRTEM and SEAD images in different crystal orientations indicated the high crystallinity of the P-GDY (Figure 5m−p). The lone pair electrons of the phosphorus atoms strongly participated in delocalization under the influence of the interlayer van der Waals forces in P-GDY.

3.4. Synthesis of Graphdiyne-Based Nanostructures. By utilizing the specific properties of the acetylene-rich structure, the spatial confinement effect, and the incomplete charge transfer between GDY and metal atoms, we achieved the successful anchoring of zerovalent metal atoms on the surface of GDY and named the developed catalysts “atom catalyst”. The emergence of atomic catalysts solves the challenge of traditional single atom catalysts that cannot anchor zerovalent metal atoms. In 2018, Li and co-workers originally reported the GDY-based zerovalent metal atom catalysts (Ni^0/GDY, Fe^0/GDY).[27] Single metal atoms were uniformly and separately anchored on the surface of GDY. Inspired by this pioneering work, a series of GDY-based zerovalent metal atom catalysts have been synthesized, such as Mo^0/GDY (Figure 6a−d),[81] Pd^0/GDY (Figure 6e,f),[82] Co^0/GDY (Figure 6g,h),[83] Cu^0/GDY (Figure 6i,j),[84] Pt^0/GDY (Figure 6k,l),[85] and so on (e.g., Rh, Ru, Mn, etc.).[86−88] More recently, Li and co-workers reported the bimetal atomic catalyst that featured atomically dispersed Cu and Er atoms anchored on all crystalline GDY (CuEr-GDY, Figure 6m−p). HAADF and DFT-optimized results confirmed

https://doi.org/10.1021/acsnano.3c03849

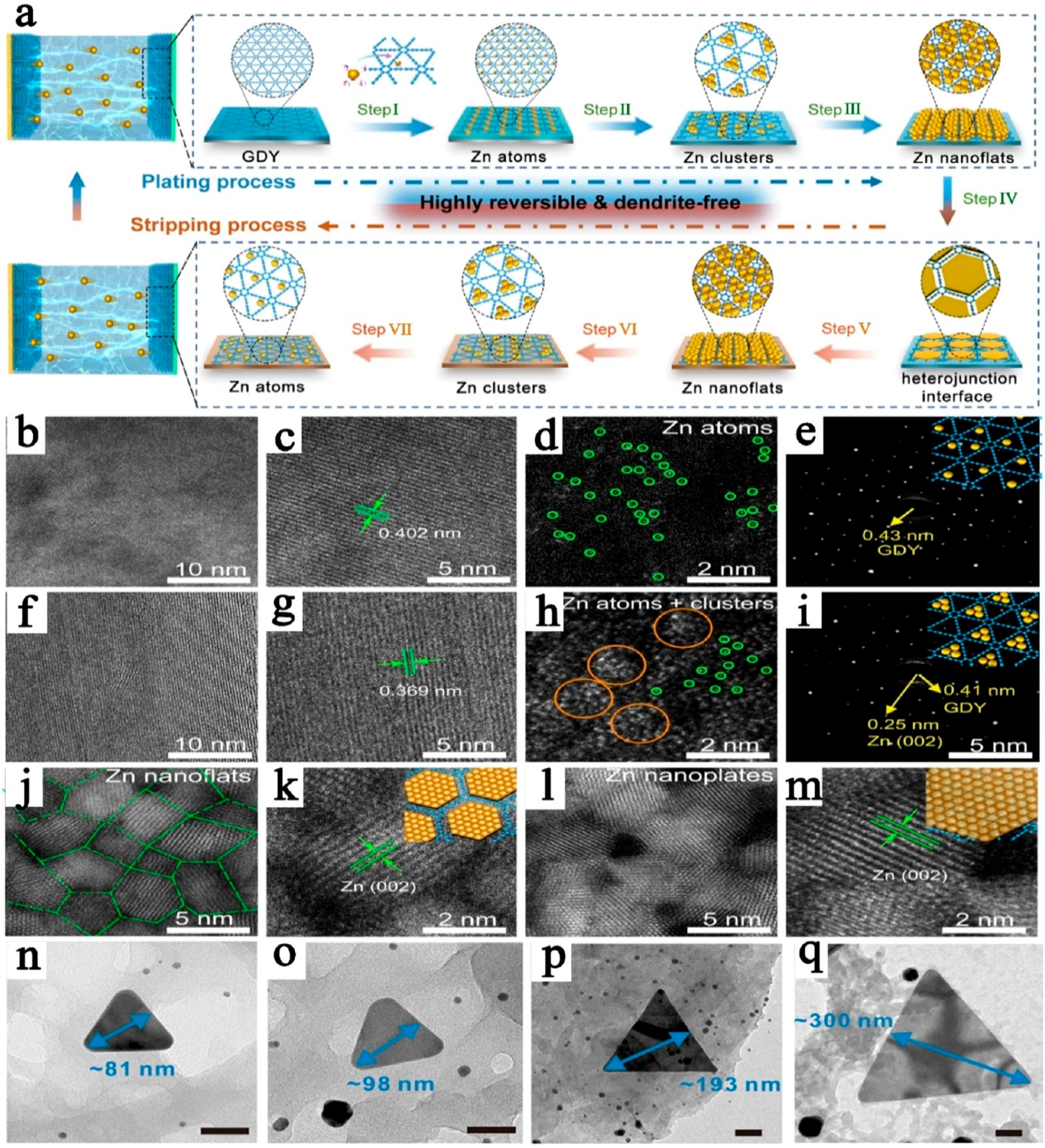

Figure 8. Graphdiyne-based heterojunction materials. (a, b) HRTEM and (c, d) HAADF-STEM images of the electrode after plating 1 s. (e, f) HRTEM and (g, h) HAADF-STEM images of the electrode after plating 2 s. HAADF-STEM images of the electrode after plating for (i, j) 5 s and (k, l) 360 s, respectively. Reproduced with permission from ref 97. Copyright 2023, Wiley-VCH. (n−q) Process of the growth of Au (111) nanoparticles on graphdiyne. Reproduced with permission under a Creative Commons CC-BY License from ref 98. Copyright 2020, American Chemical Society.

that the Cu and Er atoms are anchored on GDY with the structure of the model in Figure 6p.[89−93]

GDY could also realize the controllable synthesis of well-defined nanostructures with controlled crystalline phases, defects, and determined valence states of metal atoms. For example, Gao et al. reported a facile synthetic method to yield well-defined Rhodium nanocrystals in aqueous solution using formic acid as the reducing agent and graphdiyne as the stabilizing support.[94] HAADF-STEM images clearly show the presence of the atomic steps and the formation of high-density atomic defects, which could produce infinite active sites and therefore high intrinsic catalytic activity (Figure 7a−h). By using similar methods, Fang et al. reported the control of catalyst morphology, metal valence state, and coordination environment of iron oxides by using GDY as the growing support.[95] More recently, Cui and co-workers developed the method for ultrafast controllable preparation of metastable nanomaterials (Figure 7i).[96] They developed the hydrogen-substituted graphdiyne-assisted ultrafast sparking synthesis (GAUSS) which could achieve a temperature of 1,640 K within 40 ms. The hydrogen-

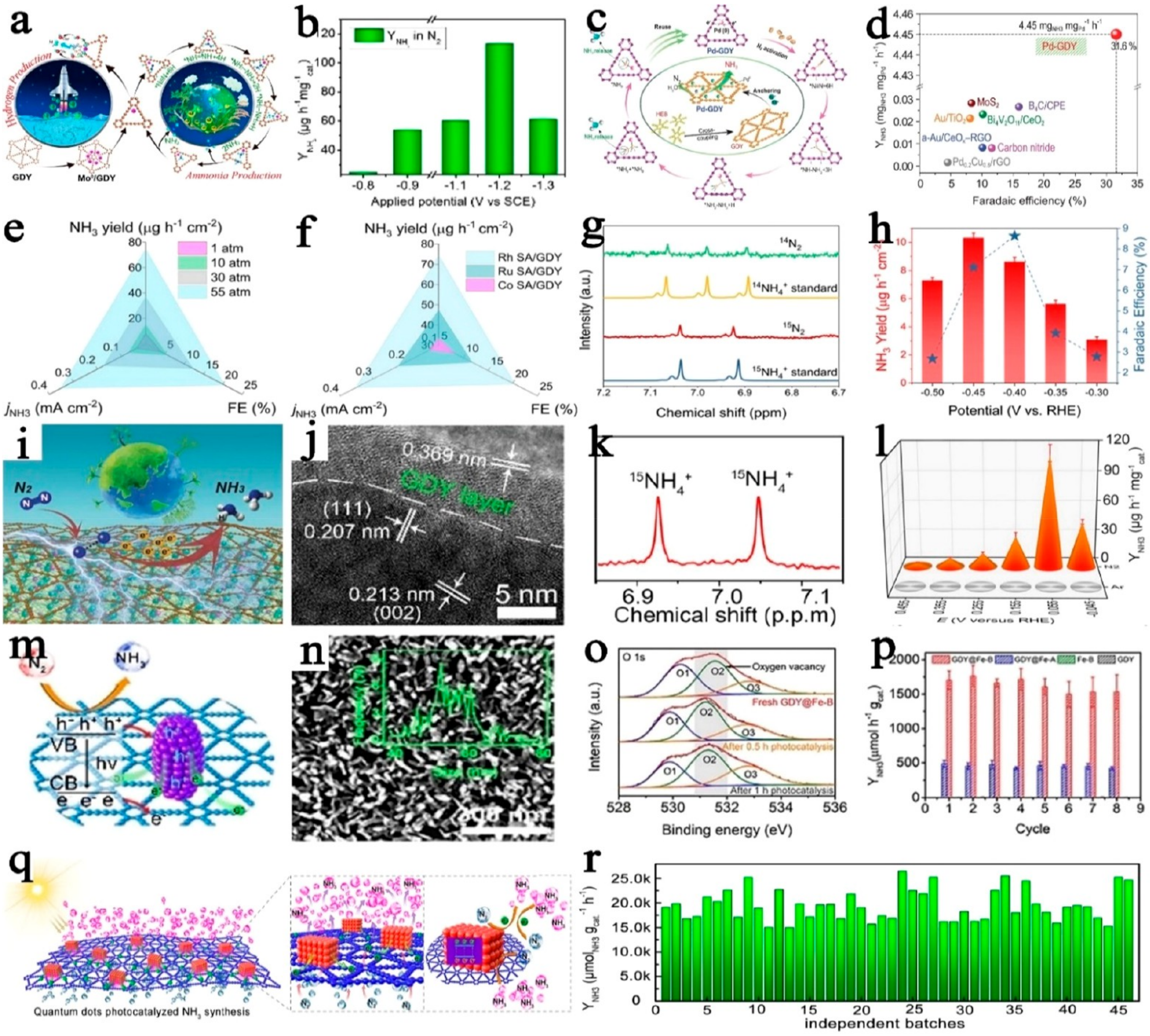

Figure 9. NH_3 synthesis. (a) Schematic representation of the synthesis and NRR processes of Mo^0/GDY. (b) Y_{NH_3} and FE at different potentials. Reproduced with permission from ref 81. Copyright 2019, American Chemical Society. (c) Schematic representation of NRR on Pd^0/GDY. (d) NRR performance comparison. Reproduced with permission under a Creative Commons CC-BY License from ref 82. Copyright 2021, Oxford University Press. (e) Comparison of the performance for Rh SA/GDY versus the exerted N_2 pressures. (f) Comparison of the performance for the prepared Rh, Ru, and Co SA/GDY. Reproduced with permission under a Creative Commons CC-BY License from ref 86. Copyright 2020, NAS. (g) ^1H NMR spectra of electrolytes. (h) The performance of Cl-GDY. Reproduced with permission from ref 104. Copyright 2019, American Chemical Society. (i) Schematic representation of NRR on GDY/Co_2N. (j) HRTEM images of GDY/Co_2N. (k) ^{15}N-isotope labeling experiments. (l) Y_{NH_3} of GDY/Co_2N at different potentials. Reproduced with permission from ref 105. Copyright 2020, Wiley-VCH. (m) Schematic representation of the photocatalyst NRR. (n) SEM image of GDY@Fe-B. (o) O 1s XPS spectra. (p) Y_{NH_3} at different times under irradiation. Reproduced with permission from ref 95. Copyright 2021, Wiley-VCH. (q) Schematic diagram of NH_3 production on GDY@CoO_x. (r) Y_{NH_3} of GDY@CoO_xQD in independent experiments. Reproduced with permission from ref 106. Copyright 2021, Elsevier.

substituted graphdiyne provided the acetylenic site of adsorption and high-density sites of microexplosions. A series of high-entropy alloys and high-entropy oxides could be synthesized by the universal method. These studies proved that GDY was an ideal substrate for the controlled synthesis of nanomaterials.

Recently, Luan et al. reported the process of materials changes while Zn ions were deposited or dissociated on graphdiyne (Figure 8a−m).[97] And Fan, Li, and co-workers demonstrated the process of Au(111) in situ growth on graphdiyne (Figure 8n−q).[98] Benefitting from in situ growth on an arbitrary substrate at room temperature and atmospheric pressure, graphdiyne could simultaneously achieve the stabilization of materials and modulation of active sites at the interface. Wang et al. reported a universal growth method to achieve stabilization of electrode materials by in situ coating with graphdiyne.[99] And Zhang et al. reported the in situ growth of GDY on the surface of cobalt−nickel mixed oxides that effectively optimized the adsorption/desorption capacities of the intermediate and promoted direct C−N coupling for urea synthesis.[100] Besides, the sandwich structure was typically synthesized in two steps. First, the other materials were prepared on GDY, followed by in situ cladding few-layer GDY film via a coupling reaction. These various controllable synthesis and design approaches have led to a wide range of applications for GDY-based materials in the fields of catalysis, energy, biology, and intelligent devices.

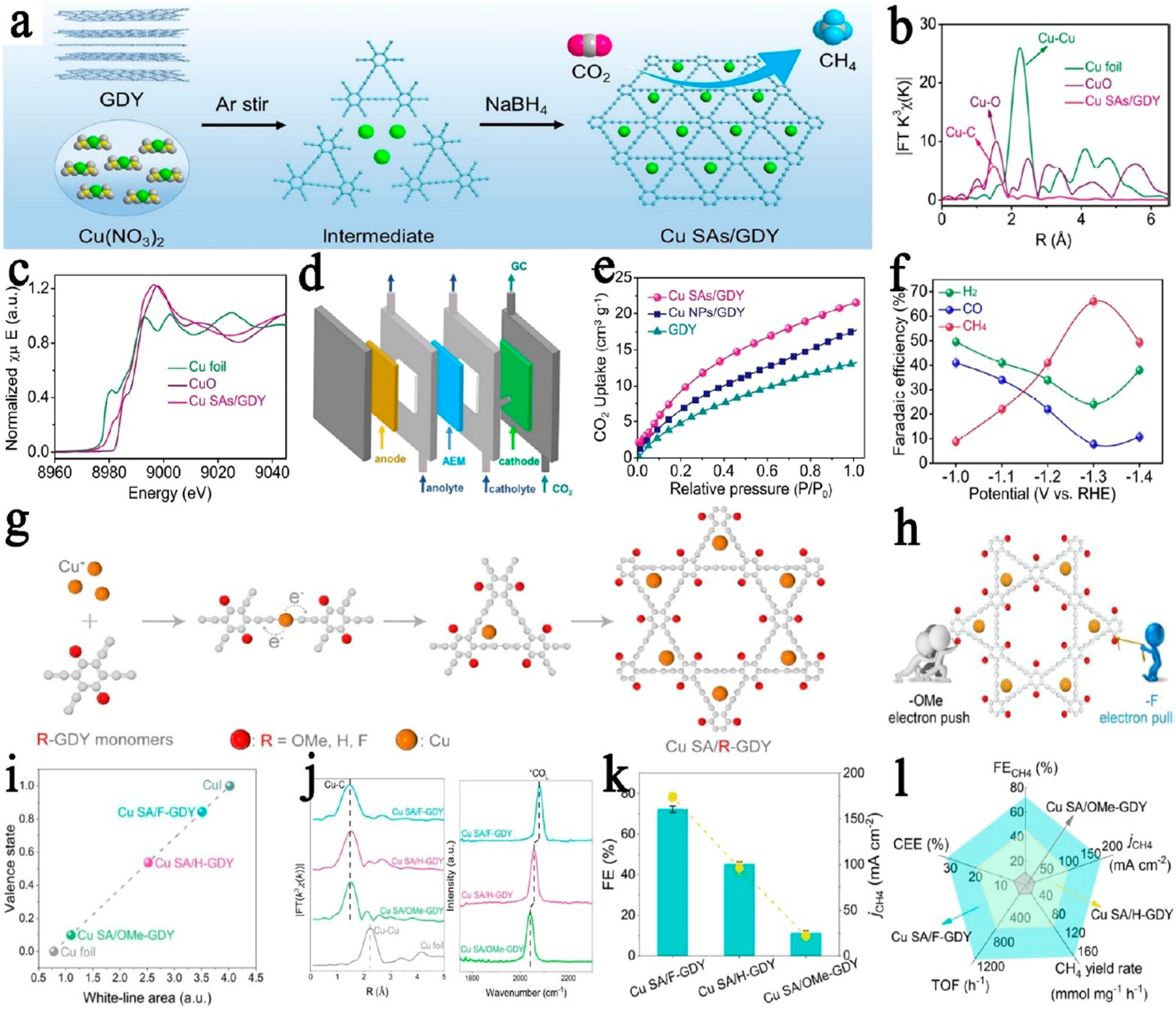

Figure 10. Electrocatalytic carbon dioxide reduction to methane. (a) Schematic illustration of the synthesis of Cu SAs/GDY. (b) HAADF-STEM images of the Cu SAs/GDY. XANES (c) and EXAFS (d) spectra of Cu SAs/GDY. (e) Diagram of flow cell device. (f) Faradaic efficiency of Cu SAs/GDY at different potentials. Reproduced with permission from ref 84. Copyright 2022, Wiley-VCH. (g) Schematic diagram of the synthesis of Cu SAs/RGDY. (h) HAADF-STEM image and EDX mapping of the Cu SAs/F-GDY. (i) The average valence state of samples. (j) EXAFS spectra of Cu SAs/RGDY and Cu foil. (k) CO-probed DRIFT spectra. (l) The Faradaic efficiency and current density of CH$_4$ of Cu SAs/RGDY at −1.2 V. Reproduced with permission from ref 112. Copyright 2023, Wiley-VCH.

4. GRAPHDIYNE-BASED CATALYTIC MATERIALS

The unevenly distributed surface charge, large specific surface area, and excellent stability of GDY endow it with infinite active sites, high intrinsic activity, and stability for catalysis.[96] GDY-based catalysts have made significant progress in various fields, including the nitrogen reduction reaction (NRR) for ammonia production, the nitrate reduction reaction (NtRR), hydrogen evolution reaction (HER), oxygen evolution reaction (OER), CO$_2$ reduction reaction (CO$_2$RR), and many other different reactions.[27,29,101,102]

4.1. Ammonia Synthesis. The development of synthetic ammonia chemistry is a great opportunity to promote the progress of human society. Efficient conversion of inert atmospheric nitrogen (N$_2$) molecules into ammonia (NH$_3$) at room temperature and ambient pressure to conventional Haber-Bosch processes is still a big challenge. Compared with traditional catalysts, GDY-based catalysts have shown outstanding advantages in the process of nitrogen fixation to ammonia through both NRR and NtRR. Li and co-workers reported the GDY-based zerovalent Mo atom catalysts (Mo^0/GDY, mass loading: 7.5 wt %) for efficient NRR at room temperature and ambient pressure (Figure 9a).[81] HAADF-STEM images and XAFS spectroscopy confirmed the successful anchoring of zerovalent Mo atoms on GDY and the high dispersion of the active sites. Besides, experimental and theoretical analyses reveal the presence of incomplete charge transfer between GDY and Mo atoms. These advantages endow the atom catalyst with excellent catalytic activities, showing a high NH$_3$ yield rate (Y$_{NH_3}$) of 145.4 μg h^{-1} mg^{-1} and NH$_3$ purity of 100% (Figure 9b). Our group further synthesized a GDY-based zerovalent Pd atomic catalyst through a self-reduction strategy (Figure 9c).[82] DFT results revealed that the obtained Pd^0/GDY had a downhill energetic trend for NRR. Experimental results demonstrated that the HER of Pd^0/GDY was effectively suppressed and resulted in excellent NRR performances, with the highest Y$_{NH_3}$ of 4.45 ± 0.30 mg$_{NH_3}$ mg$_{Pd}$$^{-1}$ h^{-1} compared to reported catalysts (Figure 9d). ^{15}N-isotope labeling experiments confirmed 100% purity of produced NH$_3$. Later, Duan and co-workers reported a GDY-based zerovalent Rh and Ru atom catalyst for NRR in a pressurized reaction system (Figure 9e−f), showing a NH$_3$ yielding rate of 74.15 μg h^{-1}·cm^{-2} and an FE of 20.36% at 55 atm.[86] Fang et al. reported a GDY-based Mn atom catalyst with highly dispersed Mn atoms on GDY. The catalyst achieved a high Y$_{NH_3}$ of 46.78 μg h^{-1} mg^{-1} and faradaic efficiency (FE) of 39.83%.[88] Zou et al. compared the NRR catalyst performance of several low-valence single metal atoms on GDY.[103] In addition to GDY-based atom catalysts, Duan et al. showed that Cl-GDY could promote the absorption and reduction of nitrogen and result in an effective NRR (Figure 9g−h).[104] A GDY-based

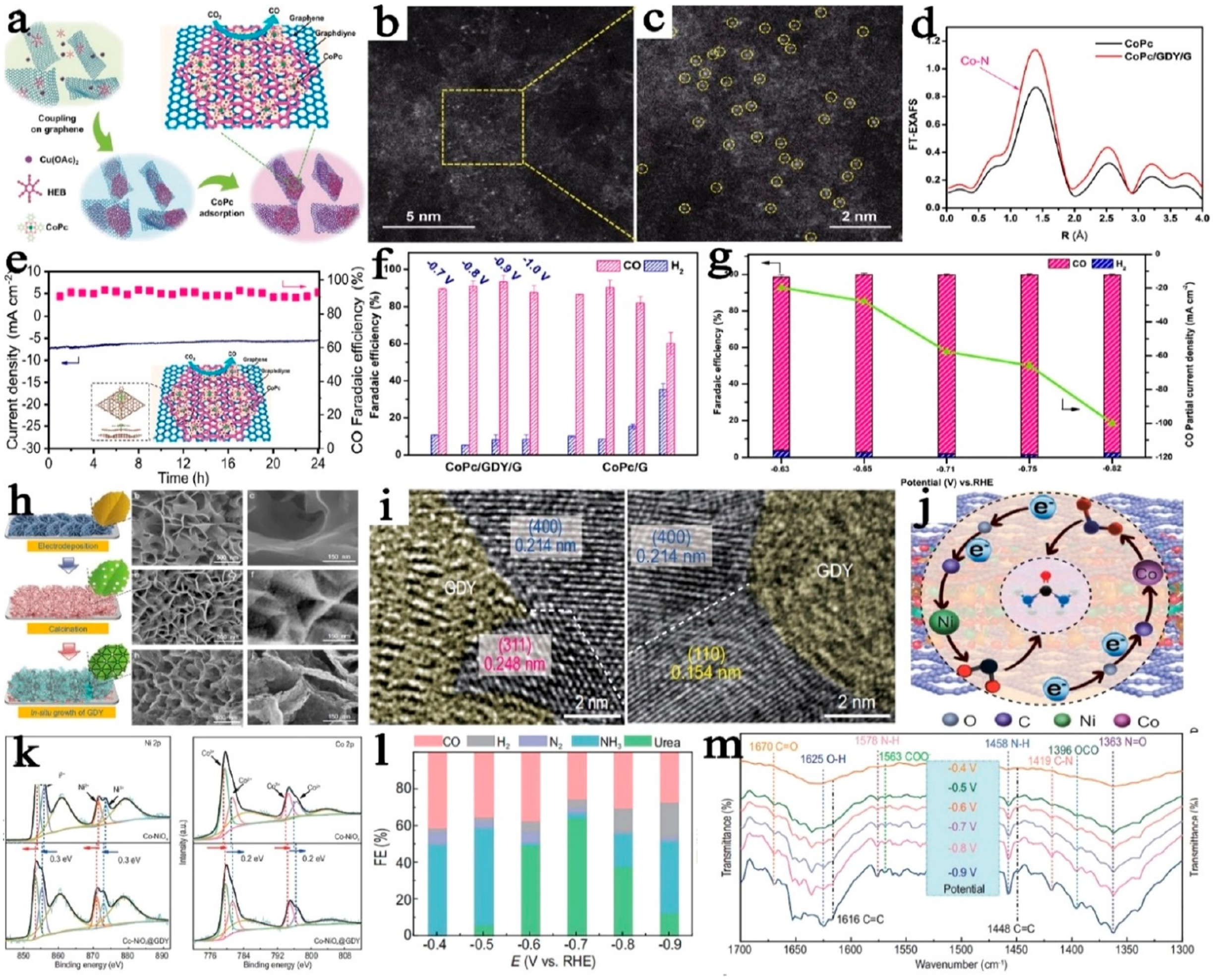

Figure 11. Electrocatalysis of CO_2 fixation. (a) Schematic diagram of the synthesis of CoPc/GDY/G. (b−c) HAADF-STEM images of CoPc/GDY/G. (d) Co K-edge XANES spectrum of samples. (e) Faradaic efficiency and CO partial current density of CoPc/GDY/G in CO_2RR. (f) Faradaic efficiency of samples. (g) The stability test of CoPc/GDY/G. (h) Schematic representation and SEM images of the synthesis of Co-NiO_x@GDY. Reproduced with permission from ref 114. Copyright 2021, American Chemical Society. (i) TEM images of Co-NiO_x@GDY. (j) Schematic diagram of the charge transfer. (k) XPS spectra of Co-NiO_x@GDY. (l) Faradaic efficiency obtained at different potentials of Co-NiO_x@GDY. (m) FTIR spectra of Co-NiO_x@GDY at different potentials. Reproduced with permission under a Creative Commons CC-BY License from ref 100. Copyright 2023, Oxford University Press.

heterostructure catalyst (GDY/Co_2N; Figure 9i−j) was synthesized by Li and co-workers to realize highly efficient ammonia production, giving the highest Y_{NH_3} and faradaic efficiency of 219.72 μg h^{-1} mg^{-1} and 58.60% in 0.1 M HCl electrolytes (Figure 9k−l).[105] As a 2D carbon allotrope with an intrinsic band gap, graphdiyne has the advantages of high carrier mobility, uneven surface charge distribution, and porous structure for photocatalytic nitrogen fixation. Fang and co-workers synthesized a GDY@Janus magnetite catalyst for an efficient photocatalytic nitrogen reduction (Figure 9m−n).[95] Their results showed that GDY could effectively tune the morphology of the catalysts and the valence state/coordination environment of Fe atoms, which provided more active sites and modified the band gap of the catalytic material (Figure 9o). The controllable growth of different morphologies of Janus magnetite (Fe-A and Fe-B) on graphdiyne exhibited a transformative photocatalytic performance with the highest ammonia yield reaching 1916.06 μmol h^{-1} g^{-1} (Figure 9p). More recently, the GDY-supported CoO_x quantum dots reported by Li and co-workers achieved an ultrahigh ammonia yield rate of 19583 μmol h^{-1} g^{-1}, which could be attributed to the GDY-enhanced surface plasmon resonance property, better than all reported catalysts (Figure 9q−r).[106]

Although the research of nitrogen fixation to ammonia via NRR has made big progress during the past decades, the ammonia synthesis with high yield rates to meet industrial requirements is still largely limited by the large kinetic barrier to break the stable N≡N triple bond. An alternative approach for ammonia production is to use nitrate as the nitrogen source. The electroreduction of nitrate to ammonia could effectively address environmental pollution and energy problems. Zhao et al. reported a zeolitic imidazolate framework nanocubes (ZIFNC)@GDY catalyst with a donor−bridge−acceptor interface for highly efficient ammonia production by the in situ growth of a 2D graphdiyne film on ZIFNCs.[107] sp-C−Co was changed by the interfacial structure, significantly enhancing the nitrate reduction performance, with the Y_{NH_3} of 0.40 ± 0.02 mmol h^{-1} cm^{-2} and a high FE of 98.51 ± 0.75%. Another Fe_3C@GDY electrocatalyst with a donor−acceptor structure was reported to have high selectivity and activity for NH_3 production in dilute nitrate electrolytes.[108] Zheng et al. presented Cu^0/GDYNA with the highest Y_{NH_3} of 15.45 mmol h^{-1} cm^{-2} and the maximal ammonia faradaic efficiency of 81.25% at ambient temperatures.[109] Ma et al. synthesized the hybrid nanoarrays of Cu-MOFs@HSGDY, which could decrease the nitrate concentration from 200 to 18.4 ppm with the reduction reaction.[110] Ni/Co-MOFs@HSGDY achieved an FE over 90% on both a wide pH and potential range.[111]

4.2. Carbon Dioxide Conversion. The accumulation of greenhouse gas CO_2 in the atmosphere is the primary driver of the current climate change. Converting CO_2 into fine chemical products is an important method to overcome the greenhouse effect and achieve

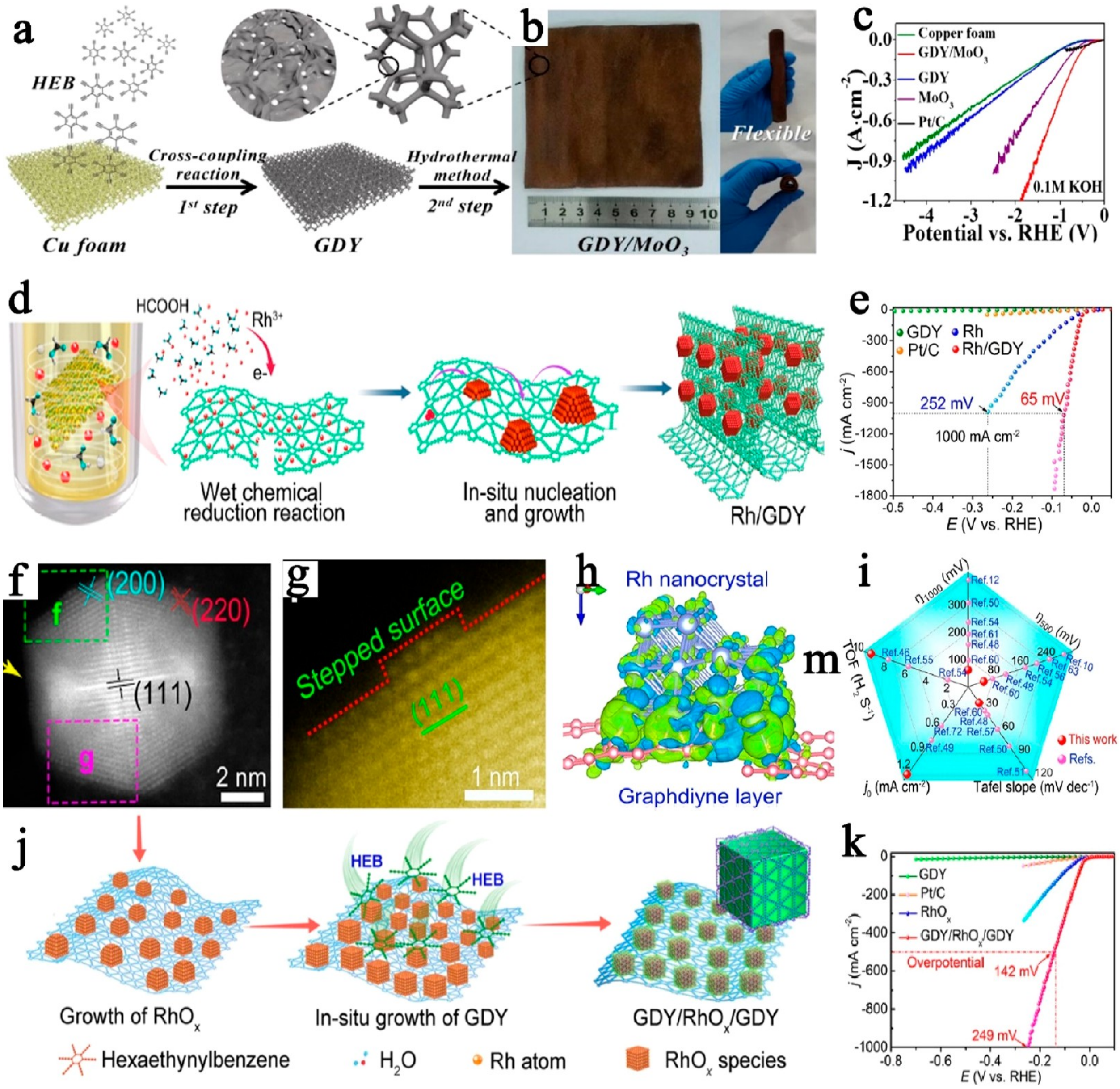

Figure 12. High current density hydrogen evolution. (a) Schematic illustration of the synthesis of GDY/MoO_3 catalyst. (b) The optical image of GDY/MoO_3. (c) Linear voltammetry curves of samples at high-current density. Reproduced with permission from ref 121. Copyright 2021, American Chemical Society. (d) Synthesis schematic diagram of porous Rh/GDY electrodes. (e) HER polarization curves at high current density. (f–g) HAADF-STEM image of Rh/GDY. (h) Differential charge distribution diagram of Rh/GDY. (i) Seawater splitting performance comparison. Reproduced with permission under a Creative Commons CC-BY License from ref 94. Copyright 2022, Springer Nature. (j) Synthesis diagram of GDY/RuO_2/GDY. (k) HER polarization curves of samples. Reproduced with permission under a Creative Commons CC-BY License from ref 123. Copyright 2022, NAS.

carbon neutrality. However, the CO_2RR is limited by its complex reaction pathways and slow reaction kinetics, resulting in low reactivity and selectivity. Therefore, designing a type of catalyst with high selectivity, activity, and stability is urgently required. Wang and co-workers reported the synthesis of Cu SAs/GDY by in situ anchoring of Cu atoms on graphdiyne for carbon oxide reduction to methane (Figure 10a).[84] HAADF-STEM images and XAFS spectra demonstrated that the coordination Cu−C bond in Cu SAs/GDY was successfully constructed via an assisted reduction process using sodium borohydride (Figure 10b−c). Theoretical calculations and in situ Raman electrochemistry results indicated that the *OCHO intermediate in the reaction path was beneficial for CH_4 generation. The Cu SAs/GDY exhibited high methane selectivity (FE = 81%) at a high partial CH_4 current density of 243 mA cm^{-2} (Figure 10d−f). Duan, Zhang, and co-workers further researched the carbon oxide reduction reaction performance of GDY derivatives with anchored single Cu atoms (Figure 10g−h).[112] The XAFS results demonstrated that the functional groups in the GDY derivatives successfully tuned the electronic structure and chemical valence of a single Cu atom (Figure 10i−j). Diffuse reflectance infrared Fourier transform spectra illustrated a peak shift of the adsorbed CO molecules on Cu SAs/RGDY. Theoretical calculations showed that the significant difference in the selectivity of the CO_2RR of Cu/RGDY could be attributed to the positive Cu centers adjusted by the electron-withdrawing group. The methane faradaic efficiency of Cu SAs/FGDY was 72.3% (Figure 10k−l). Wang and co-workers reported a sp-N doped GDY metal-free catalyst for the high-performance electroreduction of CO_2 to CH_4.[113] Zhang and co-workers synthesized CoPc/GDY/G via electrocatalytic van der Waals interactions for high-selectivity CO_2 reduction to CO (Figure 11a).[114] HAADF-STEM images illustrated that cobalt phthalocyanine was

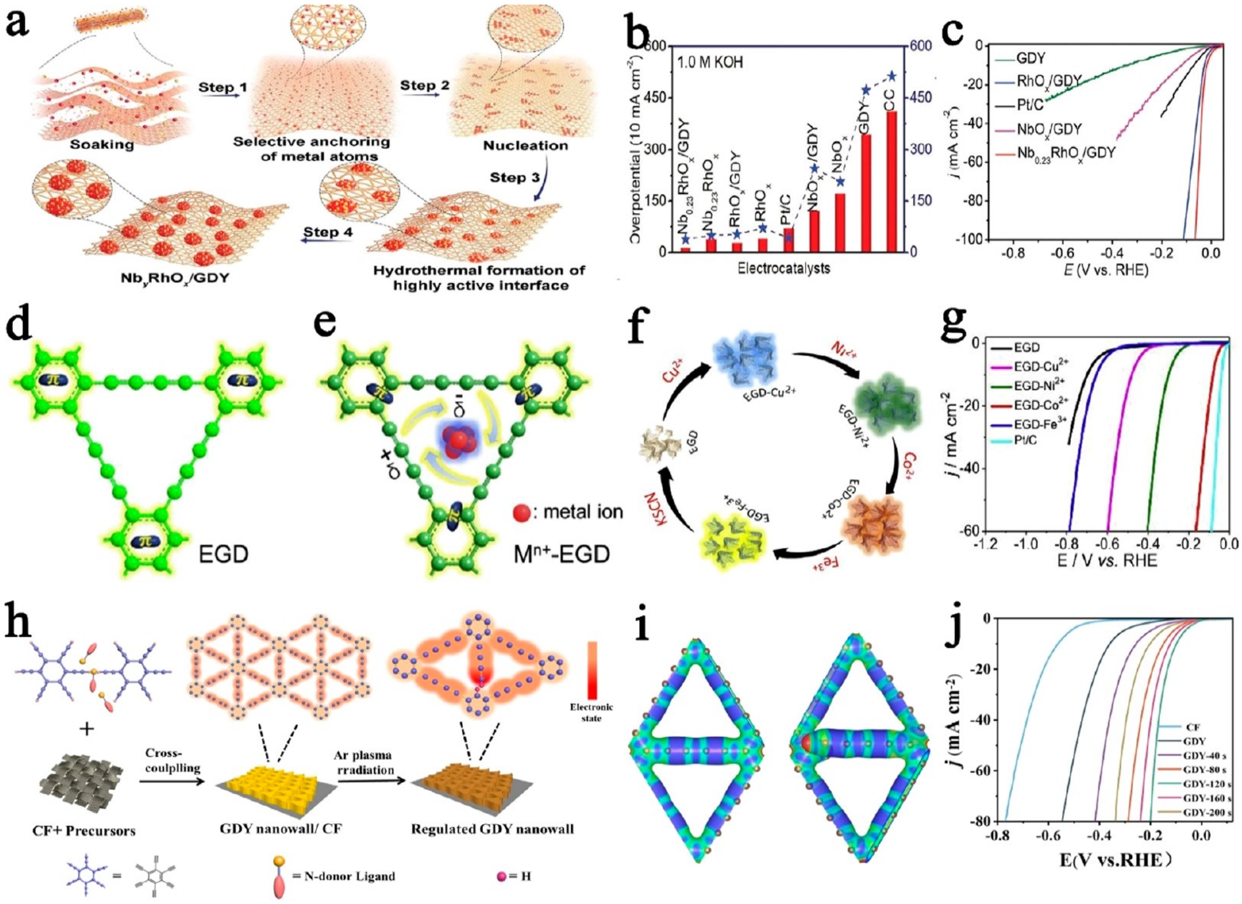

Figure 13. Other elements and structure of the GDY-based catalyst applied in HER. (a) Schematic representation of the synthesis of Nb_yRhO_x/GDY. (b) Overpotentials of samples with current density achieved at 10 mA cm^{-2}. (c) HER polarization curves of samples. Reproduced with permission under a Creative Commons CC-BY License from ref 124. Copyright 2022, Wiley-VCH. Electron distribution of (d) graphdiyne and (e) metal ions/graphdiyne. (f) Schematic illustration of the metal ions on the GDY according to the different capacity of coordination. (g) HER polarization curves of samples. Reproduced with permission from ref 125. Copyright 2019, Elsevier. (h) Schematic illustration of the synthesis of I-GDY. (i) Electrostatic potential (ESP) of pristine GDY and I-GDY. (j) HER polarization curves of samples. Reproduced with permission from ref 126. Copyright 2022, Wiley.

anchored on a 2D graphdiyne/graphene conductive scaffold and monodispersed (Figure 11b−c). The results of Raman and XAFS spectra demonstrated that the coordination environment of Co was a Co−N bond, illustrating the integrity of the phthalocyanine structure in the catalyst (Figure 11d). The strong charge transfer between GDY and CoPc, abundant reactive centers, and high electron conductivity synergistically contributed to this excellent electrocatalytic performance (Figure 11e−g). Zhao et al. showed that the efficient charge transfer between graphdiyne and C_3N_4 promoted photogenerated charge separation and transport, resulting in excellent CO_2RR performance.[115] Similar carbon nitride sheets/graphdiyne heterogeneous research was also reported by Wang et al.[116] GDY based heterostructure catalysts have also exhibited high photocatalytic CO_2RR performances. For instance, 2D GDY/Bi_2WO_6 nanosheets could promote light absorption and charge separation, leading to multielectron products (CH_4 and CH_3OH).[117] CdS/GDY with strong interfacial-interaction-induced sulfur vacancies exhibited high activity and selectivity for the photocatalytic CO_2 reduction to CO without a sacrificial agent.[118] Xu et al. further demonstrated that directed electron transfer between GDY and TiO_2 nanofibers enhanced CO_2 photoreduction efficiency.[119] Lu et al. synthesized ultrathin Co-doped GDY encapsulated $CsPbBr_3$ nanocrystals to achieve high CO_2RR performance with the high CO yield rate of 27.7 μmol g^{-1} h^{-1}.[120]

CO_2 enables the storage of renewable electricity from intermittent sources in a dense and versatile form, providing renewable carbon feedstock for the chemical industry. In addition, the catalytic CO_2 synthesis of other important chemical products, such as urea, is a potential route to fix carbon dioxide. Zhang et al. reported that Co-NiO_x@GDY efficiently reduced carbon dioxide and nitrite to synthesize urea.[100] The recorded faradaic efficiency and yield rates of urea were as high as 64.3% and 913.2 μg h^{-1} mg^{-1}, respectively (Figure 11h). Co-NiO_x@GDY was synthesized by in situ growth of graphdiyne on Co−Ni bimetallic oxide (Figure 11i−j). XPS spectra revealed a strong incomplete charge-transfer phenomenon at the multiheterointerfaces (Figure 11k). FTIR spectroscopy measurements showed that the interface structures stabilized the absorption of the intermediates and promoted direct C−N coupling (Figure 11l−m). Another potentially successful route involves the efficient cycloaddition of CO_2 to cyclic carbonates. Li and co-workers developed an organic strategy for fixing CO_2 in styrene oxide by Co^0/GDY ACs.[83] The yield rate of production reached 532 mmol mg^{-1} h^{-1} at 80 °C and normal pressure with nearly 100% conversion and current density of production (>2e$^-$) of Cu SAs/RGDY at −1.2 V.[112]

4.3. Hydrogen Energy Conversion.

Water splitting with H_2 and O_2 evolution is a promising approach to solve the current energy and environmental crises. GDY-based catalysts exhibited excellent performance in previous studies. Guo and co-workers reported excellent hydrogen evolution reaction (HER) activity and stability with a high current density in a 0.1 M KOH electrolyte.[121] The catalyst GDY/MoO_3 was synthesized by a hydrothermal method on a Cu foam (Figure 12a−b). The strong chemical interaction and electron transfer characterized by XPS and XANES measurements demonstrated that sp-hybridized carbon atoms were involved in the C−O−Mo bonds. The catalyst performance at a high current density was further investigated in an alkaline environment. As a result, GDY/MoO_3 achieved a 1 A cm^{-2} current density at an overpotential of 1.7 V (Figure 12c). According to theoretical calculations, this excellent performance was attributed to the increase in the type and number of active sites induced by the C−O−Mo bands.

Recently, Li and co-workers designed a Rh/GDY catalyst with a high electrocatalytic performance in heavy saline water electrolysis.[94] The Rh nanocrystals nucleated in situ and grew on the surface of GDY during Rh^{3+} reduction by HCOOH (Figure 12d−e). The low coordination number of the Rh structure of Rh/GDY was revealed by high-resolution HAADF-STEM images (Figure 12f−g). The XPS results showed that the Rh nanocrystals were stabilized by the formation of stable sp-C−Rh bonds. With the smallest overpotential of 65 mV, the current density could reach 1 A cm^{-2} in simulated seawater (Figure 12e,i). Similar to Rh/GDY, a noble metal electrocatalyst GDY-Pd was synthesized by Li and co-workers for efficient HER. With in-situ growth of a Pd(111) single crystal on the surface of GDY, the electrocatalyst could reach 1 A cm^{-2} at the overpotential of only 261 mV.[122] Two-layer heterostructure catalyst GDY/RuO_2/GDY was synthesized by Gao et al. for efficiency seawater electrolysis (Figure 12j).[123] The sp-C−O−Rh interface in the sandwich structure provided more active sites. The overall seawater splitting performance could achieve 500 mA cm^{-2} at only 1.52 V vs RHE (Figure 12k).

The in situ growth of metal nanoparticles on the surface of GDY to provide more active sites for the HER has been a proven strategy for preparing high-performance catalysts. Nb rarely reported for HERs was reported by Li and co-workers.[124] As the preparation routes show in Figure 13a, bimetallic oxide nanoparticles composed of Nb and Rh were synthesized on a GDY. Next, Nb_yRhO_x nanoparticles with a diameter of approximately 2 nm were uniformly dispersed on a 3D graphdiyne nanowall. Optimal HER activity was achieved at a Nb/Rh ratio of 0.23, which demonstrated that selective in situ growth of metal atoms could result in an asymmetric electron distribution and high catalytic activity and stability (Figure 13b−c). Dai and co-workers reported the tunable activity of graphdiyne on HER, which could be attributed to the different interaction strength of metal ions and graphdiyne (Figure 13d−g).[125] The construction of active sites is not exclusively provided by the metal nanoparticles grown in situ on GDY. Modification of GDY is another way to enhance HER performance. Zhang and co-workers reported a physical clipping strategy for reforming delocalized electronic states of GDY.[126] After a period of plasma radiation under an Ar atmosphere, the periodic interruption of Csp−Csp^2 bonds was triggered (Figure 13h). The increase in the D band in the Raman spectrum and the decrease in the sp-C occupation in the XPS spectrum demonstrated disruption of the ordered structure in graphdiyne. The long-range periodically ordered structure was not disrupted (Figure 13i). Therefore, after 120 s of plasma irradiation without destroying the base structure, I-GDY with more defects and active sites exhibited the best HER activity (Figure 13j). Dai and co-workers found that nonprecious metal ions functionalized exfoliated GDY (EGD) nanocomposites (EGD-M^{n+}) exhibited high and tunable catalytic performance toward the HER and found that metal ions with stronger interactions with EGD could replace those with weaker interactions.[125] The HER catalytic activity for EGD-M^{n+} catalysts could be reversibly tuned by reversible cycle coordination with anions of different interaction strengths with EGD. This provides a convenient and facile strategy for the design and synthesis of efficient catalysts of practical significance.

The oxygen evolution reaction (OER) is another important half reaction for water splitting. Li and co-workers reported that the morphological and electronic structures of a Ni complex (CT) were modulated by GDY. A Ni 2P XPS spectrum illustrated that the ratio of Ni^{3+} in CTNS/GDY was greater than that in bulk CT.[127] Electrochemical test results and theoretical calculations demonstrated that modulation by GDY enhanced the OER performance and decreased the reaction barrier. Huang et al. developed the cocoordinated monomer to synthesize a 2D graphdiyne analog (Co-PDY) via the Glaser-Hay coupling reaction. The Co center of the 4N-coordination in the metalloporphyrin structure provided high OER activity.[128] The charge transfer of nonmetallic heteroatoms by GDY could also effectively improve the OER activity. Wang and co-workers reported an N,S-heteroelement-doped GDY metal-free catalyst via an improved pyrolysis method. Compared with other N configurations, sp-N played the most important role in enhancing the OER activity.[129] In addition, N,S-codoped GDY presented excellent OER performance, which was better than that of most reported metal-free catalysts. The in situ growth of metal oxide nanoparticles on graphdiyne heterojunction catalysts also resulted in excellent performance of the nanoparticles. Recently, Li and co-workers synthesized a highly uniform size distribution of IrO_x on GDY. The experimental results showed that the Ir valence state of the small IrO_x nanoparticles (diameter of approximately 1.5 nm) decreased, which was attributed to charge transfer in GDY. In the acidic electrolyzer, IrO_xQD/GDY showed the best OER activity, with the smallest overpotential of 236 mV at 10 mA cm^{-2}, which could be attributed to the strong interactions between GDY and IrO_xQD.[130] Recently, Qi et al. synthesized heterogeneous $MnCo_2O_4$/GDY arrays with a nanowire structure. The special core/shell-nanowire structure and the synergistic interaction between $MnCo_2O_4$ and GDY improved the electrical conductivity, promoted mass/ion transport and gas emission, and exposed more active sites, which led to an improvement in the catalytic activity and long-term stability of the electrocatalysts. The alkaline water electrolyzer assembled using NW-$MnCo_2O_4$/GDY showed high performance, requiring only 1.47 to reach a current density of 10 mA cm^{-2}.[131] Li and co-workers reported ultrathin GDY-wrapped iron carbonate hydroxide nanosheets for efficient water splitting. The electrocatalyst could drive 10 mA cm^{-2} at 1.49 V.[132] Yu et al. coated ultrathin graphdiyne layers on NiO nanocubes, which exhibited excellent overall water splitting performance.[133] Further, Chen et al. reported the FeOOH@GDY with excellent overall water splitting. The cell voltages reached only 1.43 V at 10 mA cm^{-2}, which had no significant decrease after an over 400 h test.[134]

The photocatalytic water-splitting system involves three sequential steps: (i) absorption of photons with energies higher than the band gap of the photocatalysts to excavate electron−hole pairs, (ii) charge separation and transport of photoexcited carriers, and (iii) surface hydrogen and oxygen evolution reactions based on the catalysts. The water-splitting catalytic performance of graphdiyne-based photocatalysts is usually improved by two strategies: tuning the electronic band gap to enhance photon absorption and increasing charge separation and transfer rates.[15,135] Li et al. reported an H-GDY/TiO_2 heterojunction catalyst, which achieved a high photocatalytic hydrogen generation (6200 μmol h^{-1} g^{-1}).[136] After the H substitution, the narrow electronic band gap of the GDY was tuned to 2.5 eV. A suitable band alignment between H-GDY and TiO_2 efficiently promoted the absorption of photons and photogenerated carriers. Zhang et al. synthesized a MoS_2-CdS/GDY photocatalyst, and the hydrogen production rate could reach 17.99 mmol g^{-1} h^{-1}.[137] One-dimensional MoS_2 tips effectively promoted charge separation. The in situ growth of 2D GDY nanosheets on the surface of MoS_2-CdS nanodumbbells attracted photoelectron and hole transport outward, resulting in a high photocatalytic reaction rate and resistance to photocorrosion. Wang et al. reported the GDY@C_3N_4 synthesized by a deprotection-free approach. The photocatalytic hydrogen yield of GDY@C_3N_4 was 15.6-fold of that of pristine C_3N_4.[138] Mao and co-workers reported an Ag_3PO_4/GDY-based Pickering emulsion for water photooxidation and photodegradation of methylene blue.[139] As an electron acceptor, graphdiyne transported photogenerated electrons from Ag_3PO_4, promoting water oxidation on the Ag_3PO_4 active sites. In the system with a sensitizer and a sacrificial reagent, Jin and co-workers synthesized the CuBr-assisted graphdiyne p−n heterojunction photocatalyst, which significantly increased the transfer rate of electron−hole pairs and enhanced the photogeneration of hydrogen.[140] Shen et al. designed and prepared a dehydrobenzoannulene-based three-dimensional graphdiyne using Pt nanoparticles as the cocatalyst. The fiber-like structure exhibited an apparent quantum efficiency of 4.68%.[141]

Compared with electrocatalysis, photoelectrocatalytic water splitting could reduce energy consumption and environmental pollution attributed to photogenerated electrons. Regarding solar energy utilization, high reaction rates and yields are more relevant for practical

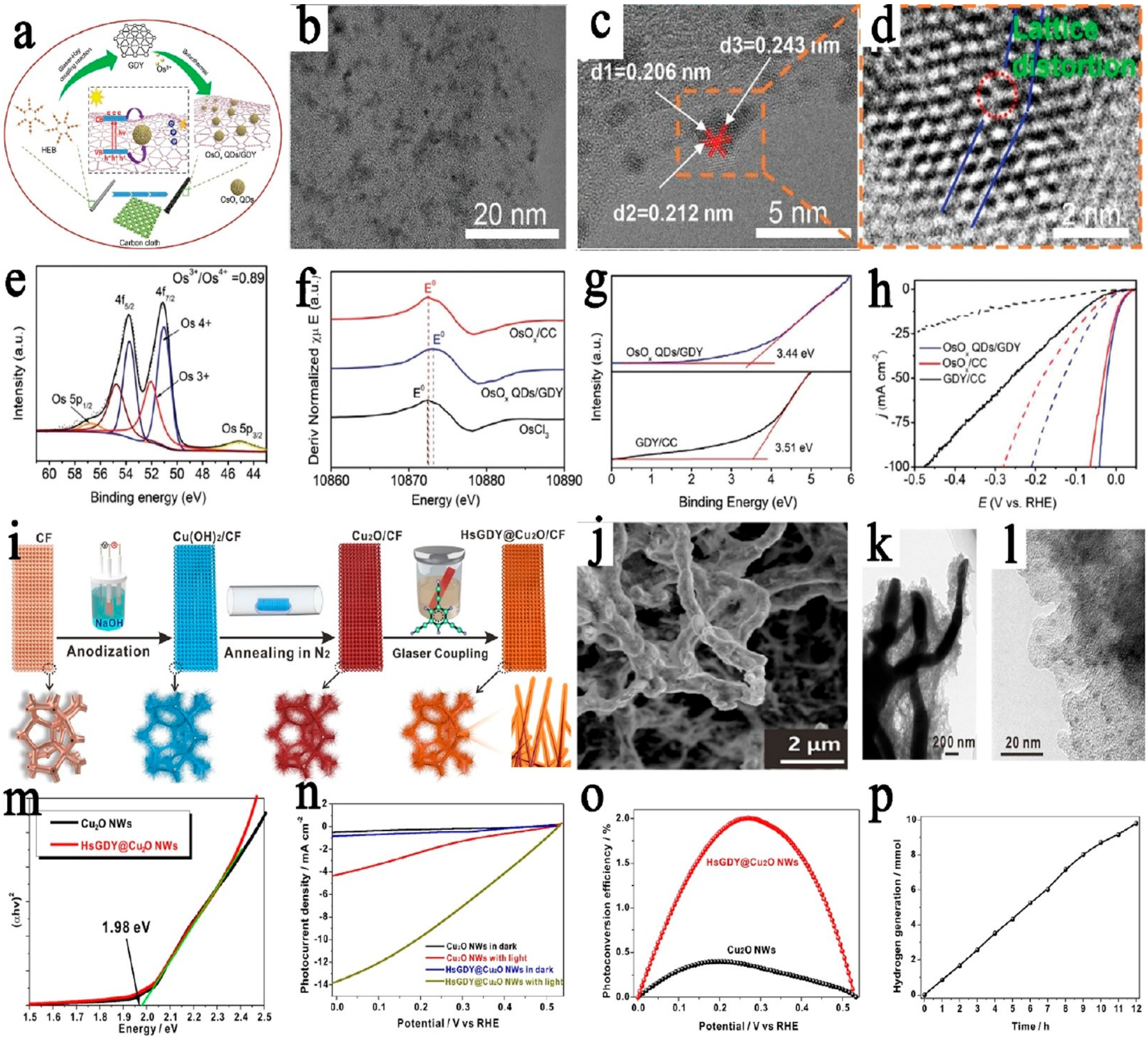

Figure 14. Photoelectrocatalytic water splitting. (a) Schematic diagram of the synthesis of OsO$_x$ QDs/GDY. TEM (b) and HRTEM (c−d) images of the OsO$_x$ QDs/GDY. The XPS XPS Os 4f spectra (e) and the first-derivative of XANES (f) of samples. (g) UPS spectra for the OsOx QSs/GDY and GDY/CC. (h) HER polarization curves of samples before and after the illumination. Reproduced with permission from ref 142. Copyright 2021, Wiley. (i) Schematic diagram of the synthesis of HSGDY@Cu$_2$O. SEM (j), TEM (k), and HRTEM (l) images of HSGDY@Cu$_2$O. (m) Tauc plots of samples. (n) LSV plots of samples in dark or solar light. (o) Photoconversion efficiency of samples. (p) Photocatalytic hydrogen generation at 0 V vs RHE. Reproduced with permission under a Creative Commons CC-BY License from ref 143. Copyright 2022, Springer Nature.

applications than photocatalysis. Du et al. reported a uniformly distributed OsO$_x$ QD/GDY catalyst for photoinduced electrocatalysis (Figure 14a).[142] Graphdiyne induced charge transfer in the OsO$_x$ QDs GDY, resulting in a lattice distortion and high-coordination of the Os (Figure 14b−d). XPS and XANEs spectra of Os showed that the proportion of the Os^{4+} in the OsO$_x$ QDs GDY was higher than that in the OsO$_x$/CC (Figure 14e−f). Owing to the excellent photogenerated charge and hole transport capacity of graphdiyne, the photoelectrocatalytic performance of the catalyst was significantly enhanced with the illumination of the electrodes (Figure 14g−h). Zhang and co-workers fabricated an encapsulation strategy for efficiency photoelectrocatalysis water splitting (Figure 14i).[143] Cu$_2$O quantum dot active sites were in situ prepared on the HSGDY during the encapsulation of Cu$_2$O NWs (Figure 14j−l). With a high photocurrent density of 12.88 mA cm^{-2}, the HsGDY@Cu$_2$O exhibited an impressive hydrogen yield of 218.2 ± 11.3 μmol h^{-1} cm^{-2} (Figure 14m−p). Recently, Li and co-workers synthesized the structure of sp-C−Mo/O bonds in the GDY@MoO$_x$ catalysts.[144] The high photoelectrocatalytic activity over a wide pH range (0−14) could be attributed to the mixed valence of Mo and fast charge-transfer process in GDY@MoO$_x$. Wu and co-workers fabricated ultrathin CoAl-LDH (CO_3^-) nanosheets on superhydrophilic graphdiyne for highly efficient water oxidation.[145] After plasma treatment, the hydrophilicity of graphdiyne was improved, and electron transportation at the interface was enhanced. Regardless of the growth of CoAl-LDH (CO_3^-) nanosheets for electrocatalysis or the fabrication of a heterojunction material with BiVO$_4$ for photoelectrocatalysis, the superhydrophilic graphdiyne catalyst exhibited excellent performance.

4.4. Other Catalytic Reactions.

The oxygen reduction reaction was the fundamental half-reaction in a fuel cell. Platinum and other noble metal catalysts exhibited the best performance in the ORR reaction in the reported literature but were limited by the insufficient resources and the high cost in the commercial mass market of fuel cells. GDY-based catalysts as a two-dimensional carbon material provided a route for a high-performance oxygen reduction reaction. Li and co-workers reported the metal-free catalyst- sp-N-doped graphdiyne with

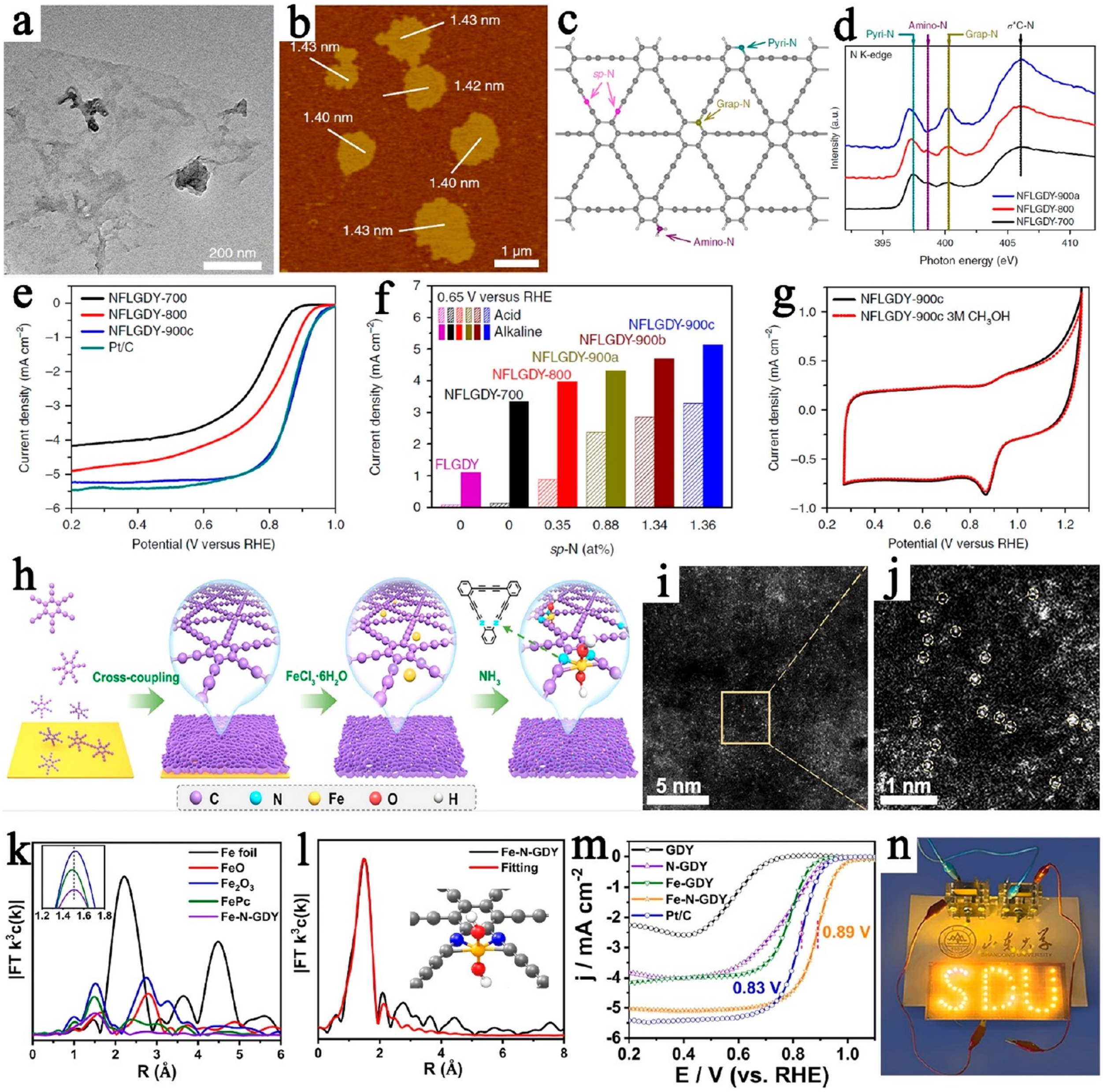

Figure 15. Oxygen reduction reaction. TEM (a) and AFM (b) images of FLGDYO. (c) Geometries of the N atoms in NFLGDY. (d) N K-edge XANES of samples. (e) ORR polarization curves of samples. (f) Current densities of the ORR at 0.65 V (vs RHE) for samples. (g) Cyclic voltammetry curves of NFLGDY-900c in O_2-saturated 0.1 M $HClO_4$. Reproduced with permission from ref 146. Copyright 2018, Springer Nature. (h) Schematic synthesis of Fe-N-GDY. (i−j) HAADF-STEM images of Fe-N-GDY. EXFAS spectra (k) and fitting curves (l) of Fe-N-GDY. (m) ORR polarization curves of samples. (n) Optical image of LED lamps powered by the Fe-N-GDY based battery. Reproduced with permission from ref 147. Copyright 2022, Wiley-VCH.

the special form of nitrogen doping moieties.[146] The ultrathin nanosheets with a negative surface of FLGDYO were prepared from BGDY through a solution-based chemical oxidation exfoliation method (Figure 15a,b). XPS spectra and XAFS spectra revealed that sp-N atoms were the main doped components in the NFLGDY catalyst (Figure 15c,d). In polarization curves, the NFLGDY-900c catalyst exhibited a similar current density to the Pt/C electrolyte (Figure 15e). And the excellent performance of the metal-free catalyst could be attributed to the beneficial effect for O_2 absorption and reduction at the sp-N sites (Figure 15f). The good stability and methanol resistance in both alkaline and acidic solutions (Figure 15g) could broaden the scope of the application. Recently, Li et al. reported the other anchoring sites of the Fe-N-GDY catalyst for a high efficiency oxygen reduction reaction (Figure 15h).[147] Experimental results revealed that the chemical environment of iron atoms was regulated by the coordination sp-C and sp-N in the N-doping graphdiyne (Figure 15i−l). Theoretical calculation results demonstrated that the Fe active sites optimized the O_2 absorption energy and accelerated the oxygen reduction reaction kinetics. As shown in Figure 15m−n, Fe-N-GDY which exhibited the excellent performance of the ORR was successfully applied in a zinc-air battery with high power density. Xu and co-workers synthesized the F-doped γ-graphyne/PtPd nanocomposite for the efficient oxygen reduction. The doped fluorine atoms changed the electron environment and the charge distribution of γ-GY, improving the catalyst activity of the PtPd nanocomposite.[148]

As another important half reaction, the performance of the anode oxide reaction determined the cell voltage, output power, and stability of fuel cells. Li and co-workers reported the $PtCl_2Au(111)$/GDY catalyst which has shown high mass activity and stability for methanol oxidation reactions.[149] The catalyst was synthesized by epitaxial growth

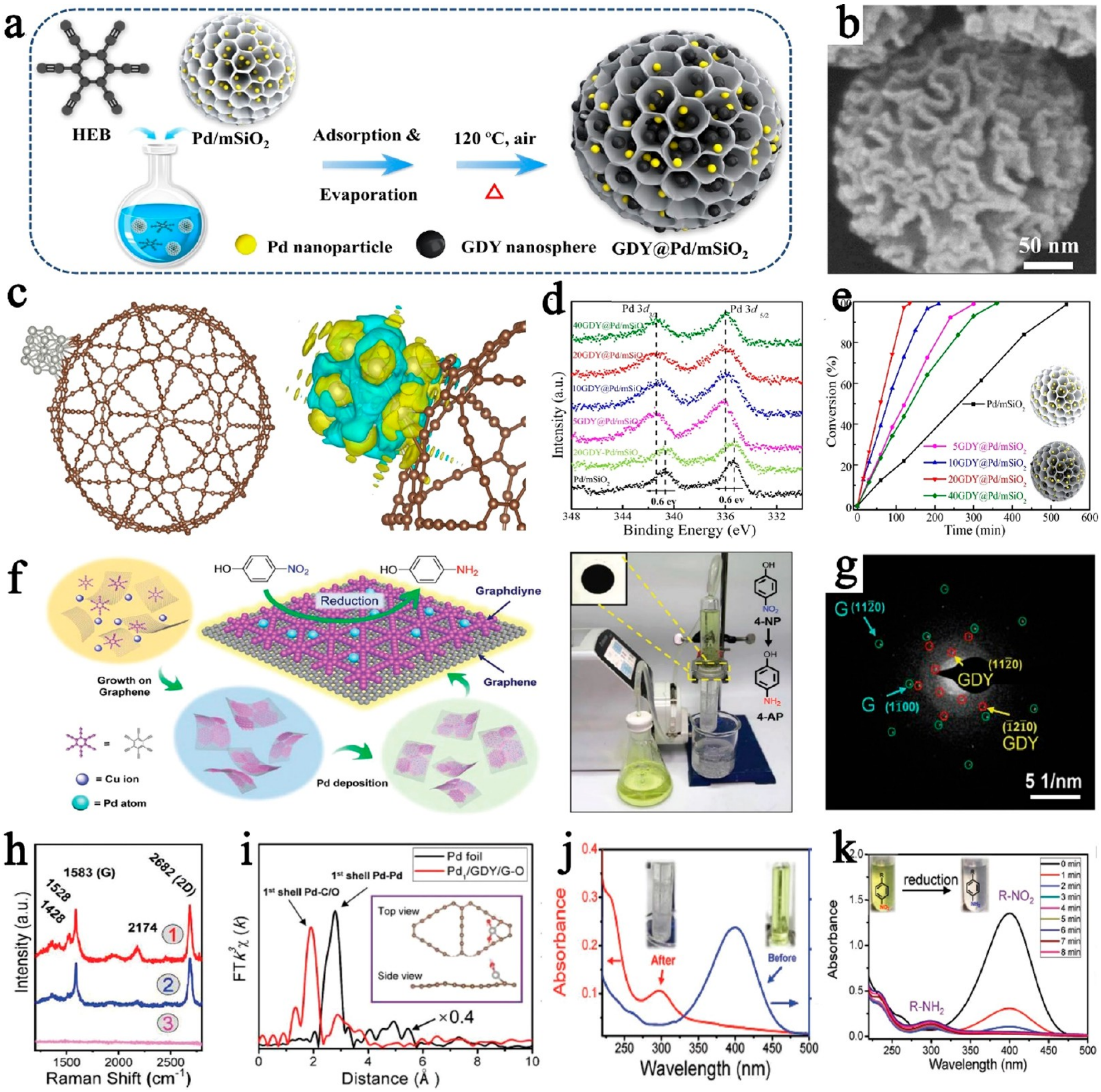

Figure 16. Small molecule conversion. (a) Schematic illustration of the synthesis route of GDY@Pd/mSiO$_2$. (b) SEM image of GDY@Pd/mSiO$_2$. (c) Interaction model of Pd/GDY. (d) Pd 4d orbital distribution and the d-band centers of samples. (e) The conversion of benzaldehyde on various catalysts. Reproduced with permission from ref 151. Copyright 2022, Wiley-VCH. (f) Schematic diagram of the Pd$_1$/GDY/G synthesis. (g) SEAD image of GDY/G. Raman (h) and EXAFS (i) spectra of Pd$_1$/GDY/G. (j) UV−vis spectrum and optical images of the samples. (k) UV−vis absorption spectra during the catalytic reaction. Reproduced with permission from ref 152. Copyright 2019, Wiley-VCH.

of gold quantum dots on platinum chlorine species on graphdiyne. Both structure characterizations and theoretical calculations revealed that the excellent catalytic performance could be attributed to the chlorine introduced to modify the d-band structure of Pt and suppression of the CO poisoning pathway of the MOR. The mass activity of this catalyst could reach 175.64 A mg^{-1} for methanol oxidation reactions and 165.35 A mg^{-1} for ethanol oxidation reactions. Further, Hui et al. synthesized the zerovalent platinum atomic catalyst (Pt/NGDY) for MOR.[85] The synergistic contributions of different Pt sites promoted the electron transfer to intermediates in MOR. Li and co-workers synthesized single nickel atom alloyed platinum nanocrystals on graphdiyne. Visualization of structure and content of valence states changed by the composition tunability brought high mass activity and current density in MOR.[150] Yu et al. demonstrated an important role of GDY as a wettability modifier for enhancing hydrogenation catalysis.[151] After a certain amount of GDY nanospheres were loaded, the silica mesoporous channels became superhydrophilic, which allowed gaseous H_2 to be stored directly inside (Figure 16a,b). XPS results illustrated that GDY nanospheres could change the electronic structure of the Pd nanoparticles by strong d-π interactions (Figure 16c,d). The hydrogenation was impressively improved by a 4.3-fold improvement compared with the Pd/silica catalyst (Figure 16e). Li et al. synthesized palladium SACs anchored in an elaborate graphene/graphene heterojunction (Pd1/GDY/G) (Figure 16f−h).[152] Pd1/GDY/G exhibited high catalytic performance for the reduction reaction of 4-nitrophenol. Theoretical calculations indicated that graphene in the GDY/G heterostructure played a key role in improving the catalytic performance due to the electron transfer process, which arises from the gap between the Fermi level of graphene and the conduction band minimum of GDY/G and the gap between the conduction band minima of GDY (Figure 16i−k). Yang et al. also reported the subnanometric Pd/GDY catalysts for efficiency reduction of nitro-

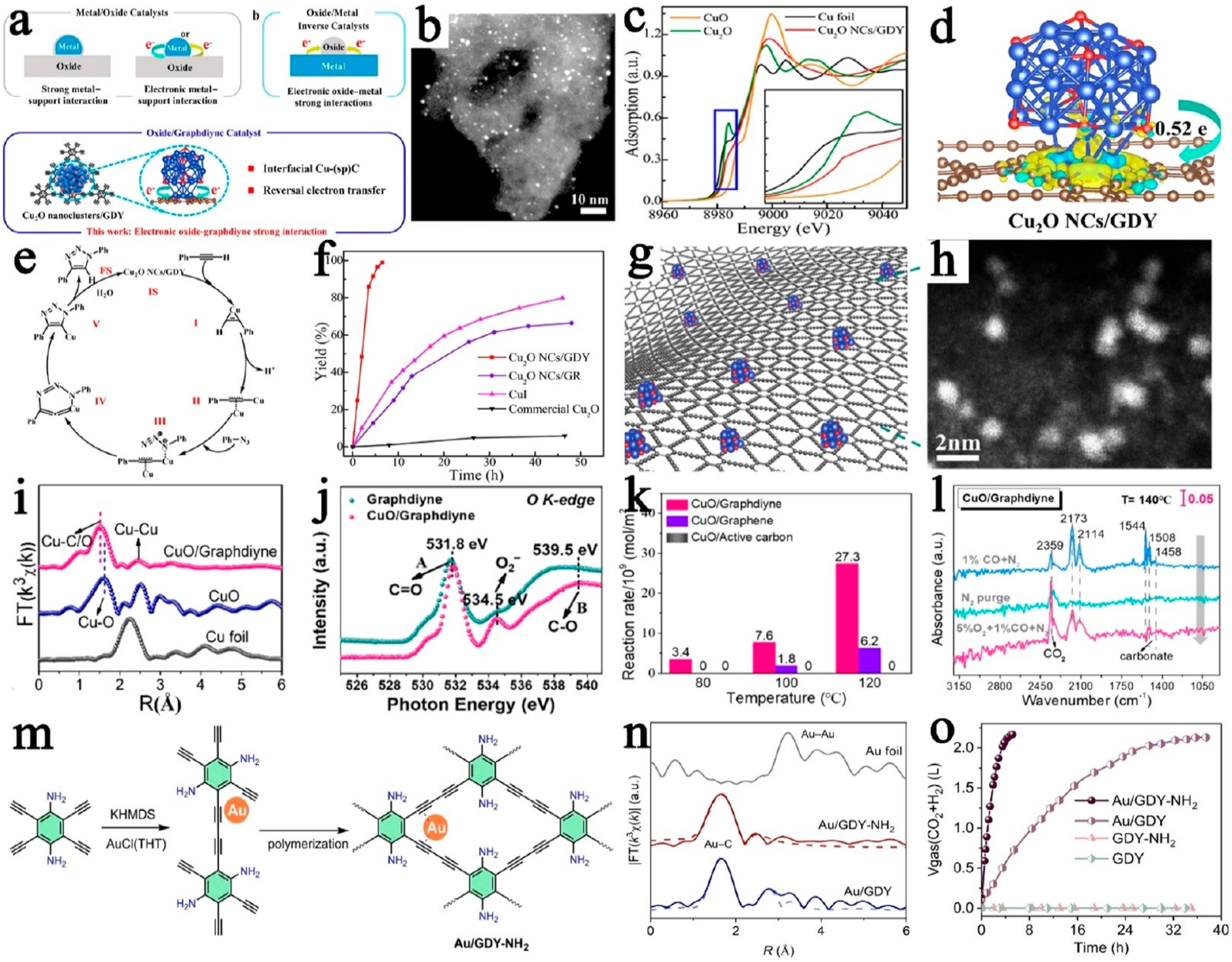

Figure 17. Other catalytic reactions. (a) Schematic diagram of the synthesis process of Cu_2O NCs/GDY. STEM image (b) and Cu K-edge XANES spectra (c) of Cu_2O NCs/GDY. (d) Difference charge density of Cu_2O NCs/GDY. (e) The catalyst reaction pathway. (f) Time-dependent catalyst performance. Reproduced with permission from ref 154. Copyright 2023, American Chemical Society. (g) Schematic illustration of CuO/graphdiyne catalyst. (h) HAADF-STEM images of CuO/graphdiyne. (i) XANES spectra of CuO/graphdiyne. (j) O K-edge spectra of samples. (k) Catalytic reaction rate of CuO/graphdiyne. (l) In situ FTIR spectroscopy. Reproduced with permission from ref 155. Copyright 2022, American Chemical Society. (m) Synthetic scheme for Au/GDY-NH_2. (n) XANES spectra of samples. (o) Dehydrogenation of formic acid with different catalysts. Reproduced with permission from ref 159. Copyright 2023, Wiley-VCH.

arenes. The deposition and stabilization by graphdiyne improved the activity and stability of electrocatalyst.[153]

GDY-based catalysts can also realize the efficient conversion of small molecules. Yu et al. reported a Cu(I)-catalyzed azide−alkyne cycloaddition reaction by Cu_2O NCs/GDY (Figure 17a).[154] The charge transfer at the interface stabilized Cu(I) species and optimized adsorption energy for reactants/intermediates (Figure 17b−d), resulting in high performance for a broad scope of substituted acetylenes (Figure 17e−f). Guo and co-workers fabricated the subnanocluster CuO/graphdiyne for an efficient CO oxide (Figure 17g−h).[155] XFAS results demonstrated that the adjacent sp-hybridized C bonds to Cu sites at the interface, which was the key structure that effectively regulated the O_2 activation process (Figure 17i−j). The prepared subnanocluster CuO/graphdiyne catalysts exhibited the highest CO oxidation activity, converting 50% of CO at around 133 °C (Figure 17k). In situ FTIR spectroscopy and DFT results showed that adjacent sp-hybridized C was more favorable to facilitate the rapid dissociation of carbonate without overcoming any energy barrier (Figure 17l). Further, Gu et al. reported hemin molecules anchored uniformly on GDY with single site configuration, delivering a O^{2-} production rate of 35.7 and 2.3 times than that of respective hemin and hemin/graphene.[156] Qi and co-workers demonstrated the preparation of boron-doped and ketonic carbonyl (−C═O) group-enriched graphdiyne with enhanced peroxidase-like activity.[157] SGDY nanosheets with piezoelectrically enhanced enzyme-mimicking activity were synthesized by Zhu et al. and co-workers. The incorporation of sulfur minimized the band gap, improved the charge distribution of the SGDY network, and increased the density of active sites, which resulted in significant peroxidase-like activity.[158] Liu et al. reported the Au SAs anchored on amino-substituted graphdiyne for efficient formic acid dehydrogenation (Figure 17m−n).[159] After 5 h of catalyst reaction by Au/GDY-NH_2, the conversion of formic acid could reach over 99% (Figure 17o). Mao and co-workers fabricated the selective electrocatalysis by interfacing redox-active methylene green and graphdiyne. The oxidation of NADH was efficiently accelerated at low overpotentials by rapid self-exchange of interlayer MG dimers, while AA oxidation relied on the hindering of direct electron tunneling by GDY.[160,161]

5. GRAPHDIYNE-BASED ENERGY STORAGE AND CONVERSION MATERIALS

5.1. Lithium Ion and Other Alkali Metals Ion Battery.

GDY has been demonstrated to be an ideal material for metal batteries with a theoretical capacity of 744 mAh g^{-1} and multilayer theoretical capacity up to 1117 mAh g^{-1} (1589 mAh cm^{-3}). Besides, the structure of GDY is more conducive to the in-plane and out-of-plane diffusion and transmission of lithium ions, thus leading to a very good multiplier

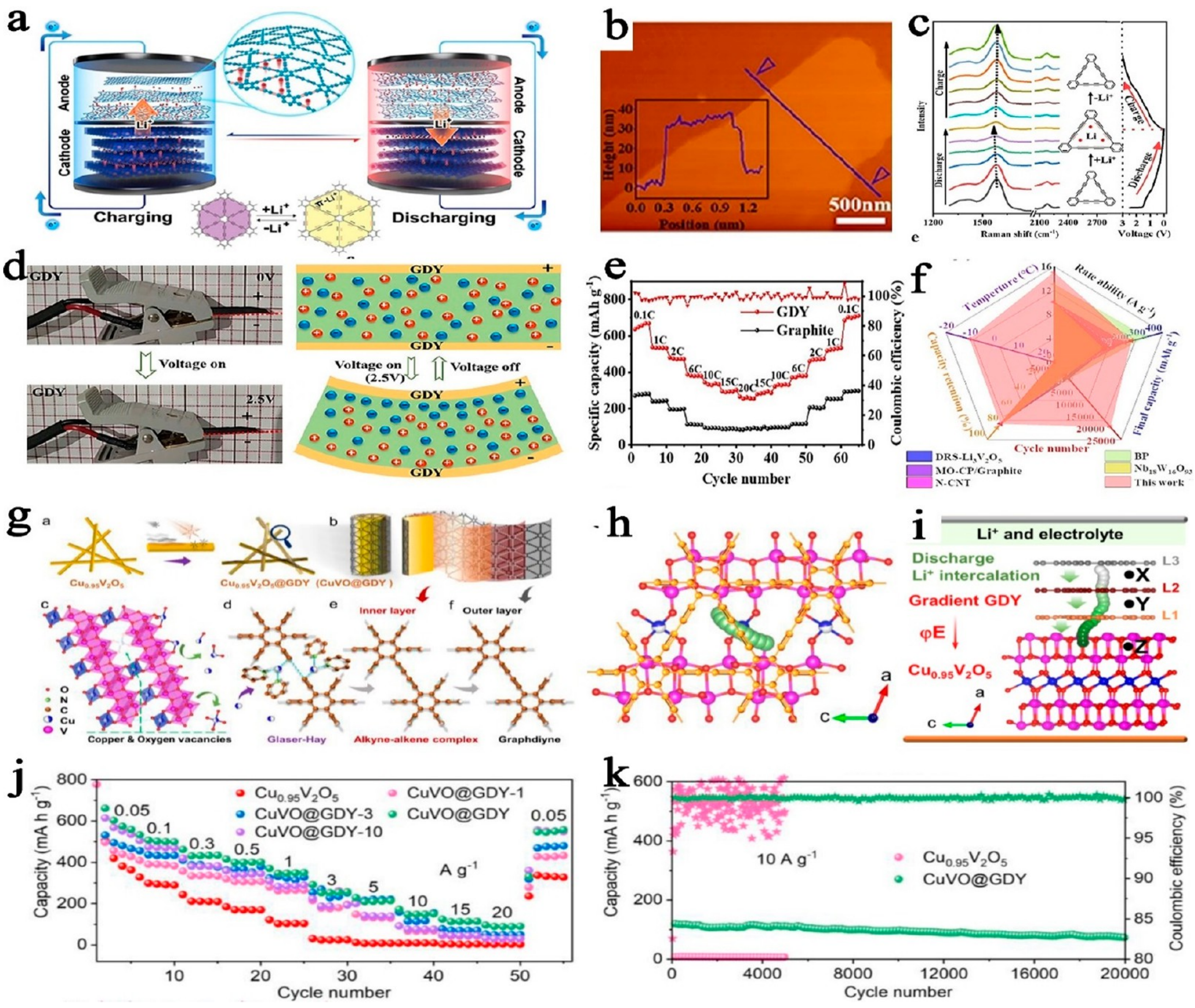

Figure 18. GDY anodes in a lithium-ion battery. (a) Schematic representation of self-expanding Li-ion transport channels in GDY anodes. (b) AFM image of GDY. (c) In situ Raman spectra of GDY anodes. (d) The deformation experiments of GDY electrode. (e) The rate performance of GDY and graphite anodes. (f) Performance comparison of full cell. Reproduced with permission from ref 176. Copyright 2022, Wiley-VCH. (g) Schematic illustration of the synthesis of $Cu_{0.95}V_2O_5$@GDY. (h) Scheme of the Li-ion diffusion pathway. (i) Schematic diagram of Li intercalation. (j) Rate performance of samples. (k) Cycling performance of samples. Reproduced with permission from ref 177. Copyright 2022, Wiley-VCH.

performance.[162−173] The high efficiency lithium storage performance of graphdiyne was achieved through the Li-ion interlayer insertion/extraction and surface absorption/desorption methods.[174] Jang et al. calculated that the practical specific capacities of Li-intercalated multilayer graphdiyne could reach up to 2719 mAh g^{-1}.[175] Based on the special properties of GDY, we put forward the concept of "alkyne-alkene transition", especially in the aspect of lithium fast charge, to change the traditional mechanism of lithium fast charge and establish a special mode of lithium fast charge. Our group reported the self-expanding lithium-ion transport channels for fast-charging LIBs (Figure 18a).[176] Experimental results indicated that Li^+ reversible binding with the acetylenic bond in graphdiyne led to the transition between the alkyne-alkene complexes (Figure 18b−c). Theoretical calculation revealed the size expansion of the covalent bond network and the pores after lithium was embedded at the anode. Li ions interacted with the alkyne bonds of the GDY to form an alkyne-alkene complex structure. The deformation of the GDY-electrode sheet toward the positive electrode side can be observed in Figure 18d. The excellent lithium transport and storage mechanism endows high capacity and good capacity retention under fast-charging conditions (Figure 18e−f). More recently the $Cu_{0.95}V_2O_5$@GDY anodes with a large abundance of GDY induced Cu/O vacancies fabricated for fast-charging batteries was reported by our group (Figure 18g).[176] HAADF-STEM images demonstrated the absence of Cu atoms in $Cu_{0.95}V_2O_5$ after in situ growth of gradient graphdiyne. The strong interaction at the heterointerface was determined by XPS depth profiling (Figure 18h−i). The enlarged Li storage sites and improved ion transport kinetics were accomplished by the Cu/O vacancies. In 10 A g^{-1} large current fast charging, the specific capacity of the full cell could reach 132 mAh g^{-1} (Figure 18j−k).

In order to gain in-depth understanding of the structural evolution and reaction mechanism of the electrode/electrolyte interface during cycles, Wan and co-workers studied the evolution of the solid electrolyte interphase (SEI) and lithium deposition on GDY and NGDY electrodes by the in situ optical microscopy and atomic force microscopy (Figure 19a).[153] Experiment results revealed that the SEI layer on N-doped graphdiyne grew in a spherical NP shape rather than a flocculent-like manner (Figure 19b−d). These results could be attributed to the uniformized Li deposition and stabilized interfaces affected by the N-doped sites, promoting homogeneous SEI evolution (Figure 19e−f). Another key strategy for enhancing the security of LIBs is to inhibit the growth of lithium dendrites. Zuo et al. reported the spontaneously splitting copper nanowires into quantum dots (CuQDs) on GDY for suppressing lithium dendrites by in situ growth of GDY on

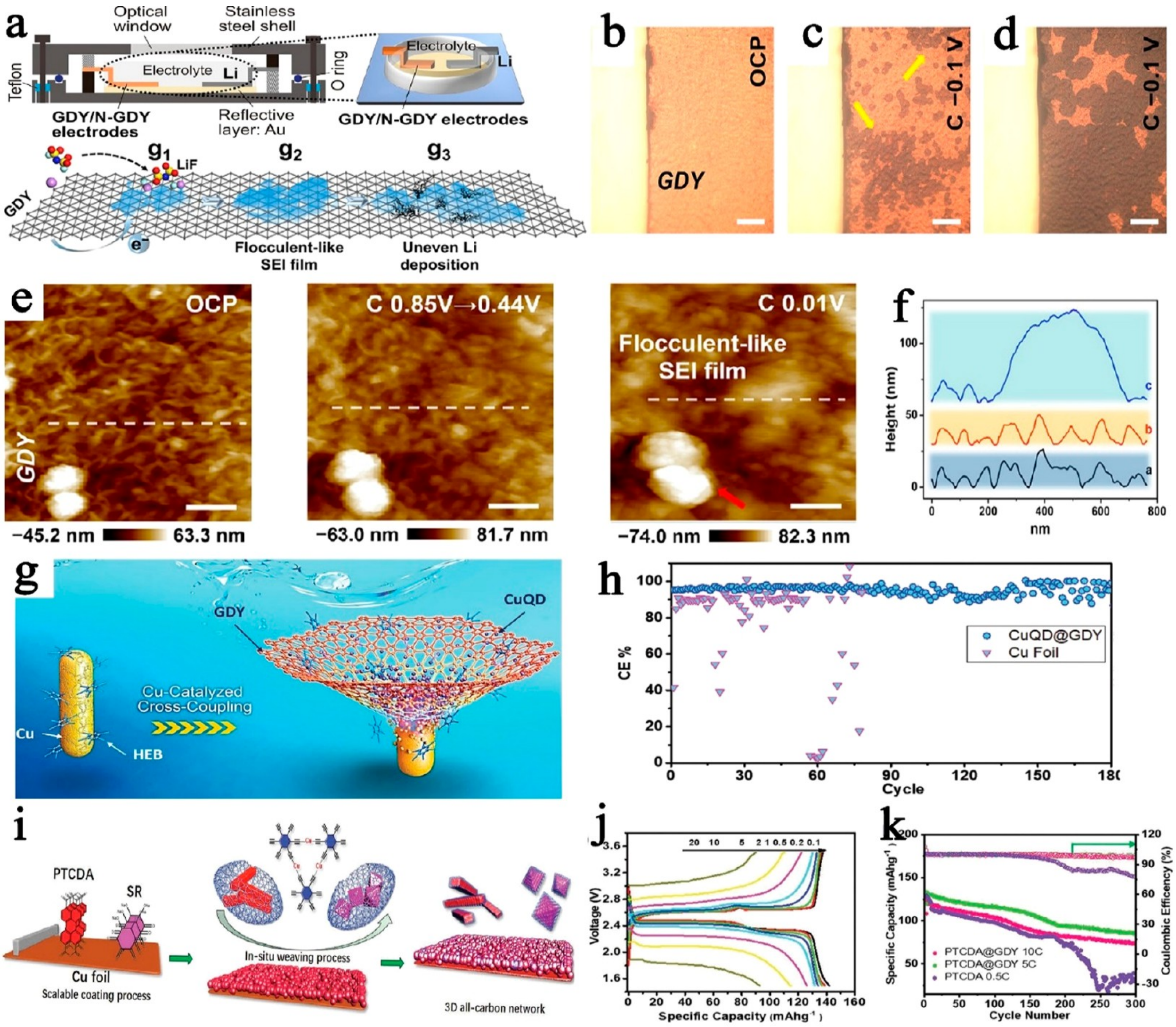

Figure 19. Graphdiyne protection electrodes. (a) Schematic diagram of in situ electrochemical OM setup and the process of Li deposition. (b–d) Part of in situ OM images of graphdiyne electrode in the charging process. (e) AFM images of GDY electrode at different potentials. (f) Height section profiles in (e). Reproduced with permission from ref 183. Copyright 2022, American Chemical Society. (g) Schematic illustrations of in situ growth of GDY on Cu nanowires. (h) Variations of Coulombic efficiency during the long-term testing. (i) Schematic process of in situ growth of GDY nanocoat. (j) charge/discharge polarization curves of PTCDA@GDY. (k) Long-term cycling performance of samples. Reproduced with permission from ref 182. Copyright 2020, Wiley-VCH.

the surface of Cu nanowire (Figure 19g).[178] The nanosized Cu distributed on GDY efficiently inhibited the nonuniform nucleation and dendric growth of metallic Li, thus efficiently suppressing the Li dendrites and enhancing the overall performances (Figure 19h). Wang et al. reported chlorine-substituted GDY with more transfer tunnels for Li ion transfer. The highly distributed substitutional chlorine atoms could synergistically stabilize the Li intercalated in the Cl-GDY framework and thus generate more storage Li sites.[179] Moreover, Huang and co-workers reported the use of fluoride-GDY as a free-stranding electrode could achieve high reversible capacity (1700 mAh g^{-1}) and extreme cycle performance, which could be attributed to the reversible transition from C−F covalent bonds to ionic bonds.[180] Owing to the high affinity with lithium, GDY presents a promising capability for stabilizing Li metal anodes.[181] Qi and co-workers showed that the vertically aligned GDY allowed for dendrite-free, columnar deposition of lithium for Li metal batteries with high safety and high energy density. In addition to the protection of the electrodes, graphdiyne could also be an all-carbon protective layer for electrolytes. Wang et al. reported a universal strategy for protecting the metal oxides from irreversible changes.[99] The high-quality graphdiyne nanosheet was synthesized on the surface of metal oxides with different dimensions and morphology. Experimental results and theoretical findings indicated that the GDY protection layer holds incomparable promises for stabilizing the structure and interface of the electrode. The graphdiyne protection strategy was still effective in cathode materials.[174,182] Catalyzed by Cu substrate, GDY was seamlessly coated on the organic cathode materials, forming a three-dimensional network (Figure 19i), resulting in an excellent long-term stability for the organic cathodes (Figure 19j−k).

Lithium−sulfur batteries have a higher theoretical energy density (reach 2600 W h kg^{-1}) than current Li-ion batteries. But the shuttle effect of polysulfides seriously limited its development and application. Wang et al. fabricated a Nafion@GDY core−shell hollow structure to store sulfur and offer active epicenters.[184] The S elemental distribution mappings revealed that sulfur had infiltrated uniformly into the Nafion@GDY network. In situ Raman spectra and theoretical simulation demonstrated that Nafion could increase the retention time of polysulfide and restrain the polysulfide migrates, resulting in excellent long-term stability. Li and co-workers fabricated a graphdiyne-like porous organic framework as sulfur conversion cathodes.[185] The reversible short sulfur chains generated abundant acetylenic bonds in nanochannels. These strategies showed that the GDY-based cathode

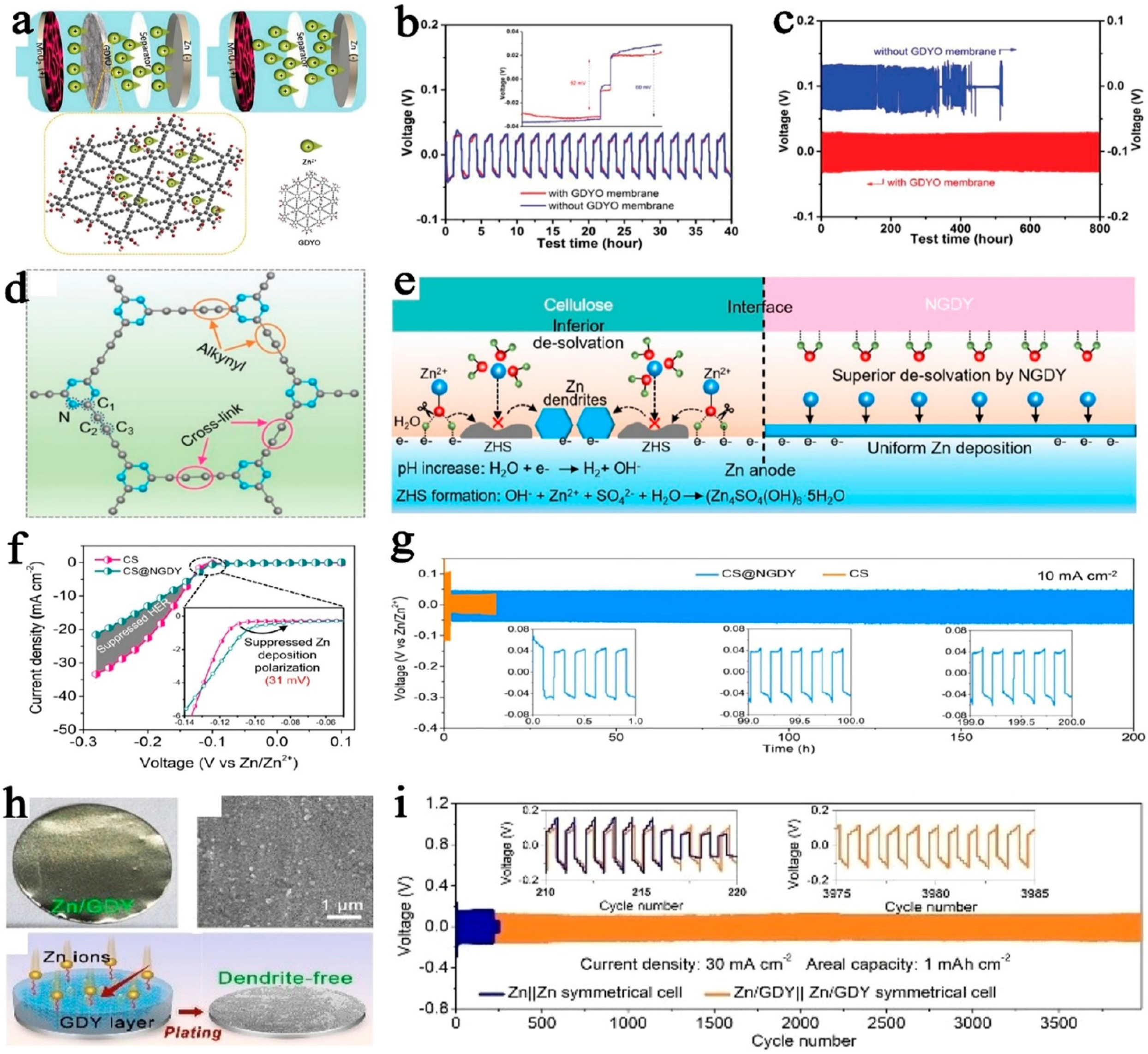

Figure 20. Zinc ion battery. (a) Schematic diagram of Zn-ion batteries. (b−c) Zn stripping/plating from Zn/Zn symmetrical cells. Reproduced with permission from ref 195. Copyright 2020, Wiley-VCH. (d) Digital image of NGDY on CS separator. (e) Schematic diagram of the NGDY-assisted stabilization of Zn electrolyte. (f) Polarization curves of water decomposition and deposition. (g) Voltage−time curves of the Zn battery. Reproduced with permission from ref 196. Copyright 2022, Wiley-VCH. (h) Schematic process of Zn plating on GDY. (i) Voltage profiles of Zn symmetric cells. Reproduced with permission from ref 97. Copyright 2023, Wiley-VCH.

could prevent the shuttle effect before the polysulfide migrate. Further, Zhang et al. reported that the rechargeable Li-CO_2 batteries with the metal-free GDY as cathode could reach 18416 mAh g^{-1}, and a full Li-CO_2 battery achieved the excellent energy density of 165.5 Wh kg^{-1}.[186] Graphdiyne was reported as the sodium ion batteries substrate interconnected with molybdenum disulfide by Huang, Zhang and co-workers.[187] Graphdiyne improved the ion diffusion and electron transfer rate, with a discharge capacity reaching 328 mAh g^{-1} at 1A g^{-1}. Li and co-workers reported that the BGDY has high reversible capacity with 180 mAh g^{-1} even after 4000 cycles.[188] Yang and co-workers reported the yolk−shell structure of Sb@Void@GDY nanoboxes with good long-term stability of 500 cycles at 1A g^{-1}.[189]

Restricted by the larger radius of potassium ions, potassium-ion batteries (KIBs) were hampered by the slow diffusion rate, huge volume expansion, and unstable interface. Graphdiyne frameworks were a perfect potassium storage and transfer structure. Yi et al. reported the graphdiyne framework exhibited high performance as the KIB anode.[190] The specific capacity was achieved at 505 mAh g^{-1} at 50 mA g^{-1}. In situ Raman spectroscopy and XPS measurements confirmed good reversibility with a capacity retention of 90% after 2000 cycles. Zhang, Sun, and co-workers reported the NC@GDY decorated with Cu quantum dots for dendrite-free potassium anodes.[191] The NC@GDY synthesized by in situ growth of graphdiyne on NC polyhedrons was directly coated on Al foil for the anode material. Experimental results and theoretical calculations revealed potassium ions uniformly embedded into NC@GDY without potassium dendrite generation, which could be attributed to the high potassiophilic. As a result, the symmetric cell exhibited a long cycle stability of 850 h at the 80% depth discharge. He et al. reported fluoride-doped graphdiyne delivered the high reversible capacity of 320 mAh g^{-1} at a current density of 50 mA g^{-1}.[192] Large ion diffusion channels in F-GDY promoted K atom diffusion and storage on F substitution sites. Zhang, Sun, and co-workers synthesized the graphdiyne/graphene/graphdiyne sandwiched carbonaceous throughout a van der Waals strategy for high performance anodes.[193] The reversible capacity of a full cell could reach 151 mA g^{-1} at 200 mA g^{-1}.[195,196,97]

5.2. Zinc Ion Battery.

Rechargeable Zn-ion batteries have been hampered by poor capacity, rate performance, and dendrites, resulting from irreversibly discharged species. Designing materials and structures to improve the performance of rechargeable Zn-MnO_2 aqueous cells

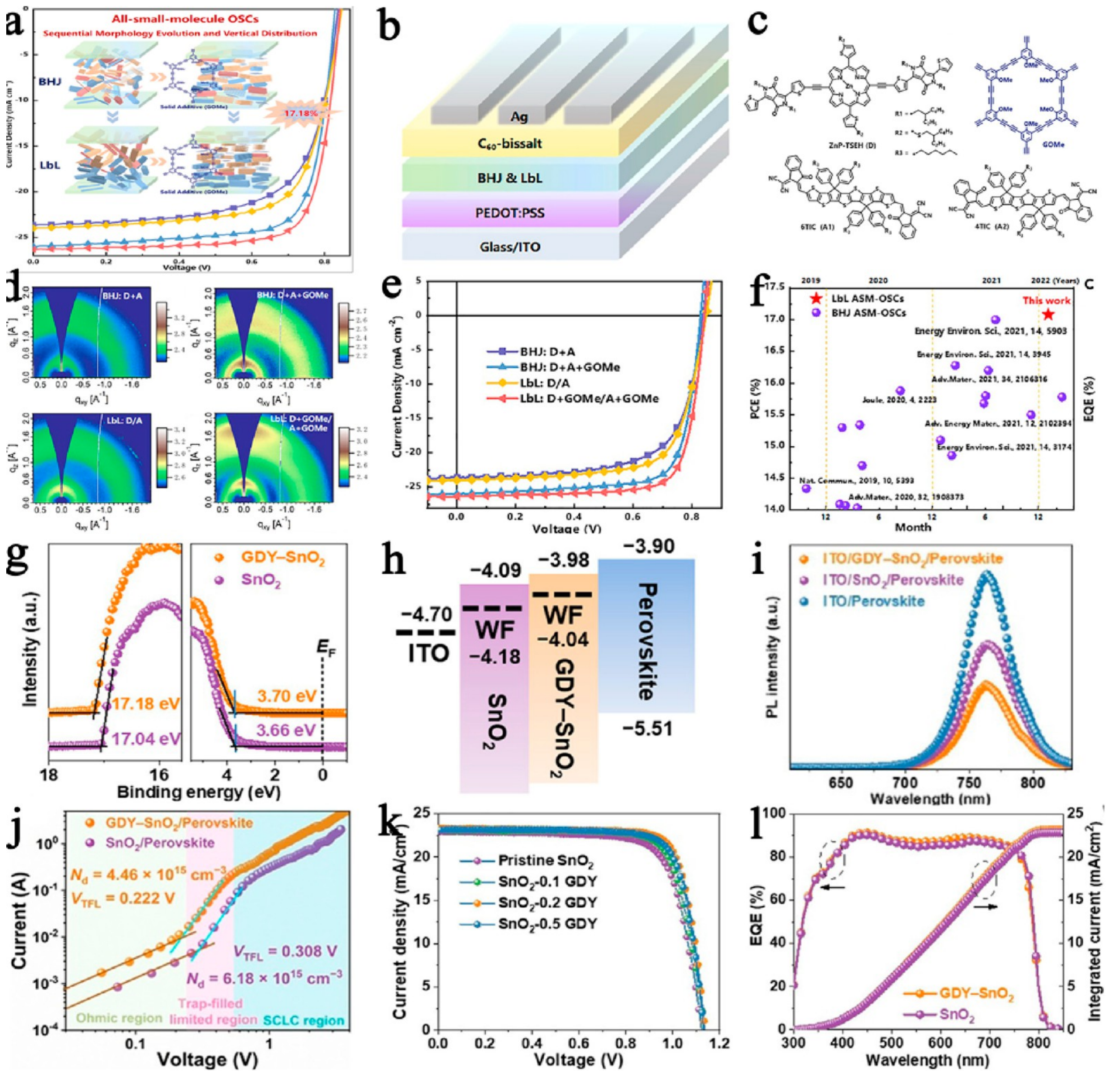

Figure 21. Solar cell. (a) Schema of all-small-molecule organic solar cells. (b) Schematic diagram of device structure. (c) Chemical structure of donor. (d) GIXD diffraction of samples. (e) *J*−*V* curves of samples. (f) Summary of the PCE for the reported ASM OSCs. Reproduced with permission from ref 199. Copyright 2022, Elsevier. (g) WF and valence band for SnO$_2$ and GDY-SnO$_2$ ETLs measured by UPS. (h) Energy band alignment for SnO$_2$ and GDY-SnO$_2$. (i) Time-resolved PL spectra. (j) Dark *J*−*V* curves of electron-only devices. (k) *J*−*V* curves of PSCs based on SnO$_2$. (l) EQE measurements of SnO$_2$ and GDY-SnO$_2$. Reproduced with permission from ref 200. Copyright 2020, Wiley-VCH.

has received extensive attention. Li et al. reported graphdiyne oxide membranes endowed Zn-MnO$_2$ cells with high capacity, high-rate performance capability, and long-term stability (Figure 20a).[194] The GDYO membrane ensured good ion transport and allowed us to maintain reversible stripping/plating of Zn ions, with the benefit of stablizing the electrodes. The specific capacity of the modified cell reached up to 300 mA h g^{-1} at a current density of 308 mA g^{-1} (Figure 20b−c). Fan, Zhi, and co-workers reported the hydrogen-substituted graphdiyne (HsGDY) materials could effectively inhibit zinc dendrites formation.[194] Simulation results revealed that the Zn^{2+} concentration field was redistributed by HsGDY, improving electrode demonstrated lifespans of >2400 h. Further, Yang et al. reported the N-modified graphdiyne could stabilize the interface pH by mediating hydrated zinc ion desolvation.[196] NGDY interface was synthesized on cellulose (CS) by triacetylenyl-based triazine monomer coupling (Figure 20d). The efficient desolvation ensures that electron directly transfers from the substrate to Zn^{2+} which avoided the formation of an alkaline zincate, resulting in high long-term stability (Figure 20e−g). Based on the in situ anchoring-nucleation growth of metal atoms on GDY, Luan et al. reported the evolution process of zinc-ion plating and deintercalating on the graphdiyne to explore the reasons for excellent stability (Figure 20h−i).[97] The growth of Zn single atom, nanoclusters, and nanoflats was induced by the uniformly dispersing and stably anchoring of graphdiyne. Further, N-doped graphdiyne was fabricated as the metal-free catalyst for Zn-air batteries by Huang and co-workers.[197] The pyridinic N active sites showed a higher catalytic performance than Pt/C or IrO$_2$. And the aqueous/solid state Zn-air batteries achieved a high open circuit voltage of 1.54 V.

5.3. Solar Cells and Fuel Cells. Li and co-workers reported chlorine-functionalized graphdiyne (GCl) applied as a multifunctional solid additive.[198] The addition of graphdiyne improved the efficiency and reproducibility of the device. The increase in mobility and the decrease in charge recombination synergistically could explain the increase in the levels of J_{sc} and FF after the introduction of GCl in the hybrid films. A record high efficiency of the control device was achieved at 17.3% compared to the certified efficiency of 17.1% obtaining an

https://doi.org/10.1021/acsnano.3c03849
ACS Nano 2023, 17, 14309−14346

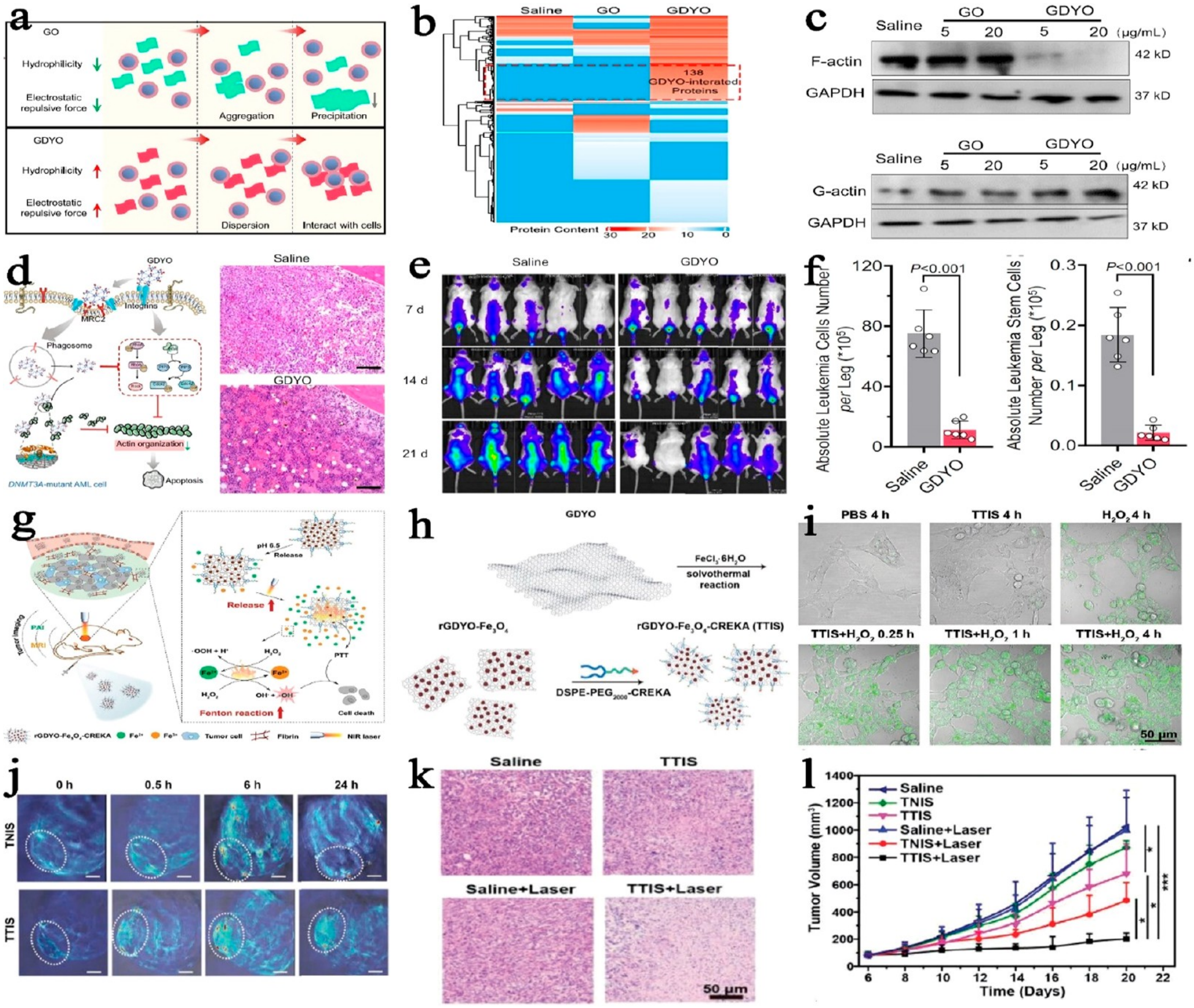

Figure 22. Cancer therapy. (a) Schematic diagram of dispersion kinetics of GO and GDYO in culture media. (b) Heatmap of GDYO-interacted proteins. (c) Western blot analysis of F-actin and G-actin after GO or GDYO treatment. (d) Schematic illustration for GDYO therapy against DNMT3A mutant AML cells. (e) Representative IVIS spectrum images. (f) Absolute leukemia cells and stem cells number. Reproduced with permission under a Creative Commons CC-BY License from ref 205. Copyright 2022, Springer Nature. (g) Schematic diagram of TTIS mediated tumor therapy. (h) Schematic diagram of the synthesis of TTIS. (i) Confocal microscopy images of cells treated. (j) Photoacoustic images at the tumor site. (k) H&E staining of tumor tissues post treatment. (l) Tumor growth curves under different treatments. Reproduced with permission from ref 208. Copyright 2020, Wiley-VCH.

increase in short-circuit current and fill factor, which demonstrated the state-of-the-art binary organic solar cell. Besides, the addition of nonvolatile property GCl reduced the batch-to-batch variability and facilitated large-scale production. Recently, Sun et al. fabricated an all-small molecule organic solar cell by methoxy-substituted graphdiyne to gain a 17.18% efficiency and 77.31% fill factor (Figure 21a−f).[199] Zhang et al. reported graphdiyne doped SnO_2 layer has 4-fold improved electron mobility and more facilitated band alignment (Figure 21g).[200] Electron extraction rate optimization and interfacial engineering were incorporated to maximize the match between SnO_2 and perovskite by optimizing electron extraction rates and interfacial engineering formed C−O bonds and more band alignment (Figure 21h). Enhanced hydrophobicity enhancement inhibited the nucleation of heterogeneous perovskites, which could contribute to the formation of high-quality films with reduced grain boundaries, lower defect density boundaries, and lower defect density (Figure 21i−l). Meng and co-workers reported a 20.54% power conversion efficiency by constructing the perovskite/graphdiyne bulk heterojunction.[201] And pyridinic nitrogen doped graphdiyne exhibited a excellent performance in hybrid perovskite reported by Zhang and co-workers.[202] At present, benchmarked proton exchange membrane-Nafion membranes have high proton conductivity and stability but are hampered by serious methanol permeability and utilization efficiency of methanol. GDY membranes possessed intrinsic potential to achieve superior proton conduction while efficiently suppressing methanol crossover. Wang et al. reported the NH_2-graphdiyne membrane could realize high selectivity between the proton and methanol.[203] The large area film with high integrity ensured the regular channel and uniform distribution of the aminated sites. The NH_2-GDY film efficiently inhibited 38% methanol crossover. And the cell assembled with NH_2-GDY exhibited higher power density and long-term stability. Recently, Li and co-workers fabricated an independent anode array of GDY@PtCu.[204] Anchored with $Pt_{4.4}Cu$ alloy nanoparticles, the graphdiyne nanochannel exhibited excellent catalyst performance in methanol oxide and the intrinsic selectivity of methanol permeation. Theoretical simulation demonstrated methanol diffusion and oxide in the ordered structure, resulting in maintaining initial 81% power density after 500 h long-term operation.

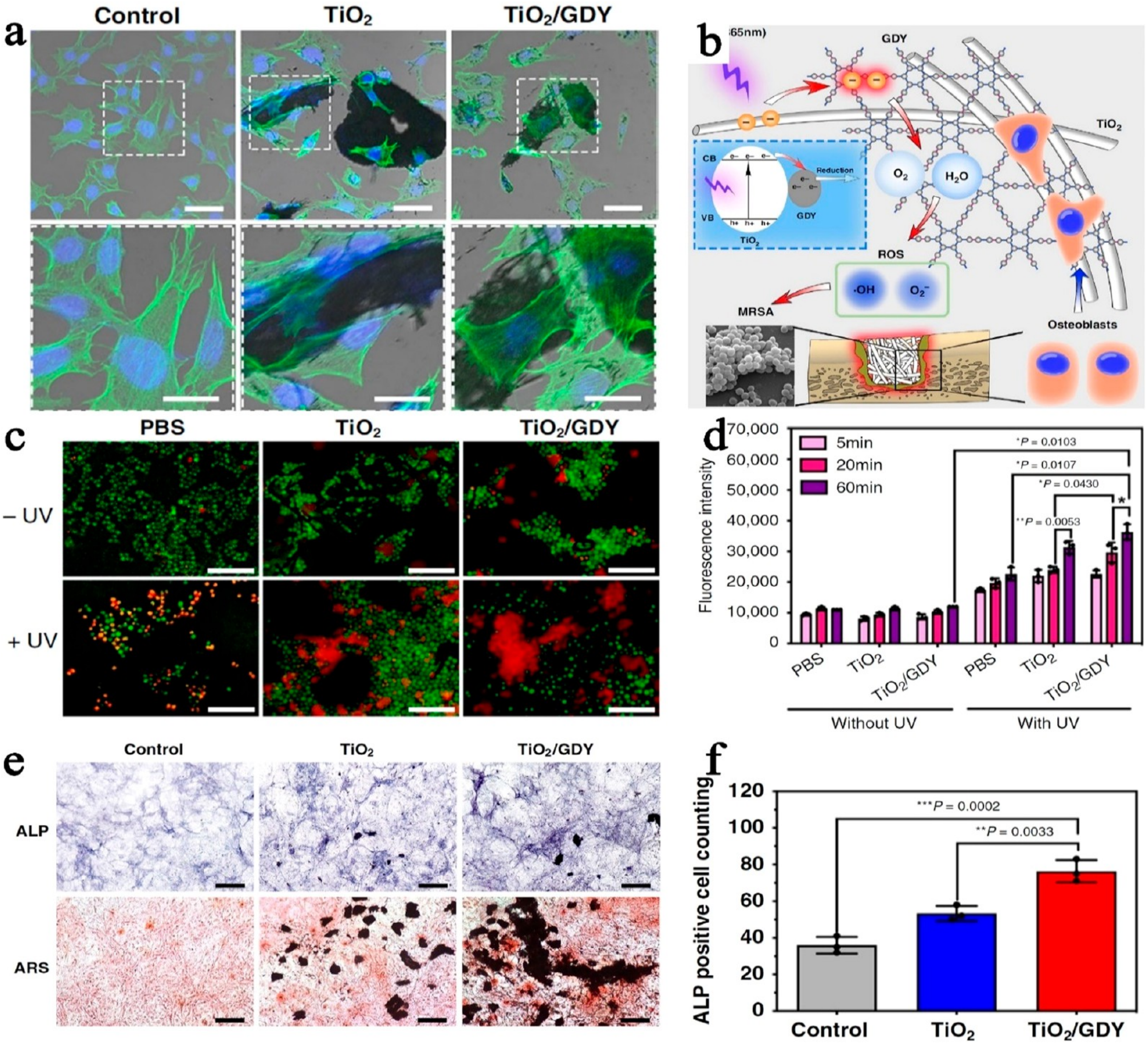

Figure 23. Antibacterial. (a) Schematic illustration of orthopedic implant infection. (b) Cytoskeleton staining of MC3T3-E1 cells after coculturing 24 h. (c) Live/dead stained images of MRSA biofilms with photocatalytic treatment. (d) Quantitative analysis of radical oxygen species in MRSA. (e) Alkaline phosphatase activity and Alizarin Red S staining on day 14. (f) Semiquantitative analysis of ALP activity. Reproduced with permission under a Creative Commons CC-BY License from ref 211. Copyright 2020, Springer Nature.

6. OTHER APPLICATIONS OF GRAPHDIYNE-BASED MATERIALS

6.1. Biochemical Application. GDY-based materials have demonstrated a wide range of applications in biomedicine and biosensing owing to outstanding conductivity, large surface area, high flexibility, natural band gap, and biocompatibility. The recent advances in GDY-based nanomaterials, along with their characteristics and useful applications in the biomedical field, will be discussed. Wang et al. reported that GDYO had an efficient antileukemic effect on the DNMT3A mutated AML with cell adhesion-related genes.[205] Experimental results demonstrated that highly hydrophilic GDYO could interact with integrin β2 (ITGB2) and c-type mannose receptor (MRC2) to increase cellular absorption (Figure 22a–b). Afterward, GDYO inhibited G-actin polymerization, damaged the actin cytoskeleton, and finally induced apoptosis of AML cells (Figure 22c–d). Mouse experiments illustrated survival of white blood cells while killing leukemic cells. which demonstrated the safety and therapeutic potential of GDYO (Figure 22e–f). Guo reported that the efficacy of cancer immunotherapy was enhanced via GDYO treatment.[206] After the injection of GDYO, the tumor growth in the melanoma-bearing model was slowed down. The research results revealed that GDYO nanosheets could re-educate the immunosuppressive cells by triggering the pro-inflammatory pathway and activating cytotoxic T cells. Qian and co-workers further demonstrated the antimacrophage effect of GDYO on lymphoma.[207] GDYO treatment significantly kills cancer stem cells, remodels the immunosuppressive tumor microenvironment simultaneously, and inhibits lymphoma growth ultimately. GDYO was also used by Min et al. to treat tumors photothermally through the Fenton reaction (Figure 22g).[208] The heat generated during PTT could accelerate the release of ions from tumor-targeted iron sponge (TTIS; Figure 22h) nanocomposite with simultaneous enhancement of the efficiency of the Fenton reaction, thus achieving combined PTT and Fenton Response-mediated cancer therapy (Figure 22i–l). Zhang et al. reported a metal-free BN-GDY ferroptosis-apoptosis inducer by efficient glutathione (GSH) depletion.[209] BN-GDY exhibited high catalytic activity for hydrogen peroxide decomposition, resulting in inhibiting colorectal cancer cell proliferation. Targeting the radiation source of cancer, Xie et al. synthesized the bovine serum albumin modified graphdiyne nanoparticles (GDY-BSA NPs) for a gastrointestinal radioprotector.[210] GDY-BSA NPs with a high free radical scavenging ability could consume the intracellular ROS generated by radiolysis and reduce mitochondrial membrane damage.

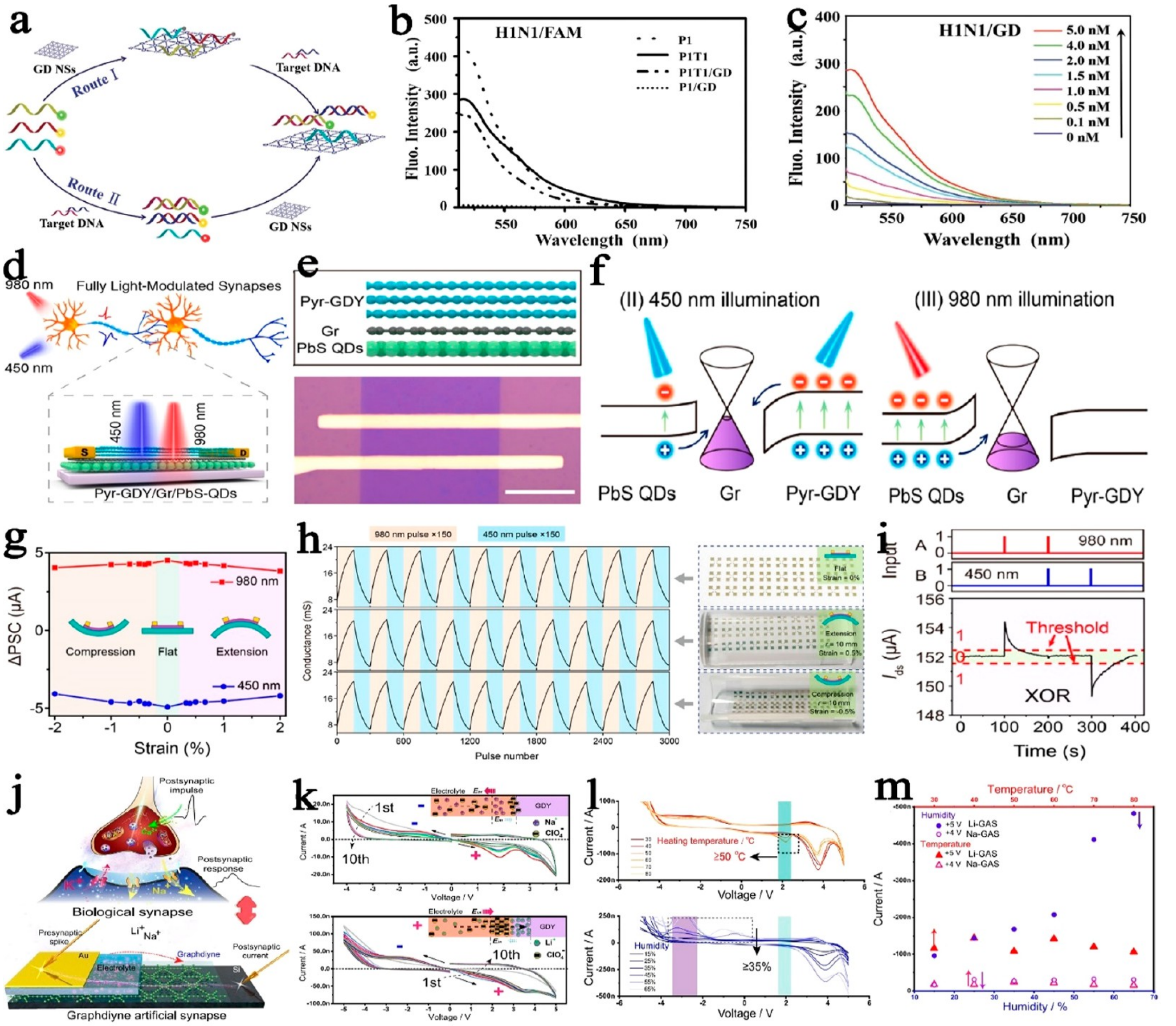

Figure 24. Biosensor. (a) Schematic diagram of GD-based multiplexed DNA detection. (b) Fluorescence spectra of H1N1/FAM ssDNA. (c) Fluorescence spectra of the dye-labeled ssDNA. Reproduced with permission from ref 213. Copyright 2017, Wiley-VCH. Schematic illustration of flexible optical synapses (d) and Pyr-GDY/Gr/PbS-QD heterostructure (e). (f) Energy band alignment for the Pyr-GDY/Gr/PbS heterostructure. (g) ΔPSC index fluctuation as a function of tensile strength. (h) Cyclic LTP/LTD curves of the device. (i) XOR logic function realized by using 980 and 450 nm optical pulses. Reproduced with permission from ref 215. Copyright 2021, American Chemical Society. (j) Schematic illustration of GASs. (k) *I*−*V* curves for Li-GAS and Na-GAS. (l) *I*−*V* curves of Li-GAS measured after heat and humidity treatment. (m) Current value of the devices after treatment in different environments. Reproduced with permission under a Creative Commons CC-BY License from ref 217. Copyright 2021, Springer Nature.

The GDY-modified TiO_2 nanofibers have been reported to prevent implant infection through photocatalyst generated radical oxygen species (Figure 23a).[211] Cells on TiO_2/GDY nanofibers tended to aggregate and adhere due to the superior biocompatibility of GDY (Figure 23b). More bacterial death occurred as a result of prolonged radical oxygen species (ROS) produced under UV irradiation as free electrons and holes transferred from TiO_2 to graphdiyne (Figure 23c−d). Besides, experimental results demonstrated that the bone tissue regeneration was promoted by TiO_2/GDY nanofiber (Figure 23e−f). ROS-dependent oxidation stress was also achieved by using GDYO as the antibacterial agent, which has superior antibacterial capability compared with graphdiyne.[212]

Few-layer GDY nanosheets were recently successfully used for DNA detection (Figure 24a),[213] showing distinguished fluorescence quenching ability and different affinities toward single-stranded DNA and double-stranded DNA (Figure 24b−c). Further, Hou et al. fabricated a biosensing platform based on graphdiyne to detect microRNA.[209,214] Zhang and co-workers reported the graphdiyne/graphene/PbS quantum dot heterostructure-based to emulate both the excitatory and inhibitory synaptic behaviors in an optical pathway (Figure 24d−e).[215] The simple device structure and low-dimensional features of this heterostructure confer powerful flexibility to the photosynapse in wearable electronic devices (Figure 24f). The optical synapse has a linear and symmetric conductivity update trajectory with multiple conductivity states and low noise, which facilitated accurate and efficient pattern recognition with high fault tolerance even in the bent state (Figure 24g). A range of logical functions and associative learning abilities have been demonstrated by the optical synapses in the optical pathway, enhancing the information processing ability of the neomorphs (Figure 24h−i). The information processing capability of neuromorphic computation has been significantly enhanced. In terms of human health, Li et al. fabricated a porous graphdiyne for respiration sensors.[216] Xu and co-workers reported a graphdiyne-based artificial synapse (GAS) with an excellent temperature and humidity response (Figure 24j−l). Ultralow voltage response and sub-biological power

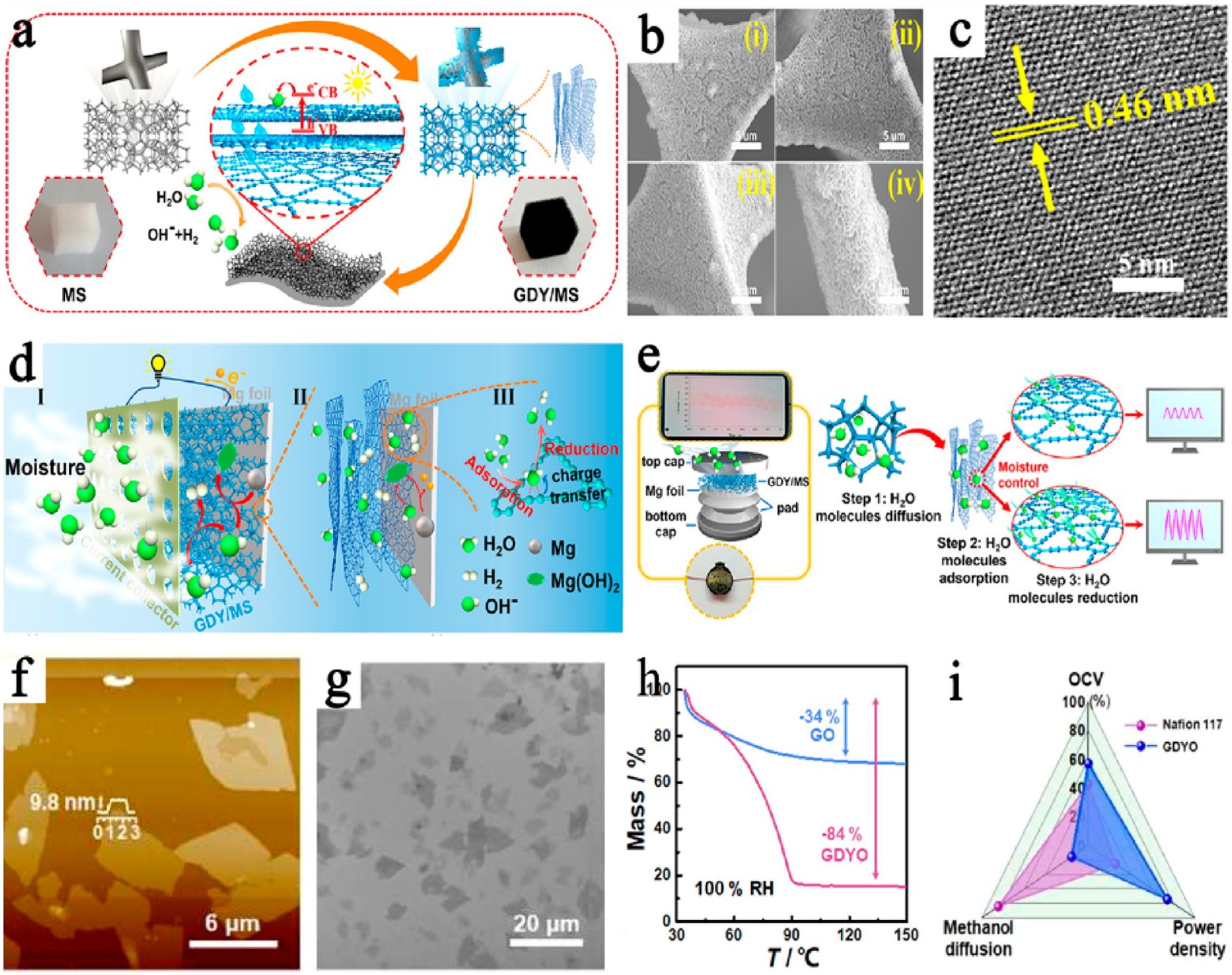

Figure 25. Intelligent device. (a) Schema of the preparation of GDY/MS. SEM (b) and TEM (c) images of GDY. (d) Schematic illustration of the process of GSMB. (e) Schema of humidity monitoring process by GSMB. Reproduced with permission from ref 218. Copyright 2023, American Chemical Society. AFM (f) and SEM (g) images of GDYO. (h) Thermogravimetric analysis of GDYO. (i) The comparison of GDYO and Nafion 117 in the performances of OCV. Reproduced with permission from ref 219. Copyright 2023, Wiley-VCH.

consumption meant GAS was competitive with other double-ended resistive switches (Figure 24m).[217]

6.2. Intelligent Devices. Carbon materials have been considered as promising materials that can be used in the development of next-generation multifunctional intelligent devices due to their advantages of suitable electrical conductivity, thermal stability, electrochemical stability, high specific surface area, and easy modification of chemical functional groups. Despite the above advantages and potentials of carbon materials, current reports on intelligent devices based on carbon materials are still very limited and challenging. By utilizing the numerous advantages of GDY, Fu et al. fabricated the solid magnesium cell by an array of graphdiyne nanosheets with both continuous humidity and a sunlight response (Figure 25a).[218] The integrated devices worked on the outstanding characteristics in capturing and transferring water molecules, catalyzing HER and utilizing solar energy of the graphdiyne cathode for high-performance intelligent SMB (Figure 25b−d). The devices could be applied as a self-powered humidity monitor with an ultrafast response time of <0.24 s, recovery time of <0.16 s, and high sensitivity (36,600%) (Figure 25e). Further, Mao et al. reported a graphdiyne oxide film with ultrahigh proton conductivity, which could be attributed to different proton conduction pathways (Figure 25f−g). And the GDYO membrane could be applied as the proton transfer membrane in methanol fuel cells with excellent performance (Figure 25h−i).[219] By spin-coating ultrathin GDY nanosheets onto flexible poly(ethylene terephthalate) (PET) substrates, GDY-based photodetectors (PDs) were obtained[221,220] and showed excellent photoresponsive behaviors with high photocurrent (P_{ph}, 5.98 μA cm^{-2}), photoresponsivity (R_{ph}, 1086.96 μA W^{1-}), detection rate (7.31 × 10^{10} Jones), and excellent long-term stability (more than 1 month). The high degree of flexibility of the GDY structure is responsible for the excellent performance that was maintained through 1000 times of bending and twisting. Li et al. developed a high-performance self-powered wind speed sensor possessing water/cold resistance, which can stably run for a long time and be directly applied in a typical extreme environment.[220]

As a two-dimensional semiconductor with excellent optical response properties, graphdiyne is an ideal material for optoelectronic devices.[222] Gao et al. developed strong ECL emission without any functionalization or treatment of GDY with potassium persulfate as the core agent (Figure 26a,b).[223] Mechanistic studies demonstrated that the ECL emission of GDY was generated by the transition of the surface state (Figure 26c−e). The ECL was produced in the NIR region at 705 nm with an ECL efficiency of 424% (Figure 26f−h). Zhang and coworkers[224] reported the GDY-based optoelectronic memory with floating gates on top of both ends with multibit storage capability. Benefiting from the excellent charge storage capability and high optical response of the GDY, the fabricated devices exhibited more than 256 different storage levels with a signal-to-tone ratio greater than 100. In addition, the fully two-dimensional material and the two-end structure gave the device robust bending. Wu et al. reported the Kerr nonlinearity of graphdiyne with a large nonlinear refractive index (10^{-5} cm^2 W^{-1}).[225] The excellent performance of nonlinear photonic devices

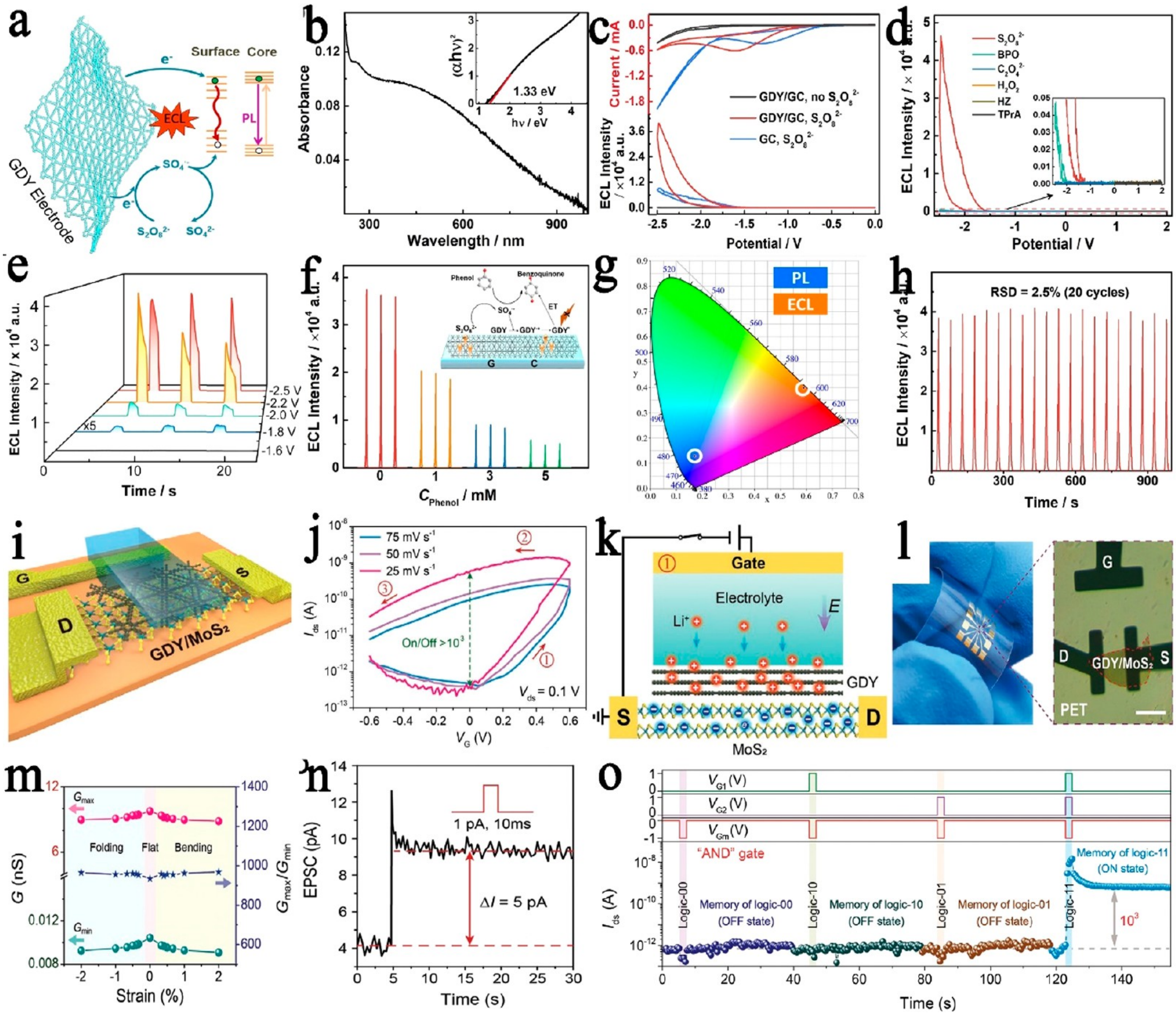

Figure 26. Smart detector. (a) Schematic illustration of GDY electrochemiluminescence. (b) Absorption spectrum of the GDY. (c) CV curves and the ECL-potential curves. (d) ECL-potential curves obtained at GDY/GC electrode. (e) ECL−time curves. (f) ECL intensity at different concentrations of phenol. (g) The CIE coordinates of GDY. (h) The ECL stability of the GDY. Reproduced with permission from ref 223. Copyright 2022, Wiley-VCH. (i) Schematic diagram of electrolyte-gated transistors. (j) Transfer curve of the EGT. (k) The intercalation processes of Li ions. (l) Photograph and optical-microscopy image of the EGT on PET substrate. (m) The function of tensile and compressive strain. (n) The EPSC responses triggered by positive and negative IGS pulses. (o) Output signals for the processing of logic transistor. Reproduced with permission from ref 226. Copyright 2021, Wiley-VCH.

(such as a Kerr switcher) fabricated by graphdiyne and SnS_2 was revealed by the SSPM method. Lu and co-workers presented the GDY/MoS_2-based EGT (Figure 26i).[226] With a lithium-ion storage graphdiyne layer, the GDY/MoS_2-based EGT exhibited a robust stability (<1% change over more than 2000 cycles), an ultralow energy consumption (50 J μm^{-2}), and long retention characteristics (>104 s) (Figure 26j−m). An ultrahigh G_{max}/G_{min} ratio (10^3), and an ultralow readout conductance (<10 nS) of the device has demonstrated this, thus enabling the implementation of neuromorphological calculations with near-ideal accuracy. In addition, the nonvolatile nature of GDY/MoS_2-based EGTs enables them to demonstrate logic functions in memory, which could perform logic processing in a single device and store logic processing (Figure 26n−o). These results demonstrated the potential of GDY/MoS_2-based EGTs for next-generation, low-power electronics beyond the von Neumann architecture. Qu et al. developed the high-performance n-type Ta_4SiTe_4/polyvinylidene fluoride/GDY thermoelectric composited.[227] The Ta_4SiTe_4/PVDF/GDY composite films demonstrated a maximum ZT value of 0.2 at 300 K, among the highest reported in organic−inorganic flexible thermoelectric composites.

6.3. Substance Absorption and Separation.

The basic structure and properties of GDY also endow it with many excellent advantages for the selective and high-performance adsorption and separation of substances. Geim and co-workers showed that the membranes made from multilayer GDY (Figure 27a−c) allowed fast, Knudsen-type permeation of light gases such as helium and hydrogen, whereas heavy noble gases like xenon exhibited strongly suppressed flows (Figure 27d−f).[228] These seemingly contradictory properties are explained by the high density of straight-through pores (direct porosity of 0.1%) in which heavy atoms were adsorbed on the pore walls (Figure 27g−h). And the gas investigative adsorption capacity of graphdiyne aerogel architecture was reported by Liu and co-workers.[229] Additionally, Zhang and co-workers fabricated the different hole sizes by a GDY-derivatized triptycene film to separate the acetylene and ethylene.[230] The separation of oils or organic solvents and water in an ultrafast and economical method was still gaining increasing attention with absorbent or membrane materials.[231] Zhang, Liu, and co-workers reported the graphdiyne-based 3D superhydrophobic porous architectures for the oil/water separation.[232] Besides, current experimental and theoretical calculations showed that graphdiyne could also realize

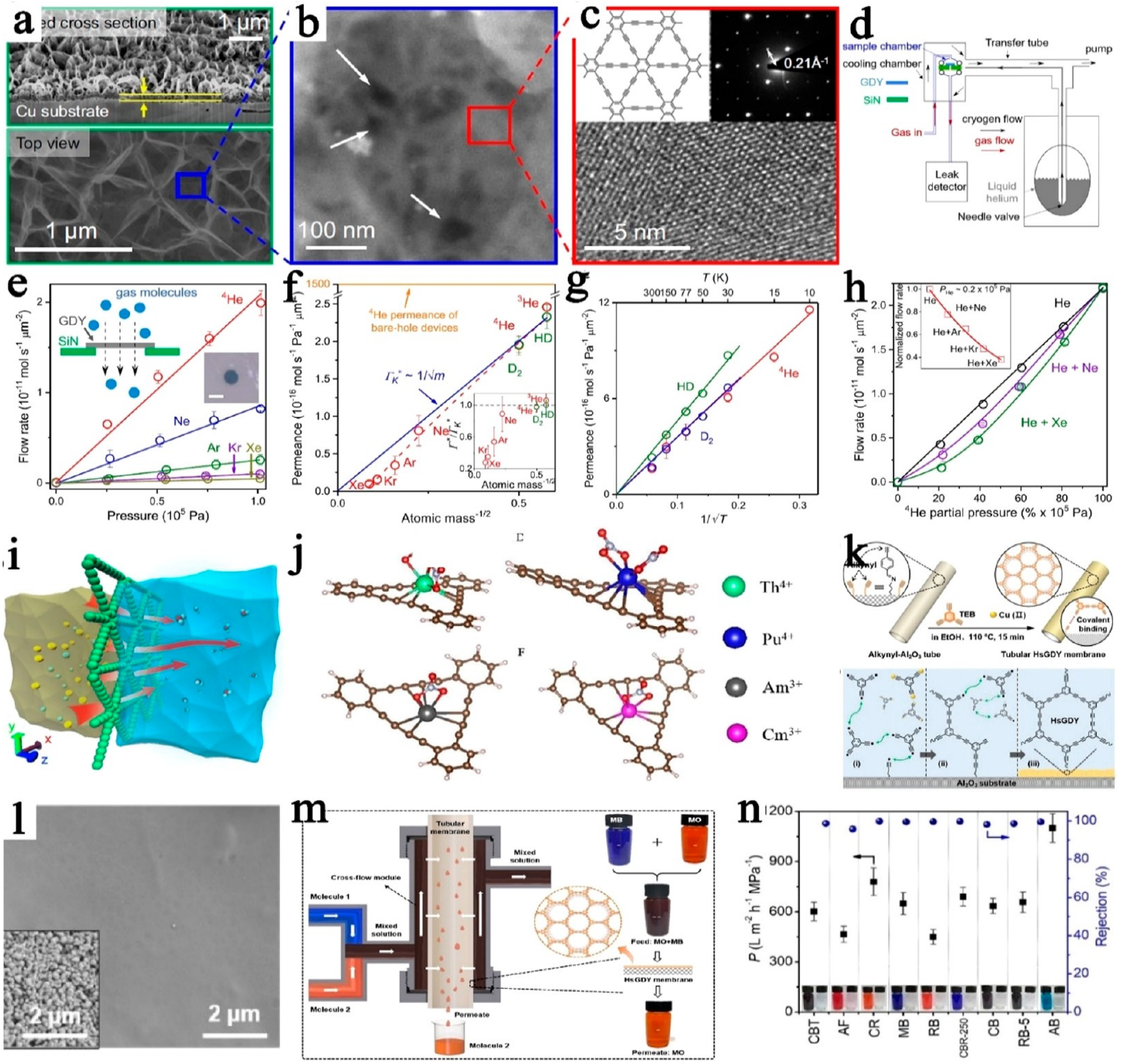

Figure 27. Substance separation. SEM (a), TEM (b), and HRTEM (c) images of graphdiyne-based membranes. (d) Schematic diagram of gas separation devices. (e) Flow rate of noble gases through micrometer-sized membranes. (f) Observed gas permeance at room temperature. (g) Temperature dependence of gas permeance for light gases. (h) ^{4}He permeation as a function of its partial pressure. Reproduced with permission under a Creative Commons CC-BY License from ref 228. Copyright 2022, Springer Nature. (i) Schematic representation of the graphdiyne separation system. Reproduced with permission from ref 234. Copyright 2013, IOP Publishing Ltd. (j) Various coordination patterns of actinide single ions on graphdiyne. Reproduced with permission from ref 235. Copyright 2020, Wiley-VCH. (k) Schematic diagram of the synthesis of HsGDY membranes on an Al_2O_3 tube. (l) SEM image of HsGDY membranes. (m) Scheme of the nanofiltration process. (n) Permeance and rejection rates of different conditions. Reproduced with permission from ref 236. Copyright 2023, Wiley-VCH.

ion separation and desalination (Figure 27i).[233,234] Shen and co-workers reported that actinide single ions could be coordinated with graphdiyne. Actinide ions on the graphdiyne had different coordination patterns and adsorption capacities, resulting in the separation of these ions commonly found in nuclear fuel (Figure 27j).[235] On the separation of small organic molecules in water, the superhydrophilic surface and hydrophobic pore membrane have been fabricated by Meng and co-workers (Figure 27k).[236] The HsGDY membrane with continuous stability could realize an excellent water permeance rate (near 1100 L m^{-2} h^{-1} MPa^{-1}; Figure 27l–n).

7. CONCLUSION AND PERSPECTIVES

The rapid development of carbon material science and technology has significantly influenced the progress of fundamental and applied sciences and the lifestyle of humans. As an emerging carbon allotrope, GDY possesses a sp and sp^2 cohybridized network in which the sp and sp^2- hybridized carbon atoms were topologically ordered in a planar one-atom-thick network. Such a one-of-a-kind chemical structure endowed GDY with extraordinary physical and chemical properties in fundamental and applied research and has brought renewed vitality to carbon material science. Graphdiyne science has currently been a developing interdisciplinary science in many important fields and has provided tremendous opportunities not only for revealing the intrinsic properties of graphdiyne but also for achieving transformative results in many research fields. In this review, we discussed in a comprehensive and detailed manner the research progress in the synthesis, properties, and applications of GDY and GDY-based materials. Due to its special chemical and electrical structures (unevenly distributed surface charge, intrinsic pores, highly conjugated two-dimensional planar structures, reversible chemical bonding transitions, fast charge transfer, excellent mechanical properties, etc.), GDY has already demonstrated potential uses in a wide range of crucial disciplines, including chemistry, physics, materials science, biological engineering, and environmental engineering, despite its brief growth history. In addition, in this review, we detail the controlled synthesis and self-assembly of GDY-based materials with adjustable structures and properties, providing scientists with valuable guidance on chemical synthesis, which may help solve some scientific bottlenecks.

At present, GDY has brought a series of achievements in the fields of catalysis, energy, optoelectronics, life science, information intelligence, and material transformation and conversion. For example, the creation of zerovalent metal atom catalysts is a breakthrough in the field of electrocatalysis to realize the maximum utilization of catalytic atoms. Besides, aiming at the challenge of how to achieve efficient ammonia synthesis under room temperatures and ambient pressures, we started from concept innovation, broke the problem faced by traditional catalysts, and successfully prepared a synthetic ammonia catalyst with transformative catalytic performance under room temperature and ambient pressures. In addition, based on the special properties of GDY, we put forward the concept of "alkyne-alkene transition", especially in the aspect of lithium fast charge, to change the traditional mechanism of lithium fast charge, and establish a special mode of lithium fast charge. Owing to its electronic and chemical structures, GDY also demonstrates some transformative application potential in the fields of hydrogen energy conversion, photosynthetic chemicals, efficient artificial nitrogen fixation, life sciences, intelligent information, and so on.

Although many advances have been made in the synthesis and application of GDY, the research and efficient utilization of GDY are still in the development stage and far from our needs. In the next ten years, researchers still need to overcome some fundamental issues and accumulate more knowledge such as (i) improvement of synthesis methods to effectively control the continuous growth of large-area all-crystalline graphdiyne with different layers (e.g., monolayer and few layer) and basic physical property measurements of monolayer GDY to explore the structure−property relationship and the intrinsic electronic structure of GDY; (ii) to better control the band structure of GDY and study the influence regularity on properties, explore the origin and conversion of the intrinsic optical, electrical, and magnetic energy of GDY-based materials; and (iii) exploration of efficient utilization devices and frontier knowledge, functions, and applications of GDY in the fields of semiconductors, catalysis, energy, optoelectronics, information intelligence, bioscience, etc. As a transformative material, GDY will rapidly develop in the direction of interdisciplinary research and play a more important role in cross-disciplinary research.

AUTHOR INFORMATION

Corresponding Authors

Yurui Xue − *CAS Key Laboratory of Organic Solids, Institute of Chemistry, Chinese Academy of Sciences, Beijing 100190, P. R. China; Shandong Provincial Key Laboratory for Science of Material Creation and Energy Conversion, Science Center for Material Creation and Energy Conversion, Institute of Frontier and Interdisciplinary, Shandong University, Qingdao 266237, P. R. China*; Email: yrxue@sdu.edu.cn

Changshui Huang − *CAS Key Laboratory of Organic Solids, Institute of Chemistry, Chinese Academy of Sciences, Beijing 100190, P. R. China;* orcid.org/0000-0001-5169-0855; Email: huangcs@iccas.ac.cn

Chunying Chen − *CAS Key Laboratory for Biomedical Effects of Nanomaterials and Nanosafety and CAS Center for Excellence in Nanoscience, National Center for Nanoscience and Technology of China, Beijing 100190, P. R. China;* orcid.org/0000-0002-6027-0315; Email: chenchy@nanoctr.cn

Yanbing Guo − *Key Laboratory of Pesticide & Chemical Biology of Ministry of Education, Institute of Environmental and Applied Chemistry, College of Chemistry, Central China Normal University, Wuhan 430079, P. R. China;* orcid.org/0000-0002-5399-1739; Email: guoyanbing@mail.ccnu.edu.cn

Tong-Bu Lu − *MOE International Joint Laboratory of Materials Microstructure, Institute for New Energy Materials and Low Carbon Technologies, School of Materials Science and Engineering, Tianjin University of Technology, Tianjin 300350, P. R. China;* orcid.org/0000-0002-6087-4880; Email: lutongbu@tjut.edu.cn

Dan Wang − *Institute of Process Engineering, Chinese Academy of Sciences, Beijing 100190, P. R. China*; Email: danwang@ipe.ac.cn

Lanqun Mao − *College of Chemistry, Beijing Normal University, Beijing 100875, P. R. China;* orcid.org/0000-0001-8286-9321; Email: lqmao@bnu.edu.cn

Jin Zhang − *Center for Nanochemistry, Beijing Science and Engineering Center for Nanocarbons, Beijing National Laboratory for Molecular Sciences, College of Chemistry and Molecular Engineering, Peking University, Beijing 100871, P. R. China;* orcid.org/0000-0003-3731-8859; Email: jinzhang@pku.edu.cn

Yue Zhang − *Academy for Advanced Interdisciplinary Science and Technology, Beijing Advanced Innovation Center for Materials Genome Engineering and Beijing Key Laboratory for Advanced Energy Materials and Technologies, School of Materials Science and Engineering, University of Science and Technology Beijing, Beijing 100083, P. R. China;* orcid.org/0000-0002-8213-1420; Email: yuezhang@ustb.edu.cn

Lifeng Chi − *Institute of Functional Nano and Soft Materials, Soochow University, Soochow 1215031, P. R. China;* orcid.org/0000-0003-3835-2776; Email: chilf@suda.edu.cn

Wanlin Guo − *Key Laboratory for Intelligent Nano Materials and Devices of the Ministry of Education, State Key Laboratory of Mechanics and Control for Aerospace Structures, and Institute for Frontier Science, Nanjing University of Aeronautics and Astronautics, Nanjing 210016, P. R. China;* orcid.org/0000-0002-2302-8044; Email: wlguo@nuaa.edu.cn

Xian-He Bu − *School of Materials Science and Engineering, National Institute for Advanced Materials, Nankai University, Tianjin 300350, P. R. China;* orcid.org/0000-0002-2646-7974; Email: buxh@nankai.edu.cn

Hongjie Zhang − *Department of Chemistry, Tsinghua University, Beijing 100084, P. R. China;* Email: hjzhang2019@

Liming Dai − *Australian Carbon Materials Centre (A-CMC), School of Chemical Engineering, University of New South Wales, Sydney, New South Wales 2052, Australia;* orcid.org/0000-0001-7536-160X; Email: l.dai@unsw.edu.au

Yuliang Zhao − *CAS Key Laboratory for Biomedical Effects of Nanomaterials and Nanosafety and CAS Center for Excellence in Nanoscience, National Center for Nanoscience and Technology of China, Beijing 100190, P. R. China; School of Chemical Sciences, University of Chinese Academy of Sciences, Beijing 100049, P. R. China;* orcid.org/0000-0002-9586-9360; Email: zhaoyl@nanoctr.cn

Yuliang Li − *CAS Key Laboratory of Organic Solids, Institute of Chemistry, Chinese Academy of Sciences, Beijing 100190, P. R. China; Shandong Provincial Key Laboratory for Science of Material Creation and Energy Conversion, Science Center for Material Creation and Energy Conversion, Institute of Frontier and Interdisciplinary, Shandong University, Qingdao 266237, P. R. China; School of Chemical Sciences, University of Chinese Academy of Sciences, Beijing 100049, P. R. China;* orcid.org/0000-0001-5279-0399; Email: ylli@iccas.ac.cn

Authors

Xuchen Zheng − *CAS Key Laboratory of Organic Solids, Institute of Chemistry, Chinese Academy of Sciences, Beijing 100190, P. R. China; School of Chemical Sciences, University of Chinese Academy of Sciences, Beijing 100049, P. R. China*

Siao Chen − *CAS Key Laboratory of Organic Solids, Institute of Chemistry, Chinese Academy of Sciences, Beijing 100190, P. R. China; School of Chemical Sciences, University of Chinese Academy of Sciences, Beijing 100049, P. R. China*

Jinze Li − *CAS Key Laboratory of Organic Solids, Institute of Chemistry, Chinese Academy of Sciences, Beijing 100190, P. R. China; School of Chemical Sciences, University of Chinese Academy of Sciences, Beijing 100049, P. R. China*

Han Wu − *CAS Key Laboratory of Organic Solids, Institute of Chemistry, Chinese Academy of Sciences, Beijing 100190, P. R. China; School of Chemical Sciences, University of Chinese Academy of Sciences, Beijing 100049, P. R. China*

Chao Zhang − *CAS Key Laboratory of Organic Solids, Institute of Chemistry, Chinese Academy of Sciences, Beijing 100190, P. R. China; School of Chemical Sciences, University of Chinese Academy of Sciences, Beijing 100049, P. R. China*

Danyan Zhang − *CAS Key Laboratory of Organic Solids, Institute of Chemistry, Chinese Academy of Sciences, Beijing 100190, P. R. China; School of Chemical Sciences, University of Chinese Academy of Sciences, Beijing 100049, P. R. China*

Xi Chen − *CAS Key Laboratory of Organic Solids, Institute of Chemistry, Chinese Academy of Sciences, Beijing 100190, P. R. China; School of Chemical Sciences, University of Chinese Academy of Sciences, Beijing 100049, P. R. China*

Yang Gao − *CAS Key Laboratory of Organic Solids, Institute of Chemistry, Chinese Academy of Sciences, Beijing 100190, P. R. China*

Feng He − *CAS Key Laboratory of Organic Solids, Institute of Chemistry, Chinese Academy of Sciences, Beijing 100190, P. R. China;* orcid.org/0000-0003-4820-7978

Lan Hui − *CAS Key Laboratory of Organic Solids, Institute of Chemistry, Chinese Academy of Sciences, Beijing 100190, P. R. China*

Huibiao Liu − *CAS Key Laboratory of Organic Solids, Institute of Chemistry, Chinese Academy of Sciences, Beijing 100190, P. R. China; School of Chemical Sciences, University of Chinese Academy of Sciences, Beijing 100049, P. R. China;* orcid.org/0000-0002-9017-6872

Tonggang Jiu − *Shandong Provincial Key Laboratory for Science of Material Creation and Energy Conversion, Science Center for Material Creation and Energy Conversion, Institute of Frontier and Interdisciplinary, Shandong University, Qingdao 266237, P. R. China;* orcid.org/0000-0001-9608-4429

Ning Wang − *Shandong Provincial Key Laboratory for Science of Material Creation and Energy Conversion, Science Center for Material Creation and Energy Conversion, Institute of Frontier and Interdisciplinary, Shandong University, Qingdao 266237, P. R. China*

Guoxing Li − *Shandong Provincial Key Laboratory for Science of Material Creation and Energy Conversion, Science Center for Material Creation and Energy Conversion, Institute of Frontier and Interdisciplinary, Shandong University, Qingdao 266237, P. R. China;* orcid.org/0000-0002-4384-7063

Jialiang Xu − *School of Materials Science and Engineering, National Institute for Advanced Materials, Nankai University, Tianjin 300350, P. R. China;* orcid.org/0000-0003-2441-4809

Complete contact information is available at:
https://pubs.acs.org/10.1021/acsnano.3c03849

Notes

The authors declare no competing financial interest.

ACKNOWLEDGMENTS

We thank the support from the Fundamental Research Center of Nano Toxicology Chemistry, supported through the National Natural Science Foundation of China, the National Key Research and Development Project of China (2022YFA1204500, 2022YFA1204501, 2022YFA1204503, 2018YFA0703501) and the Key Program of the Chinese Academy of Sciences (XDPB13).

VOCABULARY

Graphdiyne	a emerging member of carbon allotrope with characteristics of one-atom-thick two-dimensional layers comprising of sp and sp^2 hybridized carbon atoms
two-dimensional materials	sheet-like nanomaterials with a thickness on the atomic scale, in which the electron is free to move in the two-dimensional plane
sp-hybridization	an orbital hybridization of one s orbital and one p orbital hybridize, resulting in two sp orbitals with equal energy and two remaining p orbitals
atom catalyst	the catalysts obtained by anchoring zerovalent metal atoms on graphdiyne
energy conversion	the process of changing one form of energy into another

REFERENCES

(1) Li, G.; Li, Y.; Liu, H.; Guo, Y.; Li, Y.; Zhu, D. Architecture of graphdiyne nanoscale films. *Chem. Commun.* **2010**, *46*, 3256−3258.

(2) Gao, X.; Liu, H.; Wang, D.; Zhang, J. Graphdiyne: synthesis, properties, and applications. *Chem. Soc. Rev.* **2019**, *48*, 908−936.

(3) Fang, Y.; Liu, Y.; Qi, L.; Xue, Y.; Li, Y. 2D Graphdiyne: an emerging carbon material. *Chem. Soc. Rev.* **2022**, *51*, 2681−2709.

(4) Yu, H.; Xue, Y.; Li, Y. Graphdiyne and its assembly architectures synthesis functionalization and applications. *Adv. Mater.* **2019**, *31*, 1803101.

(5) Kong, Y.; Li, J.; Zeng, S.; Yin, C.; Tong, L.; Zhang, J. Bridging the gap between reality and ideality of graphdiyne: the advances of synthetic methodology. *Chem.* **2020**, *6*, 1933−1951.

(6) Li, J.; Gao, X.; Zhu, L.; Ghazzal, M. N.; Zhang, J.; Tung, C. H.; Wu, L. Z. Graphdiyne for crucial gas involved catalytic reactions in energy conversion applications. *Energy Environ. Sci.* **2020**, *13*, 1326−1346.

(7) Huang, C.; Li, Y.; Wang, N.; Xue, Y.; Zuo, Z.; Liu, H.; Li, Y. Progress in research into 2d graphdiyne-based materials. *Chem. Rev.* **2018**, *118*, 7744−7803.

(8) Sheka, E. Chapter Four - Stretching and Breaking of Chemical Bonds, Correlation of Electrons, and Radical Properties of Covalent Species. In *Adv. Quantum Chem.*; Sabin, J. R., Brändas, E. J, Eds.; Academic Press, 2015; Vol. *70*, pp 111−161.

(9) Li, H.; Lim, J. H.; Lv, Y.; Li, N.; Kang, B.; Lee, J. Y. Graphynes and graphdiynes for energy storage and catalytic utilization: theoretical insights into recent advances. *Chem. Rev.* **2023**, *123*, 4795−4854.

(10) Li, Y.; Xu, L.; Liu, H.; Li, Y. Graphdiyne and graphyne: from theoretical predictions to practical construction. *Chem. Soc. Rev.* **2014**, *43*, 2572−2586.

(11) Long, M.; Tang, L.; Wang, D.; Li, Y.; Shuai, Z. Electronic structure and carrier mobility in graphdiyne sheet and nanoribbons: theoretical predictions. *ACS Nano* **2011**, *5*, 2593−2600.

(12) Zuo, Z.; Shang, H.; Chen, Y.; Li, J.; Liu, H.; Li, Y.; Li, Y. A facile approach for graphdiyne preparation under atmosphere for an advanced battery anode. *Chem. Commun.* **2017**, *53*, 8074−8077.

(13) Jia, Z.; Li, Y.; Zuo, Z.; Liu, H.; Huang, C.; Li, Y. Synthesis and properties of 2D carbon - graphdiyne. *Acc. Chem. Res.* **2017**, *50*, 2470−2478.

(14) Zheng, Z.; Xue, Y.; Li, Y. A new carbon allotrope: graphdiyne. *Trend. Chem.* **2022**, *4*, 754−768.

(15) Li, J.; Zhu, L.; Tung, C.-H.; Wu, L.-Z. Engineering graphdiyne for solar photocatalysis. *Angew. Chem., Int. Ed.* **2023**, *135*, No. e202301384.

(16) Fu, X.; Zhao, X.; Lu, T. B.; Yuan, M.; Wang, M. Graphdiyne-based single-atom catalysts with different coordination environments. *Angew. Chem., Int. Ed.* **2023**, *135*, No. e202219242.

(17) Zuo, Z.; Wang, D.; Zhang, J.; Lu, F.; Li, Y. Synthesis and applications of graphdiyne-based metal-free catalysts. *Adv. Mater.* **2019**, *31*, 1803762.

(18) Khan, K.; Tareen, A. K.; Iqbal, M.; Shi, Z.; Zhang, H.; Guo, Z. Novel emerging graphdiyne based two dimensional materials: synthesis, properties and renewable energy applications. *Nano Today* **2021**, *39*, 101207.

(19) Li, B.; Lai, C.; Zhang, M.; Zeng, G.; Liu, S.; Huang, D.; Qin, L.; Liu, X.; Yi, H.; Xu, F.; An, N.; Chen, L. Graphdiyne: A rising star of electrocatalyst support for energy conversion. *Adv. Energy Mater.* **2020**, *10*, 2000177.

(20) Li, J.; Wang, C.; Zhang, B.; Wang, Z.; Yu, W.; Chen, Y.; Liu, X.; Guo, Z.; Zhang, H. Artificial Carbon Graphdiyne: Status and challenges in nonlinear photonic and optoelectronic applications. *ACS Appl. Mater. Interfaces* **2020**, *12*, 49281−49296.

(21) Chen, S.; Shi, G. Two-dimensional materials for halide perovskite-based optoelectronic devices. *Adv. Mater.* **2017**, *29*, 1605448.

(22) Kang, J.; Huang, S.; Jiang, K.; Lu, C.; Chen, Z.; Zhu, J.; Yang, C.; Ciesielski, A.; Qiu, F.; Zhuang, X. 2D Porous polymers with sp^2-carbon connections and sole sp^2-carbon skeletons. *Adv. Funct. Mater.* **2020**, *30*, 2000857.

(23) Liu, J.; Chen, C.; Zhao, Y. Progress and prospects of graphdiyne-based materials in biomedical applications. *Adv. Mater.* **2019**, *31*, 1804386.

(24) He, F.; Li, Y. Advances on theory and experiments of the energy applications in graphdiyne. *CCS Chem.* **2023**, *5*, 72−94.

(25) Xue, Y.; Li, Y.; Zhang, J.; Liu, Z.; Zhao, Y. 2D graphdiyne materials: challenges and opportunities in energy field. *Sci. China Chem.* **2018**, *61*, 765−786.

(26) Liu, B.; Xu, L.; Zhao, Y.; Du, J.; Yang, N.; Wang, D. Heteroatoms in graphdiyne for catalytic and energy-related applications. *J. Mater. Chem. A* **2021**, *9*, 19298−19316.

(27) Xue, Y.; Huang, B.; Yi, Y.; Guo, Y.; Zuo, Z.; Li, Y.; Jia, Z.; Liu, H.; Li, Y. Anchoring zero valence single atoms of nickel and iron on graphdiyne for hydrogen evolution. *Nat. Commun.* **2018**, *9*, 1460.

(28) Yu, H.; Xue, Y.; Hui, L.; Zhang, C.; Li, Y.; Zuo, Z.; Zhao, Y.; Li, Z.; Li, Y. Efficient hydrogen production on a 3D flexible heterojunction material. *Adv. Mater.* **2018**, *30*, 1707082.

(29) Yu, H.; Xue, Y.; Hui, L.; Zhang, C.; Zhao, Y.; Li, Z.; Li, Y. Controlled growth of mos$_2$ nanosheets on 2D N-doped graphdiyne nanolayers for highly associated effects on water reduction. *Adv. Funct. Mater.* **2018**, *28*, 1707564.

(30) Wang, N.; He, J.; Tu, Z.; Yang, Z.; Zhao, F.; Li, X.; Huang, C.; Wang, K.; Jiu, T.; Yi, Y.; Li, Y. Synthesis of chlorine-substituted graphdiyne and applications for lithium-ion storage. *Angew. Chem., Int. Ed.* **2017**, *129*, 10880−10885.

(31) Wang, F.; Zuo, Z.; Li, L.; He, F.; Lu, F.; Li, Y. A universal strategy for constructing seamless graphdiyne on metal oxides to stabilize the electrochemical structure and interface. *Adv. Mater.* **2018**, *31*, 1806272.

(32) Wang, F.; Zuo, Z.; Li, L.; Li, K.; He, F.; Jiang, Z.; Li, Y. Large-area aminated-graphdiyne thin films for direct methanol fuel cells. *Angew. Chem., Int. Ed.* **2019**, *58*, 15010−15015.

(33) Matsuoka, R.; Sakamoto, R.; Hoshiko, K.; Sasaki, S.; Masunaga, H.; Nagashio, K.; Nishihara, H. Crystalline graphdiyne nanosheets produced at a gas/liquid or liquid/liquid interface. *J. Am. Chem. Soc.* **2017**, *139*, 3145−3152.

(34) Gao, X.; Zhu, Y.; Yi, D.; Zhou, J.; Zhang, S.; Yin, C.; Ding, F.; Zhang, S.; Yi, X.; Wang, J.; Tong, L.; Han, Y.; Liu, Z.; Zhang, J. Ultrathin graphdiyne film on graphene through solution-phase van der waals epitaxy. *Sci. Adv.* **2018**, *4*, No. eaat6378.

(35) Li, Y.; Chen, C.; Wang, D.; Xue, Y. 2D carbon graphdiyne development and progress on fundamental science. *Nano Today* **2023**, *48*, 101725.

(36) Long, M.; Tang, L.; Wang, D.; Li, Y.; Shuai, Z. Electronic structure and carrier mobility in graphdiyne sheet and nanoribbons: theoretical predictions. *ACS Nano* **2011**, *5*, 2593−2600.

(37) Jiao, Y.; Du, A.; Hankel, M.; Zhu, Z.; Rudolph, V.; Smith, S. C. Graphdiyne: a versatile nanomaterial for electronics and hydrogen purification. *Chem. Commun.* **2011**, *47*, 11843−11845.

(38) Cui, H. J.; Sheng, X. L.; Yan, Q. B.; Zheng, Q. R.; Su, G. Strain-induced dirac cone-like electronic structures and semiconductor-semimetal transition in graphdiyne. *Phys. Chem. Chem. Phys.* **2013**, *15*, 8179−8185.

(39) Luo, G.; Zheng, Q.; Mei, W. N.; Lu, J.; Nagase, S. Structural, electronic, and optical properties of bulk graphdiyne. *J. Mater. Chem. C* **2013**, *117*, 13072−13079.

(40) Zheng, Q.; Luo, G.; Liu, Q.; Quhe, R.; Zheng, J.; Tang, K.; Gao, Z.; Nagase, S.; Lu, J. Structural and electronic properties of bilayer and trilayer graphdiyne. *Nanoscale* **2012**, *4*, 3990−3996.

(41) Luo, G.; Qian, X.; Liu, H.; Qin, R.; Zhou, J.; Li, L.; Gao, Z.; Wang, E.; Mei, W. N.; Lu, J.; Li, Y.; Nagase, S. Quasiparticle energies and excitonic effects of the two-dimensional carbon allotrope graphdiyne: theory and experiment. *Phys. Rev. B* **2011**, *84*, 075439.

(42) Lin, L.; Pan, H.; Chen, Y.; Song, X.; Xu, J.; Liu, H.; Tang, S.; Du, Y.; Tang, N. Identifying the stacking style, intrinsic bandgap and magnetism of pristine graphdiyne. *Carbon* **2019**, *143*, 8−13.

(43) Xie, C.; Hu, X.; Guan, Z.; Li, X.; Zhao, F.; Song, Y.; Li, Y.; Li, X.; Wang, N.; Huang, C. Tuning the Properties of Graphdiyne by Introducing Electron-Withdrawing/Donating Groups. *Angew. Chem., Int. Ed.* **2020**, *59*, 13542−13546.

(44) Zhang, C.; Xue, Y.; Zheng, X.; Qi, L.; Li, Y. Loaded Cu-Er Metal Iso-Atoms on Graphdiyne for Artificial Photosynthesis. *Mater. Today* **2023**, *66*, 72.

(45) Li, C.; Lu, X.; Han, Y.; Tang, S.; Ding, Y.; Liu, R.; Bao, H.; Li, Y.; Luo, J.; Lu, T. Direct imaging and determination of the crystal structure of six-layered graphdiyne. *Nano Res.* **2018**, *11*, 1714−1721.

(46) Yin, C.; Li, J.; Li, T.; Yu, Y.; Kong, Y.; Gao, P.; Peng, H.; Tong, L.; Zhang, J. Catalyst-free synthesis of few-layer graphdiyne using a microwave-induced temperature gradient at a solid/liquid interface. *Adv. Funct. Mater.* **2020**, *30*, 2001396.

(47) Yan, H.; Yu, P.; Han, G.; Zhang, Q.; Gu, L.; Yi, Y.; Liu, H.; Li, Y.; Mao, L. High-yield and damage-free exfoliation of layered graphdiyne in aqueous phase. *Angew. Chem., Int. Ed.* **2019**, *58*, 746−750.

(48) Hu, G.; He, J.; Li, Y. Controllable synthesis of two-dimensional graphdiyne films catalyzed by a copper(ii) trichloro complex. *ACS Catal.* **2022**, *12*, 6712−6721.

(49) Kan, X.; Wang, D.; Pan, Q.; Wang, Y.; Xiao, Y.; Liu, J.; Zhao, Y.; Li, Z. Confined interfacial synthesis of highly crystalline and ultrathin graphdiyne films and their applications for N_2 fixation. *Chem.—Eur. J.* **2020**, *26*, 7801−7807.

(50) Zhou, J.; Xie, Z.; Liu, R.; Gao, X.; Li, J.; Xiong, Y.; Tong, L.; Zhang, J.; Liu, Z. Synthesis of ultrathin graphdiyne film using a surface template. *ACS Appl. Mater. Interfaces* **2019**, *11*, 2632−2637.

(51) Kong, Y.; Li, X.; Wang, L.; Zhang, Z.; Feng, X.; Liu, J.; Chen, C.; Tong, L.; Zhang, J. Rapid synthesis of graphdiyne films on hydrogel at the superspreading interface for antibacterial. *ACS Nano* **2022**, *16*, 11338−11345.

(52) Zhao, F.; Wang, N.; Zhang, M.; Sápi, A.; Yu, J.; Li, X.; Cui, W.; Yang, Z.; Huang, C. In situ growth of graphdiyne on arbitrary substrates with a controlled-release method. *Chem. Commun.* **2018**, *54*, 6004−6007.

(53) He, J.; Wang, N.; Yang, Z.; Shen, X.; Wang, K.; Huang, C.; Yi, Y.; Tu, Z.; Li, Y. Fluoride graphdiyne as a free-standing electrode displaying ultra-stable and extraordinary high Li storage performance. *Energy Environ. Sci.* **2018**, *11*, 2893−2903.

(54) Zou, H.; Rong, W.; Long, B.; Ji, Y.; Duan, L. Corrosion-induced Cl-doped ultrathin graphdiyne toward electrocatalytic nitrogen reduction at ambient conditions. *ACS Catal.* **2019**, *9*, 10649−10655.

(55) Das, B. K.; Sen, D.; Chattopadhyay, K. K. Implications of boron doping on electrocatalytic activities of graphyne and graphdiyne families: a first principles study. *Phys. Chem. Chem. Phys.* **2016**, *18*, 2949−2958.

(56) Matsuoka, R.; Toyoda, R.; Shiotsuki, R.; Fukui, N.; Wada, K.; Maeda, H.; Sakamoto, R.; Sasaki, S.; Masunaga, H.; Nagashio, K.; Nishihara, H. Expansion of the graphdiyne family: a triphenylene-cored analogue. *ACS Appl. Mater. Interfaces* **2019**, *11*, 2730−2733.

(57) Shen, X.; He, J.; Wang, K.; Li, X.; Wang, X.; Yang, Z.; Wang, N.; Zhang, Y.; Huang, C. Fluorine-enriched graphdiyne as an efficient anode in lithium-ion capacitors. *ChemSusChem* **2019**, *12*, 1342−1348.

(58) Kang, H.; Chen, Y.; Xu, L.; Lin, Y.; Feng, Q.; Yao, H.; Zheng, Y. Top-down strategy synthesis of fluorinated graphdiyne for lithium ion battery. *RSC Adv.* **2019**, *9*, 31406−31412.

(59) He, J.; Wang, N.; Cui, Z.; Du, H.; Fu, L.; Huang, C.; Yang, Z.; Shen, X.; Yi, Y.; Tu, Z.; Li, Y. Hydrogen substituted graphdiyne as carbon-rich flexible electrode for lithium and sodium ion batteries. *Nat. Commun.* **2017**, *8*, 1172.

(60) Gao, J.; Wang, N.; He, J.; Yang, Z.; Huang, C. Precise and controllable N/C ratio in graphdiyne for superior Li and Na ions storage capacities. *2D Mater.* **2020**, *7*, 025032.

(61) Wang, X. Y.; Yao, X.; Narita, A.; Müllen, K. Heteroatom-doped nanographenes with structural precision. *Acc. Chem. Res.* **2019**, *52*, 2491−2505.

(62) Yang, Z.; Song, Y.; Ren, X.; Zhang, C.; Hu, X.; Li, X.; Wang, K.; Li, J.; Huang, C. A universal way to prepare graphyne derivatives with variable band gap and lithium storage properties. *Carbon* **2021**, *182*, 413−421.

(63) Shen, X.; Li, X.; Zhao, F.; Wang, N.; Xie, C.; He, J.; Si, W.; Yi, Y.; Yang, Z.; Li, X.; Lu, F.; Huang, C. Preparation and structure study of phosphorus-doped porous graphdiyne and its efficient lithium storage application. *2D Mater.* **2019**, *6*, 035020.

(64) Yang, Z.; Cui, W.; Wang, K.; Song, Y.; Zhao, F.; Wang, N.; Long, Y.; Wang, H.; Huang, C. Chemical modification of the sp-hybridized carbon atoms of graphdiyne by using organic sulfur. *Chemistry* **2019**, *25*, 5643−5647.

(65) Du, H.; Zhang, Z.; He, J.; Cui, Z.; Chai, J.; Ma, J.; Yang, Z.; Huang, C.; Cui, G. A delicately designed sulfide graphdiyne compatible cathode for high-performance lithium/magnesium-sulfur batteries. *Small* **2017**, *13*, 1702277.

(66) Mortazavi, B.; Shahrokhi, M.; Zhuang, X.; Rabczuk, T. Boron-Graphdiyne: A superstretchable semiconductor with low thermal conductivity and ultrahigh capacity for Li, Na and Ca ion storage. *J. Mater. Chem. A* **2018**, *6*, 11022−11036.

(67) Calipari, E. S.; Godino, A.; Peck, E. G.; Salery, M.; Mervosh, N. L.; Landry, J. A.; Russo, S. J.; Hurd, Y. L.; Nestler, E. J.; Kiraly, D. D. Granulocyte-colony stimulating factor controls neural and behavioral plasticity in response to cocaine. *Nat. Commun.* **2018**, *9*, 9.

(68) Wu, J.; Liang, J.; Zhang, Y.; Zhao, X.; Yuan, C. Synthesis of hydrogen-substituted graphdiynes via dehalogenative homocoupling reactions. *Chem. Commun.* **2021**, *57*, 5036−5039.

(69) Song, Y.; Li, X.; Yang, Z.; Wang, J.; Liu, C.; Xie, C.; Wang, H.; Huang, C. A facile liquid/liquid interface method to synthesize graphyne analogs. *Chem. Commun.* **2019**, *55*, 6571−6574.

(70) Zhang, Z.; Wu, C.; Pan, Q.; Shao, F.; Sun, Q.; Chen, S.; Li, Z.; Zhao, Y. Interfacial synthesis of crystalline two-dimensional cyano-graphdiyne. *Chem. Commun.* **2020**, *56*, 3210−3213.

(71) Kan, X.; Ban, Y.; Wu, C.; Pan, Q.; Liu, H.; Song, J.; Zuo, Z.; Li, Z.; Zhao, Y. Interfacial synthesis of conjugated two-dimensional N-graphdiyne. *ACS Appl. Mater. Interfaces* **2018**, *10*, 53−58.

(72) Abdi, G.; Filip, A.; Krajewski, M.; Kazimierczuk, K.; Strawski, M.; Szarek, P.; Hamankiewicz, B.; Mazej, Z.; Cichowicz, G.; Leszczyński, P. J.; Fijałkowski, K. J.; Szczurek, A. Toward the synthesis, fluorination and application of N-graphyne. *RSC Adv.* **2020**, *10*, 40019−40029.

(73) Li, X.; Niu, K.; Duan, S.; Tang, Y.; Hao, Z.; Xu, Z.; Ge, H.; Rosen, J.; Björk, J.; Zhang, H.; Xu, X.; Chi, L. Pyridinic nitrogen modification for selective acetylenic homocoupling on Au(111). *J. Am. Chem. Soc.* **2023**, *145*, 4545−4552.

(74) Zhou, W.; Shen, H.; Zeng, Y.; Yi, Y.; Zuo, Z.; Li, Y.; Li, Y. Controllable synthesis of graphdiyne nanoribbons. *Angew. Chem., Int. Ed.* **2020**, *132*, 4938−4943.

(75) Guo, J.; Guo, M.; Wang, F.; Jin, W.; Chen, C.; Liu, H.; Li, Y. Graphdiyne: structure of fluorescent quantum dots. *Angew. Chem., Int. Ed.* **2020**, *59*, 16712−16716.

(76) Min, H.; Qi, Y.; Chen, Y.; Zhang, Y.; Han, X.; Xu, Y.; Liu, Y.; Hu, J.; Liu, H.; Li, Y.; Nie, G. Synthesis and imaging of biocompatible graphdiyne quantum dots. *ACS Appl. Mater. Interfaces* **2019**, *11*, 32798−32807.

(77) Hu, Y.; Wu, C.; Pan, Q.; Jin, Y.; Lyu, R.; Martinez, V.; Huang, S.; Wu, J.; Wayment, L. J.; Clark, N. A.; Raschke, M. B.; Zhao, Y.; Zhang, W. Synthesis of γ-graphyne using dynamic covalent chemistry. *Nat. Syn.* **2022**, *1*, 449−454.

(78) Desyatkin, V. G.; Martin, W. B.; Aliev, A. E.; Chapman, N. E.; Fonseca, A. F.; Galvão, D. S.; Miller, E. R.; Stone, K. H.; Wang, Z.; Zakhidov, D.; Limpoco, F. T.; Almahdali, S. R.; Parker, S. M.; Baughman, R. H.; Rodionov, V. O. Scalable. Synthesis and characterization of multilayer γ-graphyne, new carbon crystals with a small direct band gap. *J. Am. Chem. Soc.* **2022**, *144*, 17999−18008.

(79) Pan, Q.; Chen, S.; Wu, C.; Shao, F.; Sun, J.; Sun, L.; Zhang, Z.; Man, Y.; Li, Z.; He, L.; Zhao, Y. Direct synthesis of crystalline graphtetrayne-a new graphyne allotrope. *CCS Chem.* **2021**, *3*, 1368−1375.

(80) Wang, Y.; An, J.; Qi, L.; Xue, Y.; Li, G.; Lyu, Q.; Yang, W.; Li, Y. Synthesis of crystalline phosphine-graphdiyne with self-adaptive P-π conjugation. *J. Am. Chem. Soc.* **2023**, *145*, 864−872.

(81) Hui, L.; Xue, Y.; Yu, H.; Liu, Y.; Fang, Y.; Xing, C.; Huang, B.; Li, Y. Highly efficient and selective generation of ammonia and hydrogen on a graphdiyne-based catalyst. *J. Am. Chem. Soc.* **2019**, *141*, 10677−10683.

(82) Yu, H.; Xue, Y.; Hui, L.; Zhang, C.; Fang, Y.; Liu, Y.; Chen, X.; Zhang, D.; Huang, B.; Li, Y. Graphdiyne-based metal atomic catalysts for synthesizing ammonia. *Natl. Sci. Rev.* **2021**, *8*, nwaa213.

(83) Zheng, Z.; Wang, Z.; Xue, Y.; He, F.; Li, Y. Selective conversion of CO_2 into cyclic carbonate on atom level catalysts. *ACS Mater. Au* **2021**, *1*, 107−115.

(84) Shi, G.; Xie, Y.; Du, L.; Fu, X.; Chen, X.; Xie, W.; Lu, T. B.; Yuan, M.; Wang, M. Constructing Cu-C Bonds in a graphdiyne-regulated Cu single-atom electrocatalyst for CO_2 reduction to CH_4. *Angew. Chem., Int. Ed.* **2022**, *61*, No. e202203569.

(85) Hui, L.; Xue, Y.; Xing, C.; Liu, Y.; Du, Y.; Fang, Y.; Yu, H.; Huang, B.; Li, Y. Highly loaded independent Pt^0 atoms on graphdiyne for PH-general methanol oxidation reaction. *Adv. Sci.* **2022**, *9*, 2104991.

(86) Zou, H.; Rong, W.; Wei, S.; Ji, Y.; Duan, L. Regulating kinetics and thermodynamics of electrochemical nitrogen reduction with metal single-atom catalysts in a pressurized electrolyser. *Proc. Natl. Acad. Sci. U. S. A.* **2020**, *117*, 29462−29468.

(87) Yu, H.; Xue, Y.; Huang, B.; Hui, L.; Zhang, C.; Fang, Y.; Liu, Y.; Zhao, Y.; Li, Y.; Liu, H.; Li, Y. Ultrathin nanosheet of graphdiyne-supported palladium atom catalyst for efficient hydrogen production. *iScience* **2019**, *11*, 31−41.

(88) Fang, Y.; Xue, Y.; Hui, L.; Chen, X.; Li, Y. High-loading metal atoms on graphdiyne for efficient nitrogen fixation to ammonia. *J. Mater. Chem. A* **2022**, *10*, 6073−6077.

(89) Feng, J.; Zhang, H. Hybrid materials based on lanthanide organic complexes: a review. *Chem. Soc. Rev.* **2013**, *42*, 387−410.

(90) Du, K.; Feng, J.; Gao, X.; Zhang, H. Nanocomposites based on lanthanide-doped upconversion nanoparticles: diverse designs and applications. *Light Sci. Appl.* **2022**, *11*, 222.

(91) Wei, Z.; Sun, J.; Lu, S.; Liu, Y.; Wang, B.; Zhao, L.; Wang, Z.; Liu, K.; Li, J.; Su, J.; Wang, F.; Zhang, H.; Yang, Y. An engineered protein-au bioplaster for efficient skin tumor therapy. *Adv. Mater.* **2022**, *34*, 2110062.

(92) Zhou, X.; Han, K.; Li, K.; Pan, J.; Wang, X.; Shi, W.; Song, S.; Zhang, H. Dual-Site single-atom catalysts with high performance for three-way catalysis. *Adv. Mater.* **2022**, *34* (20), 2201859.

(93) Zhang, H.; Zhang, H. Special issue: rare earth luminescent materials. *Light Sci. Appl.* **2022**, *11*, 260.

(94) Gao, Y.; Xue, Y.; Qi, L.; Xing, C.; Zheng, X.; He, F.; Li, Y. Rhodium nanocrystals on porous graphdiyne for electrocatalytic hydrogen evolution from saline water. *Nat. Commun.* **2022**, *13*, 5227.

(95) Fang, Y.; Xue, Y.; Hui, L.; Yu, H.; Li, Y. Graphdiyne@Janus magnetite for photocatalytic nitrogen fixation. *Angew. Chem., Int. Ed.* **2021**, *60*, 3170−3174.

(96) Zheng, X.; Gao, X.; Vilá, R. A.; Jiang, Y.; Wang, J.; Xu, R.; Zhang, R.; Xiao, X.; Zhang, P.; Greenburg, L. C.; Yang, Y.; Xin, H. L.; Zheng, X.; Cui, Y. Hydrogen-substituted graphdiyne-assisted ultrafast sparking synthesis of metastable nanomaterials. *Nat. Nanotechnol.* **2023**, *18*, 153−159.

(97) Luan, X.; Qi, L.; Zheng, Z.; Gao, Y.; Xue, Y.; Li, Y. Step by step induced growth of zinc-metal interface on graphdiyne for aqueous Zinc-ion batteries. *Angew. Chem., Int. Ed.* **2023**, *62*, No. e202215968.

(98) Chen, X.; He, F.; Fang, W.; Shen, J.; Liu, X.; Xue, Y.; Liu, H.; Li, J.; Wang, L.; Li, Y.; Fan, C. DNA-guided room-temperature synthesis of single-crystalline gold nanostructures on graphdiyne substrates. *ACS Cent. Sci.* **2020**, *6*, 779−786.

(99) Wang, F.; Zuo, Z.; Li, L.; He, F.; Lu, F.; Li, Y. A universal strategy for constructing seamless graphdiyne on metal oxides to stabilize the electrochemical structure and interface. *Adv. Mater.* **2018**, *31*, 1806272.

(100) Zhang, D.; Xue, Y.; Zheng, X.; Zhang, C.; Li, Y. Multi-heterointerfaces for selective and efficient urea production. *Natl. Sci. Rev.* **2023**, *10*, nwac209.

(101) Yin, X.-P.; Wang, H.-J.; Tang, S.-F.; Lu, X.-L.; Shu, M.; Si, R.; Lu, T.-B. Engineering the coordination environment of single-atom platinum anchored on graphdiyne for optimizing electrocatalytic hydrogen evolution. *Angew. Chem., Int. Ed.* **2018**, *130*, 9526−9530.

(102) Qi, H.; Yu, P.; Wang, Y.; Han, G.; Liu, H.; Yi, Y.; Li, Y.; Mao, L. Graphdiyne oxides as excellent substrate for electroless deposition of Pd clusters with high catalytic activity. *J. Am. Chem. Soc.* **2015**, *137*, 5260−5263.

(103) Zou, H.; Arachchige, L. J.; Rong, W.; Tang, C.; Wang, R.; Tan, S.; Chen, H.; He, D.; Hu, J.; Hu, E.; Sun, C.; Duan, L. Low-valence metal single atoms on graphdiyne promotes electrochemical nitrogen reduction via M-to-N_2 π-backdonation. *Adv. Funct. Mater.* **2022**, *32*, 2200333.

(104) Zou, H.; Rong, W.; Long, B.; Ji, Y.; Duan, L. Corrosion-induced Cl-doped ultrathin graphdiyne toward electrocatalytic nitrogen reduction at ambient conditions. *ACS Catal.* **2019**, *9*, 10649−10655.

(105) Fang, Y.; Xue, Y.; Li, Y.; Yu, H.; Hui, L.; Liu, Y.; Xing, C.; Zhang, C.; Zhang, D.; Wang, Z.; Chen, X.; Gao, Y.; Huang, B.; Li, Y. Graphdiyne interface engineering: highly active and selective ammonia synthesis. *Angew. Chem., Int. Ed.* **2020**, *59*, 13021−13027.

(106) Liu, Y.; Xue, Y.; Hui, L.; Yu, H.; Fang, Y.; He, F.; Li, Y. Porous graphdiyne loading CoO_x quantum dots for fixation nitrogen reaction. *Nano Energy* **2021**, *89*, 106333.

(107) Zhao, S.; Zheng, Z.; Qi, L.; Xue, Y.; Li, Y. Controlled growth of donor-bridge-acceptor interface for high-performance ammonia production. *Small* **2022**, *18*, 2107136.

(108) Zheng, X.; Xue, Y.; Zhang, C.; Li, Y. Controlled growth of multidimensional interface for high-selectivity ammonia production. *CCS Chem.* **2023**, *5*, 1653.

(109) Zheng, Z.; Qi, L.; Xue, Y.; Li, Y. Highly selective and durable of monodispersed metal atoms in ammonia production. *Nano Today* **2022**, *43*, 101431.

(110) Ma, J.; Wang, R.; Wang, B.; Luo, J.; Zhang, Q.; Zhuo, S. Hybrid nanoarray of Cu-MoFs@H-substituted graphdiyne with variable Lewis acidity for nitrate electroreduction. *Chem. Commun.* **2023**, *59*, 4348−4351.

(111) Ma, J.; Zhang, Y.; Wang, B.; Jiang, Z.; Zhang, Q.; Zhuo, S. Interfacial engineering of bimetallic Ni/Co-MOFs with H-substituted graphdiyne for ammonia electrosynthesis from nitrate. *ACS Nano* **2023**, *17*, 6687−6697.

(112) Zou, H.; Zhao, G.; Dai, H.; Dong, H.; Luo, W.; Wang, L.; Lu, Z.; Luo, Y.; Zhang, G.; Duan, L. Electronic perturbation of copper single-atom CO_2 reduction catalysts in a molecular way. *Angew. Chem., Int. Ed.* **2023**, *135*, No. e202217220.

(113) Liu, B.; Zhan, S.; Du, J.; Yang, X.; Zhao, Y.; Li, L.; Wan, J.; Zhao, Z. J.; Gong, J.; Yang, N.; Yu, R.; Wang, D. Revealing the mechanism of sp-N doping in graphdiyne for developing site-defined metal-free catalysts. *Adv. Mater.* **2022**, 2206450.

(114) Gu, H.; Zhong, L.; Shi, G.; Li, J.; Yu, K.; Li, J.; Zhang, S.; Zhu, C.; Chen, S.; Yang, C.; Kong, Y.; Chen, C.; Li, S.; Zhang, J.; Zhang, L. Graphdiyne/graphene heterostructure: a universal 2D scaffold anchoring monodispersed transition-metal phthalocyanines for selective and durable CO_2 electroreduction. *J. Am. Chem. Soc.* **2021**, *143*, 8679−8688.

(115) Zhao, J.; Xiong, Z.; Zhao, Y.; Wang, J.; Qiu, Y.; Liu, P.; Zhang, J. 2D/2D heterostructure of metal-free ultrathin graphdiyne/carbon nitride nanosheets for enhanced photocatalytic reduction of carbon dioxide with water. *ACS Appl. Energy Mater.* **2021**, *4*, 12403−12410.

(116) Wang, Y.; Zhang, Y.; Wang, Y.; Zeng, C.; Sun, M.; Yang, D.; Cao, K.; Pan, H.; Wu, Y.; Liu, H.; Yang, R. Constructing van der Waals heterogeneous photocatalysts based on atomically thin carbon nitride sheets and graphdiyne for highly efficient photocatalytic conversion of CO_2 into CO. *ACS Appl. Mater. Interfaces* **2021**, *13*, 40629−40637.

(117) Yang, C.; Wang, Y.; Yu, J.; Cao, S. Ultrathin 2D/2D graphdiyne/Bi_2WO_6 heterojunction for gas-phase CO_2 photoreduction. *ACS Appl. Energy Mater.* **2021**, *4*, 8734−8738.

(118) Cao, S.; Wang, Y.; Zhu, B.; Xie, G.; Yu, J.; Gong, J. R. Enhanced photochemical CO_2 reduction in the gas phase by graphdiyne. *J. Mater. Chem. A Mater.* **2020**, *8*, 7671−7676.

(119) Xu, F.; Meng, K.; Zhu, B.; Liu, H.; Xu, J.; Yu, J. Graphdiyne: a new photocatalytic co_2 reduction cocatalyst. *Adv. Funct. Mater.* **2019**, *29*, 1904256.

(120) Su, K.; Dong, G. X.; Zhang, W.; Liu, Z. L.; Zhang, M.; Lu, T. B. In situ coating $CsPbBr_3$ nanocrystals with graphdiyne to boost the activity and stability of photocatalytic CO_2 reduction. *ACS Appl. Mater. Interfaces* **2020**, *12*, 50464−50471.

(121) Yao, Y.; Zhu, Y.; Pan, C.; Wang, C.; Hu, S.; Xiao, W.; Chi, X.; Fang, Y.; Yang, J.; Deng, H.; Xiao, S.; Li, J.; Luo, Z.; Guo, Y. Interfacial

sp C-O-Mo hybridization originated high-current density hydrogen evolution. *J. Am. Chem. Soc.* **2021**, *143*, 8720−8730.

(122) Zhang, D.; Zheng, X.; Qi, L.; Xue, Y.; He, F.; Li, Y. Controlled growth of single-crystal Pd quantum dots on 2D carbon for large current density hydrogen evolution. *Adv. Funct. Mater.* **2022**, *32*, 2111501.

(123) Gao, Y.; Xue, Y.; He, F.; Li, Y. Controlled growth of a high selectivity interface for seawater electrolysis. *Proc. Natl. Acad. Sci. U. S. A.* **2022**, *119*, No. e2206946119.

(124) Gao, Y.; Qi, L.; He, F.; Xue, Y.; Li, Y. Selectively growing a highly active interface of mixed Nb-Rh oxide/2D carbon for electrocatalytic hydrogen production. *Adv. Sci.* **2022**, *9*, 2104706.

(125) Hu, C.; Liu, H.; Liu, Y.; Chen, J. F.; Li, Y.; Dai, L. Graphdiyne with tunable activity towards hydrogen evolution reaction. *Nano Energy* **2019**, *63*, 103874.

(126) Ma, K.; Wu, J.; Wang, X.; Sun, Y.; Xiong, Z.; Dai, F.; Bai, H.; Xie, Y.; Kang, Z.; Zhang, Y. Periodically interrupting bonding behavior to reformat delocalized electronic states of graphdiyne for improved electrocatalytic hydrogen evolution. *Angew. Chem., Int. Ed.* **2022**, *61*, 2211094.

(127) Liu, Y.; Xue, Y.; Yu, H.; Hui, L.; Huang, B.; Li, Y. Graphdiyne ultrathin nanosheets for efficient water splitting. *Adv. Funct. Mater.* **2021**, *31*, 2010112.

(128) Huang, H.; Li, F.; Zhang, Y.; Chen, Y. Two-dimensional graphdiyne analogue co-coordinated porphyrin covalent organic framework nanosheets as a stable electrocatalyst for the oxygen evolution reaction. *J. Mater. Chem. A Mater.* **2019**, *7*, 5575−5582.

(129) Zhao, Y.; Yang, N.; Yao, H.; Liu, D.; Song, L.; Zhu, J.; Li, S.; Gu, L.; Lin, K.; Wang, D. Stereodefined Co doping of sp-N and S atoms in few-layer graphdiyne for oxygen evolution reaction. *J. Am. Chem. Soc.* **2019**, *141*, 7240−7244.

(130) Wang, Z.; Zheng, Z.; Xue, Y.; He, F.; Li, Y. Acidic water oxidation on quantum dots of IrO_x/graphdiyne. *Adv. Energy Mater.* **2021**, *11*, 2101138.

(131) Qi, L.; Zheng, Z.; Xing, C.; Wang, Z.; Luan, X.; Xue, Y.; He, F.; Li, Y. 1D nanowire heterojunction electrocatalysts of $MnCo_2O_4$/GDY for efficient overall water splitting. *Adv. Funct. Mater.* **2022**, *32*, 2107179.

(132) Hui, L.; Jia, D.; Yu, H.; Xue, Y.; Li, Y. Ultrathin graphdiyne-wrapped iron carbonate hydroxide nanosheets toward efficient water splitting. *ACS Appl. Mater. Interfaces* **2019**, *11*, 2618−2625.

(133) Yu, H.; Xue, Y.; Hui, L.; He, F.; Zhang, C.; Liu, Y.; Fang, Y.; Xing, C.; Li, Y.; Liu, H.; Li, Y. Graphdiyne-engineered heterostructures for efficient overall water-splitting. *Nano Energy* **2019**, *64*, 103928.

(134) Chen, X.; Zhang, D.; Zheng, X.; Zhang, C.; Gao, Y.; Xing, C.; Chen, S.; Wu, H.; Xue, Y.; Li, Y. Overall water electrolysis on graphdiyne-iron oxyhydroxide heterostructure. *J. Mater. Chem. A* **2023**, *11*, 9824.

(135) Tong, R.; Ng, K. W.; Wang, X.; Wang, S.; Wang, X.; Pan, H. Two-Dimensional materials as novel Co-catalysts for efficient solar-driven hydrogen production. *J. Mater. Chem. A* **2020**, *8*, 23202−23230.

(136) Li, J.; Slassi, A.; Han, X.; Cornil, D.; Ha-Thi, M. H.; Pino, T.; Debecker, D. P.; Colbeau-Justin, C.; Arbiol, J.; Cornil, J.; Ghazzal, M. N. Tuning the electronic bandgap of graphdiyne by H-substitution to promote interfacial charge carrier separation for enhanced photocatalytic hydrogen production. *Adv. Funct. Mater.* **2021**, *31*, 2100994.

(137) Zhang, L.; Wu, Y.; Li, J.; Jin, Z.; Li, Y.; Tsubaki, N. Amorphous/crystalline heterojunction interface driving the spatial separation of charge carriers for efficient photocatalytic hydrogen evolution. *Mater. Today Phys.* **2022**, *27*, 100767.

(138) Wang, C.; Han, X.; Xu, Q.; Sun, Y. N.; Arbiol, J.; Ghazzal, M. N.; Li, J. In situ construction of graphdiyne based heterojunctions by a deprotection-free approach for photocatalytic hydrogen generation. *J. Mater. Chem. A* **2023**, *11*, 3380−3387.

(139) Guo, S.; Jiang, Y.; Wu, F.; Yu, P.; Liu, H.; Li, Y.; Mao, L. Graphdiyne-promoted highly efficient photocatalytic activity of graphdiyne/silver phosphate pickering emulsion under visible-light irradiation. *ACS Appl. Mater. Int.* **2019**, *11*, 2684−2691.

(140) Li, J.; Li, M.; Li, H.; Jin, Z. Novel CuBr-assisted graphdiyne synthesis strategy and application for efficient photocatalytic hydrogen evolution. *J. Mater. Chem. C* **2022**, *10*, 2181−2193.

(141) Shen, H.; Zhou, W.; He, F.; Gu, Y.; Li, Y.; Li, Y. A dehydrobenzoannulene-based three dimensional graphdiyne for photocatalytic hydrogen generation using pt nanoparticles as a co-catalyst and triethanolamine as a sacrificial electron donor. *J. Mater. Chem. A* **2020**, *8*, 4850−4855.

(142) Du, Y.; Xue, Y.; Zhang, C.; Liu, Y.; Fang, Y.; Xing, C.; He, F.; Li, Y. Photoinduced electrocatalysis on 3d flexible OsOx quantum dots. *Adv. Energy Mater.* **2021**, *11*, 2100234.

(143) Zhou, X.; Fu, B.; Li, L.; Tian, Z.; Xu, X.; Wu, Z.; Yang, J.; Zhang, Z. Hydrogen-substituted graphdiyne encapsulated cuprous oxide photocathode for efficient and stable photoelectrochemical water reduction. *Nat. Commun.* **2022**, *13*, 5770.

(144) Chen, X.; Zheng, X.; Qi, L.; Xue, Y.; Li, Y. Conversion of interfacial chemical bonds for inducing efficient photoelectrocatalytic water splitting. *ACS Mater. Au* **2022**, *2*, 321−329.

(145) Li, J.; Gao, X.; Li, Z.; Wang, J. H.; Zhu, L.; Yin, C.; Wang, Y.; Li, X. B.; Liu, Z.; Zhang, J.; Tung, C. H.; Wu, L. Z. Superhydrophilic graphdiyne accelerates interfacial mass/electron transportation to boost electrocatalytic and photoelectrocatalytic water oxidation activity. *Adv. Funct. Mater.* **2019**, *29*, 1808079.

(146) Zhao, Y.; Wan, J.; Yao, H.; Zhang, L.; Lin, K.; Wang, L.; Yang, N.; Liu, D.; Song, L.; Zhu, J.; Gu, L.; Liu, L.; Zhao, H.; Li, Y.; Wang, D. Few-layer graphdiyne doped with sp-hybridized nitrogen atoms at acetylenic sites for oxygen reduction electrocatalysis. *Nat. Chem.* **2018**, *10*, 924−931.

(147) Li, M.; Lv, Q.; Si, W.; Hou, Z.; Huang, C. Sp-hybridized nitrogen as new anchoring sites of iron single atoms to boost the oxygen reduction reaction. *Angew. Chem., Int. Ed.* **2022**, *61*, No. e202208238.

(148) Wang, W.; Liu, S.; Min, C.; Zeng, M.; Shi, H.; Shao, R.; Liu, S.; Xu, Z.; Xia, Y.; Li, N. A cathode material of fuel cells: F-doped γ-graphyne/PtPd nanocomposite from plasma activation and gamma irradiation. *ACS Appl. Energy Mater.* **2022**, *5*, 2036−2044.

(149) Hui, L.; Zhang, X.; Xue, Y.; Chen, X.; Fang, Y.; Xing, C.; Liu, Y.; Zheng, X.; Du, Y.; Zhang, C.; He, F.; Li, Y. Highly dispersed platinum chlorine atoms anchored on gold quantum dots for a highly efficient electrocatalyst. *J. Am. Chem. Soc.* **2022**, *144*, 1921−1928.

(150) Hui, L.; Xue, Y.; Xing, C.; Liu, Y.; Du, Y.; Fang, Y.; Yu, H.; Zhang, C.; He, F.; Li, Y. Atomic alloys of nickel-platinum on carbon network for methanol oxidation. *Nano Energy* **2022**, *95*, 106984.

(151) Yu, J.; Chen, W.; Li, K.; Zhang, C.; Li, M.; He, F.; Jiang, L.; Li, Y.; Song, W.; Cao, C. Graphdiyne nanospheres as a wettability and electron modifier for enhanced hydrogenation catalysis. *Angew. Chem., Int. Ed.* **2022**, *61*, No. e202207255.

(152) Li, J.; Zhong, L.; Tong, L.; Yu, Y.; Liu, Q.; Zhang, S.; Yin, C.; Qiao, L.; Li, S.; Si, R.; Zhang, J. Atomic Pd on graphdiyne/graphene heterostructure as efficient catalyst for aromatic nitroreduction. *Adv. Funct. Mater.* **2019**, *29*, 1905423.

(153) Yang, L. L.; Wang, H. J.; Wang, J.; Li, Y.; Zhang, W.; Lu, T. B. A graphdiyne-based carbon material for electroless deposition and stabilization of sub-nanometric pd catalysts with extremely high catalytic activity. *J. Mater. Chem. A* **2019**, *7*, 13142−13148.

(154) Yu, J.; Chen, W.; He, F.; Song, W.; Cao, C. Electronic oxide-support strong interactions in the graphdiyne-supported cuprous oxide nanocluster catalyst. *J. Am. Chem. Soc.* **2023**, *145*, 1803−1810.

(155) Pan, C.; Wang, C.; Zhao, X.; Xu, P.; Mao, F.; Yang, J.; Zhu, Y.; Yu, R.; Xiao, S.; Fang, Y.; Deng, H.; Luo, Z.; Wu, J.; Li, J.; Liu, S.; Xiao, S.; Zhang, L.; Guo, Y. Neighboring sp-hybridized carbon participated molecular oxygen activation on the interface of sub-nanocluster CuO/graphdiyne. *J. Am. Chem. Soc.* **2022**, *144*, 4942−4951.

(156) Gu, Y.; Fan, C.; Hao, X.; Hu, F.; Zhang, C.; Yang, H.; Li, C. M.; Guo, C. Oxidase mimic graphdiyne for efficient superoxide generation in wide PH ranges. *Adv. Funct. Mater.* **2022**, *32*, 2110192.

(157) Qi, H.; Tong, Y.; Zhang, M.; Wu, X.; Yue, L. Boron-doped and ketonic carbonyl group-enriched graphdiyne as a dual-site carbon nanozyme with enhanced peroxidase-like activity. *Anal. Chem.* **2022**, *94*, 17272−17278.

(158) Zhang, J.; Bai, Q.; Bi, X.; Zhang, C.; Shi, M.; Yu, W. W.; Du, F.; Wang, L.; Wang, Z.; Zhu, Z.; Sui, N. Piezoelectric enhanced peroxidase-like activity of metal-free sulfur doped graphdiyne nanosheets for efficient water pollutant degradation and bacterial disinfection. *Nano Today* **2022**, *43*, 101429.

(159) Liu, H.; Zou, H.; Wang, D.; Wang, C.; Li, F.; Dai, H.; Song, T.; Wang, M.; Ji, Y.; Duan, L. Second sphere effects promote formic acid dehydrogenation by a single-atom gold catalyst supported on amino-substituted graphdiyne. *Angew. Chem., Int. Ed.* **2023**, *62*, No. e202216739.

(160) Guo, S.; Yu, P.; Li, W.; Yi, Y.; Wu, F.; Mao, L. Electron hopping by interfacing semiconducting graphdiyne nanosheets and redox molecules for selective electrocatalysis. *J. Am. Chem. Soc.* **2020**, *142*, 2074−2082.

(161) Pan, Q.; Liu, H.; Zhao, Y.; Chen, S.; Xue, B.; Kan, X.; Huang, X.; Liu, J.; Li, Z. Preparation of N-graphdiyne nanosheets at liquid/liquid interface for photocatalytic NADH regeneration. *ACS Appl. Mater. Interfaces* **2019**, *11*, 2740−2744.

(162) Wang, F.; Zuo, Z.; Shang, H.; Zhao, Y.; Li, Y. Ultrafastly interweaving graphdiyne nanochain on arbitrary substrates and its performance as a supercapacitor electrode. *ACS Appl. Mater. Interfaces* **2019**, *11*, 2599−2607.

(163) Lu, T.; He, J.; Li, R.; Wang, K.; Yang, Z.; Shen, X.; Li, Y.; Xiao, J.; Huang, C. Adjusting the interface structure of graphdiyne by H and F Co-doping for enhanced capacity and stability in Li-ion battery. *Energy Storage Mater.* **2020**, *29*, 131−139.

(164) Li, C.; Zhang, X.; Wang, K.; Sun, X.; Ma, Y. High-power Lithium-ion hybrid supercapacitor enabled by holey carbon nanolayers with targeted porosity. *J. Power Sources* **2018**, *400*, 468−477.

(165) Li, L.; Zuo, Z.; Shang, H.; Wang, F.; Li, Y. In-situ constructing 3D graphdiyne as all-carbon binder for high-performance silicon anode. *Nano Energy* **2018**, *53*, 135−143.

(166) Du, H.; Yang, H.; Huang, C.; He, J.; Liu, H.; Li, Y. Graphdiyne applied for lithium-ion capacitors displaying high power and energy densities. *Nano Energy* **2016**, *22*, 615−622.

(167) Li, J.; Li, S.; Liu, Q.; Yin, C.; Tong, L.; Chen, C.; Zhang, J. Synthesis of hydrogen-substituted graphyne film for lithium-sulfur battery applications. *Small* **2019**, *15*, 1805344.

(168) Li, J.; Xu, J.; Xie, Z.; Gao, X.; Zhou, J.; Xiong, Y.; Chen, C.; Zhang, J.; Liu, Z. Diatomite-templated synthesis of freestanding 3d graphdiyne for energy storage and catalysis application. *Adv. Mater.* **2018**, *30*, 1800548.

(169) Lin, Z.; Liu, G.; Zheng, Y.; Lin, Y.; Huang, Z. Three-dimensional hierarchical mesoporous flower-like TiO_2@graphdiyne with superior electrochemical performances for Lithium-ion batteries. *J. Mater. Chem. A* **2018**, *6*, 22655−22661.

(170) Wang, Y.; He, J.; Zhang, Z.; Liu, Z.; Huang, C.; Jin, Y. Graphdiyne-modified polyimide separator: a polysulfide-immobilizing net hinders the shuttling of polysulfides in lithium-sulfur battery. *ACS Appl. Mater. Interfaces* **2019**, *11*, 35738−35745.

(171) Huang, H.; Li, K.; Fan, X.; Singh, D. J.; Zheng, W. T. Storage of Na in Layered Graphdiyne as high capacity anode materials for sodium ion batteries. *J. Mater. Chem. A* **2019**, *7*, 25609−25618.

(172) Yang, Z.; Zhang, C.; Hou, Z.; Wang, X.; He, J.; Li, X.; Song, Y.; Wang, N.; Wang, K.; Wang, H.; Huang, C. Porous hydrogen substituted graphyne for high capacity and ultra-stable sodium ion storage. *J. Mater. Chem. A* **2019**, *7*, 11186−11194.

(173) Gong, S.; Wang, S.; Liu, J.; Guo, Y.; Wang, Q. Graphdiyne as an ideal monolayer coating material for lithium-ion battery cathodes with ultralow areal density and ultrafast Li penetration. *J. Mater. Chem. A* **2018**, *6*, 12630−12636.

(174) Huang, C.; Zhang, S.; Liu, H.; Li, Y.; Cui, G.; Li, Y. Graphdiyne for high capacity and long-life lithium storage. *Nano Energy* **2015**, *11*, 481−489.

(175) Jang, B.; Koo, J.; Park, M.; Lee, H.; Nam, J.; Kwon, Y.; Lee, H. Graphdiyne as a high-capacity lithium ion battery anode material. *Appl. Phys. Lett.* **2013**, *103*, 263904.

(176) An, J.; Zhang, H.; Qi, L.; Li, G.; Li, Y. Self-expanding ion-transport channels on anodes for fast-charging lithium-ion batteries. *Angew. Chem., Int. Ed.* **2022**, *61*, No. e202113313.

(177) Wang, F.; An, J.; Shen, H.; Wang, Z.; Li, G.; Li, Y. Gradient graphdiyne induced copper and oxygen vacancies in $Cu_{0.95}V_2O_5$ anodes for fast-charging lithium-ion batteries. *Angew. Chem., Int. Ed.* **2022**, No. e202216397.

(178) Zuo, Z.; He, F.; Wang, F.; Li, L.; Li, Y. Spontaneously splitting copper nanowires into quantum dots on graphdiyne for suppressing lithium dendrites. *Adv. Mater.* **2020**, *32* (49), 2004379.

(179) Wang, N.; He, J.; Tu, Z.; Yang, Z.; Zhao, F.; Li, X.; Huang, C.; Wang, K.; Jiu, T.; Yi, Y.; Li, Y. Synthesis of chlorine-substituted graphdiyne and applications for lithium-ion storage. *Angew. Chem., Int. Ed.* **2017**, *129*, 10880−10885.

(180) He, J.; Wang, N.; Yang, Z.; Shen, X.; Wang, K.; Huang, C.; Yi, Y.; Tu, Z.; Li, Y. Fluoride graphdiyne as a free-standing electrode displaying ultra-stable and extraordinary high Li storage performance. *Energy Environ. Sci.* **2018**, *11*, 2893−2903.

(181) Zhu, M.; Yin, C.; Wang, Q.; Zhang, Y.; Zhou, H.; Tong, L.; Zhang, J.; Qi, L. Columnar lithium deposition guided by graphdiyne nanowalls toward a stable lithium metal anode. *ACS Appl. Mater. Interfaces* **2022**, *14*, 55700−55708.

(182) Li, L.; Zuo, Z.; Wang, F.; Gao, J.; Cao, A.; He, F.; Li, Y. In situ coating graphdiyne for high-energy-density and stable organic cathodes. *Adv. Mater.* **2020**, *32*, No. e2000140.

(183) Wan, J.; Zuo, Z.; Shen, Z. Z.; Chen, W. P.; Liu, G. X.; Hu, X. C.; Song, Y. X.; Xin, S.; Guo, Y. G.; Wen, R.; Li, Y.; Wan, L. J. Interfacial evolution of the solid electrolyte interphase and lithium deposition in graphdiyne-based Lithium-ion batteries. *J. Am. Chem. Soc.* **2022**, *144*, 9354−9362.

(184) Wang, F.; Zuo, Z.; Li, L.; He, F.; Li, Y. Graphdiyne nanostructure for high-performance lithium-sulfur batteries. *Nano Energy* **2020**, *68*, 104307.

(185) Yi, Y.; Huang, W.; Tian, X.; Fang, B.; Wu, Z.; Zheng, S.; Li, M.; Ma, H. Graphdiyne-like porous organic framework as a solid-phase sulfur conversion cathodic host for stable Li-S batteries. *ACS Appl. Mater. Interfaces* **2021**, *13*, 59983−59992.

(186) Zhang, J.; Wang, F.; Qi, G.; Cheng, J.; Chen, L.; Liu, H.; Wang, B. Rechargeable Li-CO_2 batteries with graphdiyne as efficient metal-free cathode catalysts. *Adv. Funct. Mater.* **2021**, *31*, 2101423.

(187) Xu, J.; Liu, Q.; Dong, Z.; Wang, L.; Xie, X.; Jiang, Y.; Wei, Z.; Gao, Y.; Zhang, Y.; Huang, K. Interconnected MoS_2 on 2D graphdiyne for reversible sodium storage. *ACS Appl. Mater. Interfaces* **2021**, *13*, 54974−54980.

(188) Wang, N.; Li, X.; Tu, Z.; Zhao, F.; He, J.; Guan, Z.; Huang, C.; Yi, Y.; Li, Y. Synthesis and electronic structure of boron-graphdiyne with an sp-hybridized carbon skeleton and its application in sodium storage. *Angew. Chem., Int. Ed.* **2018**, *130*, 4032−4037.

(189) Liu, Y.; Qing, Y.; Zhou, B.; Wang, L.; Pu, B.; Zhou, X.; Wang, Y.; Zhang, M.; Bai, J.; Tang, Q.; Yang, W. Yolk-shell Sb@void@graphdiyne nanoboxes for high-rate and long cycle life sodium-ion batteries. *ACS Nano* **2023**, *17*, 2431−2439.

(190) Yi, Y.; Li, J.; Zhao, W.; Zeng, Z.; Lu, C.; Ren, H.; Sun, J.; Zhang, J.; Liu, Z. Temperature-mediated engineering of graphdiyne framework enabling high-performance potassium storage. *Adv. Funct. Mater.* **2020**, *30*, 2003039.

(191) Yi, Y.; Li, J.; Gao, Z.; Liu, W.; Zhao, Y.; Wang, M.; Zhao, W.; Han, Y.; Sun, J.; Zhang, J. Highly potassiophilic graphdiyne skeletons decorated with cu quantum dots enable dendrite-free potassium-metal anodes. *Adv. Mater.* **2022**, *34*, 2202685.

(192) He, J.; Lu, T.; Wang, K.; Wang, X.; Li, X.; Shen, X.; Gao, J.; Si, W.; Yang, Z.; Huang, C. Rational construction of advanced potassium ion diffusion and storage matrix. *Adv. Funct. Mater.* **2021**, *31*, 2005933.

(193) Li, J.; Yi, Y.; Zuo, X.; Hu, B.; Xiao, Z.; Lian, R.; Kong, Y.; Tong, L.; Shao, R.; Sun, J.; Zhang, J. Graphdiyne/graphene/graphdiyne sandwiched carbonaceous anode for potassium-ion batteries. *ACS Nano* **2022**, *16*, 3163−3172.

(194) Li, J.; Chen, Y.; Guo, J.; Wang, F.; Liu, H.; Li, Y. Graphdiyne Oxide-Based High-Performance Rechargeable Aqueous Zn-MnO2 Battery. *Adv. Funct. Mater.* **2020**, *30*, 2004115.

(195) Yang, Q.; Guo, Y.; Yan, B.; Wang, C.; Liu, Z.; Huang, Z.; Wang, Y.; Li, Y.; Li, H.; Song, L.; Fan, J.; Zhi, C. Hydrogen-Substituted Graphdiyne Ion Tunnels Directing Concentration Redistribution for Commercial-Grade Dendrite-Free Zinc Anodes. *Adv. Mater.* **2020**, *32*, 2001755.

(196) Yang, Q.; Li, L.; Hussain, T.; Wang, D.; Hui, L.; Guo, Y.; Liang, G.; Li, X.; Chen, Z.; Huang, Z.; Li, Y.; Xue, Y.; Zuo, Z.; Qiu, J.; Li, Y.; Zhi, C. Stabilizing interface PH by N-modified graphdiyne for dendrite-free and high-rate aqueous Zn-ion batteries. *Angew. Chem., Int. Ed.* **2022**, *61*, e202112304.

(197) Lu, T.; Hu, X.; He, J.; Li, R.; Gao, J.; Lv, Q.; Yang, Z.; Cui, S.; Huang, C. Aqueous/Solid State Zn-Air Batteries Based on N Doped Graphdiyne as Efficient Metal-Free Bifunctional Catalyst. *Nano Energy* **2021**, *85*, 106024.

(198) Liu, L.; Kan, Y.; Gao, K.; Wang, J.; Zhao, M.; Chen, H.; Zhao, C.; Jiu, T.; Jen, A. K. Y.; Li, Y. Graphdiyne Derivative as Multifunctional Solid Additive in Binary Organic Solar Cells with 17.3% Efficiency and High Reproductivity. *Adv. Mater.* **2020**, *32*, 1907604.

(199) Sun, Y.; Nian, L.; Kan, Y.; Ren, Y.; Chen, Z.; Zhu, L.; Zhang, M.; Yin, H.; Xu, H.; Li, J.; Hao, X.; Liu, F.; Gao, K.; Li, Y. Rational Control of Sequential Morphology Evolution and Vertical Distribution toward 17.18% Efficiency All-Small-Molecule Organic Solar Cells. *Joule* **2022**, *6*, 2835−2848.

(200) Zhang, S.; Si, H.; Fan, W.; Shi, M.; Li, M.; Xu, C.; Zhang, Z.; Liao, Q.; Sattar, A.; Kang, Z.; Zhang, Y. Graphdiyne: Bridging SnO2 and Perovskite in Planar Solar Cells. *Angew. Chem., Int. Ed.* **2020**, *59*, 2003502.

(201) Li, H.; Zhang, R.; Li, Y.; Li, Y.; Liu, H.; Shi, J.; Zhang, H.; Wu, H.; Luo, Y.; Li, D.; Li, Y.; Meng, Q. Graphdiyne-Based Bulk Heterojunction for Efficient and Moisture-Stable Planar Perovskite Solar Cells. *Adv. Energy Mater.* **2018**, *8*, 1802012.

(202) Fan, W.; Zhang, S.; Xu, C.; Si, H.; Xiong, Z.; Zhao, Y.; Ma, K.; Zhang, Z.; Liao, Q.; Kang, Z.; Zhang, Y. Grain Boundary Perfection Enabled by Pyridinic Nitrogen Doped Graphdiyne in Hybrid Perovskite. *Adv. Funct. Mater.* **2021**, *31*, 2104633.

(203) Wang, F.; Zuo, Z.; Li, L.; Li, K.; He, F.; Jiang, Z.; Li, Y. Large-Area Aminated-Graphdiyne Thin Films for Direct Methanol Fuel Cells. *Angew. Chem., Int. Ed.* **2019**, *58*, 15010−15015.

(204) Pan, H.; Jiang, Z.; Zuo, Z.; He, F.; Wang, F.; Li, L.; Chang, Q.; Guan, B.; Li, Y. Proton Selective Anode Nanochannel for Efficient Methanol Utilization. *Nano Today* **2021**, *39*, 101213.

(205) Wang, Q.; Liu, Y.; Wang, H.; Jiang, P.; Qian, W.; You, M.; Han, Y.; Zeng, X.; Li, J.; Lu, H.; Jiang, L.; Zhu, M.; Li, S.; Huang, K.; Tang, M.; Wang, X.; Yan, L.; Xiong, Z.; Shi, X.; Bai, G.; Liu, H.; Li, Y.; Zhao, Y.; Chen, C.; Qian, P. Graphdiyne Oxide Nanosheets Display Selective Anti-Leukemia Efficacy against DNMT3A-Mutant AML Cells. *Nat. Commun.* **2022**, *13*, 5657.

(206) Guo, M.; Liu, J.; Chen, X.; You, Z.; Gao, F.; Liu, T.; Ren, J.; Liu, J.; Xiong, Z.; Liu, Y.; Wang, Y.; Liu, H.; Chang, X.; Cai, R.; Chen, C. Graphdiyne Oxide Nanosheets Reprogram Immunosuppressive Macrophage for Cancer Immunotherapy. *Nano Today* **2022**, *45*, 101543.

(207) Li, J.; Wang, Q.; Lu, H.; Han, Y.; Jiang, L.; Qian, W.; Zhu, M.; Wang, B.; Min, J.; Hou, Y.; Xu, S.; Xiong, Z.; Liu, H.; Li, Y.; Chen, C.; Liu, Y.; Qian, P. Graphdiyne oxide nanosheets exert anti-lymphoma effect by killing cancer stem cells and remodeling tumor microenvironment. *Nano Today* **2022**, *46*, 101622.

(208) Min, H.; Qi, Y.; Zhang, Y.; Han, X.; Cheng, K.; Liu, Y.; Liu, H.; Hu, J.; Nie, G.; Li, Y. A graphdiyne oxide-based iron sponge with photothermally enhanced tumor-specific Fenton chemistry. *Adv. Mater.* **2020**, *32*, 2000038.

(209) Zhang, C.; Chen, L.; Bai, Q.; Wang, L.; Li, S.; Sui, N.; Yang, D.; Zhu, Z. Nonmetal graphdiyne nanozyme-based ferroptosis-apoptosis strategy for colon cancer therapy. *ACS Appl. Mater. Interfaces* **2022**, *14*, 27720−27732.

(210) Xie, J.; Wang, C.; Wang, N.; Zhu, S.; Mei, L.; Zhang, X.; Yong, Y.; Li, L.; Chen, C.; Huang, C.; Gu, Z.; Li, Y.; Zhao, Y. Graphdiyne nanoradioprotector with efficient free radical scavenging ability for mitigating radiation-induced gastrointestinal tract damage. *Biomaterials* **2020**, *244*, 119940.

(211) Wang, R.; Shi, M.; Xu, F.; Qiu, Y.; Zhang, P.; Shen, K.; Zhao, Q.; Yu, J.; Zhang, Y. Graphdiyne-modified TiO_2 nanofibers with osteoinductive and enhanced photocatalytic antibacterial activities to prevent implant infection. *Nat. Commun.* **2020**, *11*, 4465.

(212) Zhang, Y.; Liu, W.; Li, Y.; Yang, Y. W.; Dong, A.; Li, Y. 2D graphdiyne oxide serves as a superior new generation of antibacterial agents. *iScience* **2019**, *19*, 662−675.

(213) Parvin, N.; Jin, Q.; Wei, Y.; Yu, R.; Zheng, B.; Huang, L.; Zhang, Y.; Wang, L.; Zhang, H.; Gao, M.; Zhao, H.; Hu, W.; Li, Y.; Wang, D. Few-layer graphdiyne nanosheets applied for multiplexed real-time DNA detection. *Adv. Mater.* **2017**, *29*, 1606755.

(214) Xu, J.; Liu, Y.; Huang, K. J.; Hou, Y. Y.; Sun, X.; Li, J. Real-time biosensor platform based on novel sandwich graphdiyne for ultra-sensitive detection of tumor marker. *Anal. Chem.* **2022**, *94*, 16980−16986.

(215) Hou, Y. X.; Li, Y.; Zhang, Z. C.; Li, J. Q.; Qi, D. H.; Chen, X. D.; Wang, J. J.; Yao, B. W.; Yu, M. X.; Lu, T. B.; Zhang, J. Large-scale and flexible optical synapses for neuromorphic computing and integrated visible information sensing memory processing. *ACS Nano* **2021**, *15*, 1497−1508.

(216) Li, Y.; Zhang, M.; Hu, X.; Yu, L.; Fan, X.; Huang, C.; Li, Y. Graphdiyne-based flexible respiration sensors for monitoring human health. *Nano Today* **2021**, *39*, 101214.

(217) Wei, H.; Shi, R.; Sun, L.; Yu, H.; Gong, J.; Liu, C.; Xu, Z.; Ni, Y.; Xu, J.; Xu, W. Mimicking efferent nerves using a graphdiyne-based artificial synapse with multiple ion diffusion dynamics. *Nat. Commun.* **2021**, *12*, 1068.

(218) Fu, X.; He, F.; Gao, J.; Yan, X.; Chang, Q.; Zhang, Z.; Huang, C.; Li, Y. Directly growing graphdiyne nanoarray cathode to integrate an intelligent solid mg-moisture battery. *J. Am. Chem. Soc.* **2023**, *145*, 2759−2764.

(219) Li, W.; Xu, C.; Xiong, T.; Jiang, Y.; Ma, W.; Yu, P.; Mao, L. Giant water uptake enabled ultrahigh proton conductivity of graphdiyne oxide. *Angew. Chem., Int. Ed.* **2023**, *62*, No. e202216530.

(220) Zhang, Y.; Huang, P.; Guo, J.; Shi, R.; Huang, W.; Shi, Z.; Wu, L.; Zhang, F.; Gao, L.; Li, C.; Zhang, X.; Xu, J.; Zhang, H. Graphdiyne-based flexible photodetectors with high responsivity and detectivity. *Adv. Mater.* **2020**, *32*, 2001082.

(221) Li, X.; Li, Y.; Zhang, M.; Yang, Z.; Wang, K.; Huang, C. Carbon nano thorn arrays based water/cold resisted nanogenerator for wind energy harvesting and speed sensing. *Nano Energy* **2021**, *90*, 106571.

(222) Lin, T.; Wang, J. Applications of graphdiyne on optoelectronic devices. *ACS Appl. Mater. Interfaces* **2019**, *11*, 2638−2646.

(223) Gao, N.; Zeng, H.; Wang, X.; Zhang, Y.; Zhang, S.; Cui, R.; Zhang, M.; Mao, L. Graphdiyne: A new carbon allotrope for electrochemiluminescence. *Angew. Chem., Int. Ed.* **2022**, *61*, No. e202204485.

(224) Li, J.; Zhang, Z.; Kong, Y.; Yao, B.; Yin, C.; Tong, L.; Chen, X.; Lu, T.; Zhang, J. Synthesis of wafer-scale ultrathin graphdiyne for flexible optoelectronic memory with over 256 storage levels. *Chem.* **2021**, *7*, 1284−1296.

(225) Wu, L.; Dong, Y.; Zhao, J.; Ma, D.; Huang, W.; Zhang, Y.; Wang, Y.; Jiang, X.; Xiang, Y.; Li, J.; Feng, Y.; Xu, J.; Zhang, H. Kerr Nonlinearity in 2D Graphdiyne for Passive Photonic Diodes. *Adv. Mater.* **2019**, *31*, 1807981.

(226) Yao, B. W.; Li, J.; Chen, X. D.; Yu, M. X.; Zhang, Z. C.; Li, Y.; Lu, T. B.; Zhang, J. Non-volatile electrolyte-gated transistors based on graphdiyne/MoS_2 with robust stability for low-power neuromorphic computing and logic-in-memory. *Adv. Funct. Mater.* **2021**, *31*, 2100069.

(227) Qu, S.; Ming, C.; Qiu, P.; Xu, K.; Xu, Q.; Yao, Q.; Lu, P.; Zeng, H.; Shi, X.; Chen, L. High-performance n-Type Ta_4SiTe_4/polyvinylidene fluoride (PVDF)/graphdiyne organic-inorganic flexible thermoelectric composites. *Energy Environ. Sci.* **2021**, *14*, 6586−6594.

(228) Zhou, Z.; Tan, Y.; Yang, Q.; Bera, A.; Xiong, Z.; Yagmurcukardes, M.; Kim, M.; Zou, Y.; Wang, G.; Mishchenko, A.; Timokhin, I.; Wang, C.; Wang, H.; Yang, C.; Lu, Y.; Boya, R.; Liao, H.; Haigh, S.; Liu, H.; Peeters, F. M.; Li, Y.; Geim, A. K.; Hu, S. Gas Permeation through graphdiyne-based nanoporous membranes. *Nat. Commun.* **2022**, *13*, 4031.

(229) Liu, Q.; Li, J.; Hadjichristidis, N. Graphdiyne aerogel architecture via a modified hiyama coupling reaction for gas adsorption. *Chem. Commun.* **2023**, *59*, 2165−2168.

(230) Ma, H.; Yang, B.; Wang, Z.; Wu, K.; Zhang, C. A Three dimensional graphdiyne-like porous triptycene network for gas adsorption and separation. *RSC Adv.* **2022**, *12*, 28299−28305.

(231) Li, J.; Chen, Y.; Gao, J.; Zuo, Z.; Li, Y.; Liu, H.; Li, Y. Graphdiyne sponge for direct collection of oils from water. *ACS Appl. Mater. Interfaces* **2019**, *11*, 2591−2598.

(232) Gao, X.; Zhou, J.; Du, R.; Xie, Z.; Deng, S.; Liu, R.; Liu, Z.; Zhang, J. Robust. Superhydrophobic foam: a graphdiyne-based hierarchical architecture for oil/water separation. *Adv. Mater.* **2016**, *28*, 168−173.

(233) Qiu, H.; Xue, M.; Shen, C.; Zhang, Z.; Guo, W. Graphynes for water desalination and gas separation. *Adv. Mater.* **2019**, *31*, 1803772.

(234) Xue, M.; Qiu, H.; Guo, W. Exceptionally fast water desalination at complete salt rejection by pristine graphyne monolayers. *Nanotechnology* **2013**, *24*, 505720.

(235) Yuan, T.; Xiong, S.; Shen, X. Coordination of actinide single ions to deformed graphdiyne: strategy on essential separation processes in nuclear fuel cycle. *Angew. Chem., Int. Ed.* **2020**, *59*, 17719−17725.

(236) Yang, X.; Qu, Z.; Li, S.; Peng, M.; Li, C.; Hua, R.; Fan, H.; Caro, J.; Meng, H. Ultra-Fast Preparation of large-area graphdiyne-based membranes via alkynylated surface-modification. *Angew. Chem., Int. Ed.* **2023**, *135*, No. e202217378.